TOR VERGATA UNIVERSITY, ROME, ITALY

Department of Computer, Systems and Industrial Engineering

GeoInformation PhD Programme

XXI Cycle

Neural Networks algorithms for the estimation of atmospheric ozone from Envisat-SCIAMACHY and Aura-OMI measurements

A thesis submitted in partial fulfillment for the degree of Doctor of Philosophy

Mentor: Fabio Del Frate

Candidate: Pasquale Sellitto

February 2009

Dedicated to Chiara

"Nature - the Gentlest Mother is
Impatient of no Child -
The feeblest - or the waywardest -
Her Admonition mild -

In Forest - and the Hill -
By Traveller - be heard -
Restraining Rampant Squirrel -
Or too impetuous Bird -

How fair Her Conversation -
A Summer Afternoon -
Her Household - Her Assembly -
And when the Sun go down -

Her Voice among the Aisles
Incite the timid prayer
Of the minutest Cricket -
The most unworthy Flower -

When all the Children sleep -
She turns as long away
As will suffice to light Her lamps -
Then bending from the Sky -

With infinite Affection -
And infiniter Care -
Her Golden finger on Her lip -
Wills Silence - Everywhere -"

Emily Dickinson

Acknowledgements

Nel settembre 2005, da neolaureato in Fisica all'Università "La Sapienza", decisi di partecipare all'esame di ammisione al corso di Dottorato di Ricerca in GeoInformazione, all'Università "Tor Vergata", Dipartimento di Ingegneria dell'Informazione. Oggi posso ammetterlo, avevo letto, in fretta e furia solo 2 o 3 articoli sul telerilevamento dell'atmosfera da satellite, li avevo letti rapidamente e non ci avevo capito molto. Ero vestito da "fisico", il che scatenó qualche ilarità [1], e non conoscevo nessuno a Tor Vergata. Avevo alle spalle un contratto (che avevo rifiutato) da studente di dottorato al Forschungszentrum Jülich e la ragionevole prospettiva di vincere una posizione analoga per il dottorato in Telerilevamento a "La Sapienza". Invece vinsi qui, anche grazie alle rinunce di Cosimo e Alessandro, e decisi di accettare. Vinsi anche grazie a due parole che avevo letto distrattamente su uno dei 2 o 3 famosi articoli. Un membro della commisione esaminatrice mi chiese come mi aspettavo si potesse ricavare un profilo di qualcosa da uno spettro di qualcosa. Il membro era il Prof. Fabio Del Frate, la risposta fu *Optimal Estimation*. Un guizzo di memoria ed ecco la risposta. Non sapevo esattamente di cosa stessi parlando, ma la risposta era giusta e l'avevo data grazie a 2 articoli a caso letti pochi minuti prima. Dunque avevo cambiato al contempo Facoltà e Ateneo, ero un dottorando a "Tor Vergata" per merito di un caso fortunato e di due rinunce. Oggi ripenso a quel giorno come una svolta fondamentale della mia vita, che mi aveva aperto le porte a una esperienza non sempre facile, a volte frustrante, ma che, come poche altre, mi ha instradato verso il mio futuro. Per questo il mio primo ringraziamento va al Caso, al Destino, a Dio, come vogliamo chiamare il motore di questi eventi.

Tre anni duri ma con un altissimo *coefficiente di crescita personale*, dicevo. Per questo vorrei ringraziare fortemente il Prof. Fabio Del Frate, che ha permesso e favorito lo sviluppo delle mie capacità di (nascente) ricercatore, e che, grazie alla sua grande pacatezza, ha consentito una crescita "indipendente". Allo stesso modo vorrei ringraziare il Prof. Domenico Solimini, e lo staff del programma di dottorato in GeoInformazione. Un ringraziamento al Prof. Pawan K. Bhartia del NASA-GSFC per la sua disponibilità durante il mio periodo di ricerca in America, e a tutto l'Atmospheric Chemistry and Dynamics Branch del NASA-GSFC. In questo contesto voglio fare un ringraziamento speciale a Christian Retscher (che anche autore del Paragrafo (2.2.6)) e Bojan Bojkov dell'AVDC per il loro competente supporto.

Un ringraziamento a tutti gli studenti di dottorato dell'EOLab (in senso antiorario a partire dalla mia postazione in laboratorio), Giorgio Licciardi, Fabio Pacifici, Chiara Pratola, Michele Lazzarini, Emanuele Angiuli, e agli ex-studenti e a quelli che non sono

[1] E' ben noto come gli Ingegneri facciano una grande attenzione all'abbigliamento, il che li porta spesso e volentieri a indossare dei gilet grigi.

stati fisicamente nell'EOLab, Andrea Minchella (a cui aggiungo un ringraziamento per il supporto all'Envisat Symposium 2007), Andrea Radius, Chiara Solimini, Riccardo Duca, Alessandro Burini, Cosimo Putignano, e tutti gli altri. Un ringraziamento a Michele Iapaolo per avermi aiutato nelle prime fasi del mio dottorato.

Infine un grande ringraziamento a tutti i miei amici e familiari, senza i quali non avrei raggiunto questo né alcun altro obiettivo, ai miei genitori, a mio fratello Luca, a Chiara, mia moglie, che ha mi supportato e sopportato in questi anni. Il contributo di Chiara a questo traguardo incalcolabile e a lei dedico la mia tesi.

I acknowledge Dr. Christian Retscher for the contents of Sec. (2.2.6). I'd like to acknowledge the owners and providers of WOUDC and SHADOZ ozonesondes data. Eng. Emanuele Angiuli is gratefully acknowledged for his valuable IDL advices. Eng. Alessandro Burini is acknowledged for the fruitful collaboration and discussion regarding the dataset preparation for the work described in Chapter (5). Dr. Mark Kroon from KNMI is acknowledged for his highly skilled management of OMI cal/val AO, including project no. 2930.

(a) Tipiche condizioni meteo a Greenbelt, MD, USA

(b) IV giornata della GeoInformazione, Marzo 2006: molta eleganza sprecata

(c) Poiché la mensa dell'Università non soddisfa i dottorandi, tre di loro vanno a pranzo a Frascati

(d) Me medesimo in abbondanza di scattering molecolare

Contents

Acknowledgements iii

Preface 1

1 Atmospheric ozone measurements 3
1.1 Atmospheric structure and composition . . . 3
1.2 Ozone in the Earth's atmosphere . . . 6
1.2.1 Introduction . . . 6
1.2.2 Stratospheric ozone . . . 8
1.2.2.1 Formation and removal mechanisms . . . 8
1.2.2.2 Spatial and temporal variabilities . . . 10
1.2.3 Tropospheric ozone . . . 13
1.2.3.1 Formation and removal mechanisms . . . 13
1.2.3.2 Spatial and temporal variabilities . . . 15
1.2.4 Spectroscopic characterization of the ozone . . . 16
1.3 Radiative transfer through the Earth's atmosphere . . . 18
1.3.1 Definition of radiometric parameters of interest . . . 18
1.3.2 Radiative transfer equation . . . 19
1.4 Height resolved atmospheric ozone measurements . . . 20
1.4.1 In situ techniques . . . 21
1.4.2 Ground-based remote sensing techniques . . . 21
1.4.3 Air-borne instruments . . . 22
1.4.4 Satellite-borne techniques . . . 23
1.4.4.1 Nadir viewing instruments . . . 24
1.4.4.2 Limb viewing instruments . . . 24
1.4.4.3 Occultation viewing instruments . . . 25
1.4.4.4 Ozone profiles retrieval from nadir UV/VIS satellite data 25
1.4.4.5 Tropospheric ozone retrieval from nadir UV/VIS satellite data . . . 26
1.5 Thesis outline . . . 26

2 The SCIAMACHY and the OMI missions 28
2.1 The SCanning Imaging Absorption spectroMeter for Atmospheric CHartographY (SCIAMACHY) . . . 28
2.1.1 The EnviSat Platform . . . 28
2.1.2 The instrument . . . 29
2.1.3 Operations . . . 34

2.1.4 Calibration and Monitoring . . . 37
2.2 The Ozone Monitoring Instrument (OMI) . . . 41
2.2.1 The EOS-Aura Platform . . . 41
2.2.2 The A-Train . . . 42
2.2.3 The Instrument . . . 43
2.2.4 Operations . . . 48
2.2.5 Calibration and Monitoring . . . 49
2.2.6 The Aura Validation Data Center . . . 55

3 The inversion issue in remote sounding 56
3.1 Introduction . . . 56
3.2 Physical approach to the inversion issue . . . 57
3.2.1 Statement of the problem . . . 57
3.2.2 Inversion theory for profile quantities . . . 58
3.2.2.1 Introducing the height dependency . . . 58
3.2.2.2 A Bayesian approach . . . 60
3.2.2.3 Error estimation . . . 61
3.2.2.4 Non linear optimal estimation approach . . . 61
3.2.2.5 Error estimation in non linear case . . . 62
3.3 Neural networks algorithms . . . 63
3.3.1 Introduction . . . 63
3.3.2 Basic principles of the Multilayer Perceptron . . . 63
3.3.3 The representation problem . . . 65
3.3.4 The learning problem . . . 66
3.3.4.1 The Error Backpropagation Algorithm . . . 67
3.3.5 NNs and the retrieval of profile quantities . . . 70
3.3.6 Advantages and disadvantages of NNs algorithms . . . 70

4 NNs for tropospheric ozone column retrieval from nadir UV/VIS SCIAMACHY data 71
4.1 Introduction . . . 71
4.2 Analysis of the Sensitivity of Satellite Measurements to Tropospheric Ozone Variations . . . 73
4.2.1 Dataset Generation . . . 78
4.2.2 Neural Net Inversion of UV Radiances . . . 79
4.2.3 Neural Net Inversion of UV-VIS Radiances . . . 81
4.2.3.1 Wavelength Selection by Combined RTM-NN EP Procedure . . . 81
4.3 A Case Study With Experimental SCIAMACHY UV/VIS Data . . . 85
4.3.1 Dataset Generation . . . 85
4.3.2 Results . . . 87
4.4 Summary and Conclusion . . . 87

5 NNs for ozone profile retrieval from nadir UV/VIS SCIAMACHY data 89
5.1 Introduction . . . 89
5.2 Training and test sets generation . . . 90
5.3 Algorithm optimization . . . 92

5.4 Results . . . 92
5.5 Conclusion . . . 94

6 NNs for stratospheric ozone profile retrieval from OMI data 96
6.1 Introduction . . . 96
6.2 Training and test sets generation . . . 97
6.3 Algorithm optimization . . . 98
6.4 Results . . . 98
6.5 Conclusion . . . 99

Conclusion 101

A NNs for the retrieval of other atmospheric parameters 104
A.1 Introduction . . . 104
A.2 NNs for the retrieval of temperature profiles from satellite UV/VIS simulated radiances . . . 105
A.2.1 Sensitivity analysis . . . 105
A.2.2 Algorithm design and optimization . . . 106
A.2.3 Results . . . 109
A.3 NNs for the retrieval of nitrogen dioxide columns from satellite UV/VIS simulated radiances . . . 110
A.3.1 Sensitivity analysis . . . 110
A.3.2 Algorithm design and optimization . . . 110
A.3.3 Results . . . 111
A.4 Conclusion . . . 111

B Grid technology for the validation of NNs algorithms for ozone retrieval 112

Bibliography 115

List of Figures 125

List of Tables 130

Acronyms 131

Symbols 135

Summary

Climate changes and atmospheric pollution are currently topical issues given their possible dramatic effects from the health, social and economical points of view. Assessing the causes and possible adaptation/mitigation strategies is a challenge in modern science. To understand and quantify the anthropic role in such changes is of a particular interest to depict future scenarios and to warn politicians about local and global intervention in emissions control.

Ozone is one of the most important trace gases in the Earth's atmosphere. It is mainly present in the stratosphere, with only 10% in the troposphere. Despite its small amount, (2-7)$\cdot 10^{-3}$ % in molar fraction, the solar radiation at wavelengths below 310 nm does not reach the Earth surface because of the large absorption cross sections characterizing ozone molecules at those wavelengths. Variations in the stratospheric ozone content may play a dramatic role in a possible increase of the surface UV radiation. The discovery of the Antarctic ozone hole, i.e. a considerable reduction of ozone in the polar stratosphere, was a dramatic evidence of the effects of anthropogenic emissions on the ozone layer. Human activity is likely responsible also for tropospheric ozone enhancements caused by the photochemistry associated to industrial emissions involving ozone precursors as the nitrogen dioxide. The effect of these variations at lower altitudes, with respect to background values, have been estimated to be the third largest source of the greenhouse effect.

To support interpretation of the atmospheric phenomena, as well as interactions with the oceans and the ground, a constant and systematic monitoring of several atmospheric parameters, and with a good spatial coverage, is crucial. In this framework, global and systematic space-based observations of the atmospheric composition and its variations in time and space play a major role. Satellite measurements of atmospheric parameters has a proven and recognized effectiveness for such tasks. The advantage of atmospheric sounding performed from space, with respect to ground based techniques, lies in the very high number of available measurements per day and in the global coverage of the Earth, allowing for a detailed and continuous investigation of the atmospheric state.

A number of different techniques are available , using different instruments, bands and viewing geometries. For all of them, a major problem is related to the intrinsically indirect nature of the measurements, as they result from the interaction between the electromagnetic radiation and the atmospheric constituents. The retrieval phase requires the solution of an inverse problem, which is never trivial and can be computationally very intensive, especially for this kind of nonlinear problems. A significant concurrent requirement is an adequate spatial resolution. Horizontal resolution is very hard to achieve by limb measurements, while it can be attained by nadir observations. Nadir measurements, however, can have poor vertical resolutions, and the inversion problem can be particularly computationally expensive.

In this thesis we present novel approaches to the inversion of the nadir UV/VIS satellite Earth's radiance spectra for the retrieval of height resolved ozone information. The considered platforms are ESA EnviSat-SCIAMACHY and NASA-Aura OMI, which are particularly suited for these tasks owing to their combined high spectral and spatial resolutions. Both ozone concentration profiles and tropospheric ozone column are retrieved by means of NNs algorithms. NNs are made of interconnected elementary processing units, called neurons, and can learn from a training dataset; they were proven to be robust on systematic errors and calibration uncertainties on the input measurements vector, and they are likely to work better than OE with respect to cloudy scenarios or in presence of significant aerosols burdens. Once a net is trained it can perform retrievals in real-time.

The work has been fulfilled in the framework of the GeoInformation PhD Programme of Tor Vergata University of Rome, and with the NASA - Goddard Space Flight Center in Greenbelt, MD, USA.

Pasquale Sellitto: sellitto@disp.uniroma2.it

Chapter 1

Atmospheric ozone measurements

1.1 Atmospheric structure and composition

The Earth's atmosphere is the layer of gases and suspended solid and liquid particles surrounding the planet Earth; it is retained by Earth's gravity. Table 1.1 summarizes the molar fraction of major atmospheric gasses.

As it is possible to notice, over the 99% of the mass of the atmosphere is composed by the N_2 and the O_2. Although representing, collectively, only the $\sim 1\%$ of the atmospheric mass, some of the so-called *trace gases* have a major role in thermodynamical, chemical and radiative phenomenology of the Earth's atmosphere. Other important atmospheric constituents are the aerosols, microscopic ($10^{-3} - 10^{2}\,\mu$m) liquid and solid particles suspended in the air that can absorb and/or scatter solar and terrestrial radiation within various spectral bands; the high-degree variation in time and space of their optical and

Gas	Molar fraction (%)
N_2	78.08
O_2	20.95
A	0.93
CO_2	0.03
Ne	0.00182
He	0.00052
CH_4	0.00015
Kr	0.00012
H_2	0.00005
NO_2	0.00005
O_3	$(2\text{-}7)\cdot 10^{-3}$
H_2O	$(0\text{-}4)\cdot 10^{-3}$

TABLE 1.1: Atmospheric composition: molar fraction of the major atmospheric gasses [1].

morphological properties can cause a significant uncertainty to the climatic system and the Earth's energy balance [1].

Atmospheric constituents can absorb or scatter solar and terrestrial radiation. In these processes, energy can be stored in the atmosphere and then re-emitted as IR radiation. All these phenomena, in conjunction with surface and ocean interaction with radiation, take place to maintain a *radiative balance* between incoming and outgoing energy in dependence of which the Earth climatic system is relatively stable.

Interacting radiative, dynamical and chemical processes determine the structure of the atmosphere. The atmosphere can be divided into several different vertical *layers* possessing very distinct chemical, physical and dynamical properties. The primary way to display this structure is to look at the average temperature profile of the atmosphere. It is possible to identify regions in which the vertical temperature gradient has the same sign. Between layers with opposite vertical temperature gradients, it is possible to identify *pauses* in which the gradient is approximately zero. Layers and pauses of the Earth atmosphere are enumerated and their properties briefly described in the following:

- Troposphere - The vertical temperature gradient is negative and its magnitude is $\sim 5\,\mathrm{K/km}$ on average [2]. Atmospheric circulation is dominated by thermal and mechanical exchanges with the surface. Convection of warmer air from lower levels is the main phenomenon for temperature control, while IR absorption/emission of some gases as well as air masses dynamics and water phase changes may have a role in the energy balance. Within the troposphere most of the atmospheric mass can be found and here meteorological phenomena occur. The troposphere is $\sim 10\,\mathrm{km}$ deep on average; it is deeper at the tropics, where can reach the altitude of $\sim 20\,\mathrm{km}$, and shallower at the poles, where can be as low as $\sim 7\,\mathrm{km}$. Its height also depends on the season.

- Tropopause - The vertical temperature gradient goes to zero and slowly changes sign. Here the temperature is relatively low, $\sim 190 - 230\,\mathrm{K}$ on average [2] and condensation of water vapor is favored, generally preventing this species from diffusing upwards. The troposphere height can vary depending on the variations of thickness of the troposphere.

- Stratosphere - The vertical temperature gradient is positive and its magnitude is $\sim 2\,\mathrm{K/km}$ on average [2]. The stratification of the air masses prevent their vertical motion. Absorption of UV radiation by the ozone is the main phenomenon for temperature control and energy balance, if we neglect heath transport due to the (mainly horizontal) air masses motion. Starting from the tropopause, the stratosphere can reach altitudes as high as $\sim 55\,\mathrm{km}$.

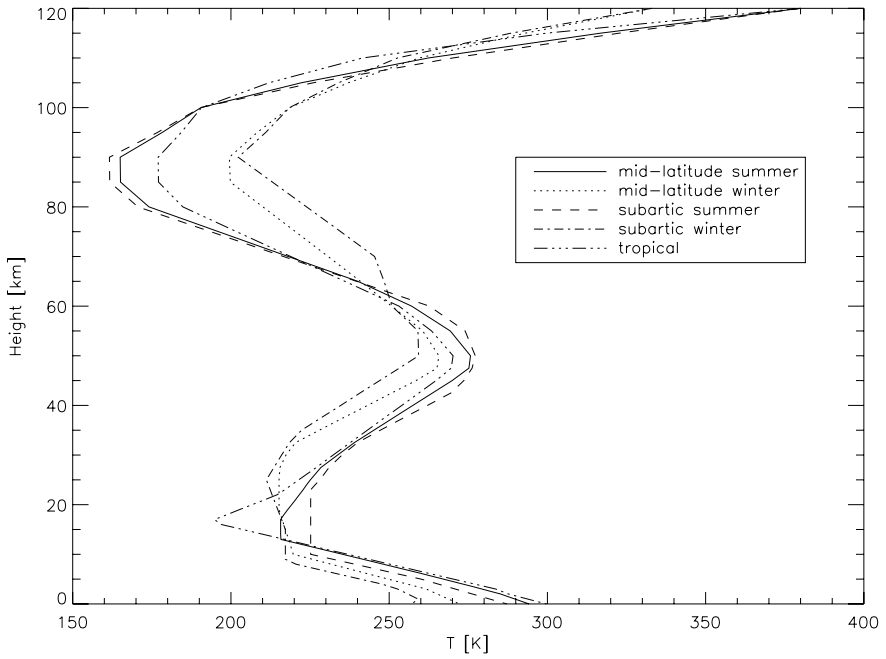

FIGURE 1.1: Standard thermal structure of the atmosphere at different latitudes and seasons. Elaborated from data taken from [3].

- Stratopause - The vertical temperature gradient goes to zero and then changes sign.
- Mesosphere - The vertical temperature gradient is negative. The UV absorption is relatively weak owing to lower gas concentrations. Starting from the stratopause, this layer can reach altitudes of $\sim 90\,\text{km}$ [2].
- Mesopause - The vertical temperature gradient goes to zero and then changes sign.
- Termosphere - The vertical gradient is positive and temperatures can reach values as high as $1000-2000\,\text{K}$ [2]. Even if the gasses concentrations rapidly decrease with height, the absorption of UV radiation increase for the dissociation of the oxygen molecule, leading to dramatically high temperatures. In this area the atmosphere has a quasi-isothermal behavior and the species tend to stratify depending on their atomic/molecular masses.

A vertical thermal structure of the atmosphere is depicted in Fig. (1.1).

1.2 Ozone in the Earth's atmosphere

1.2.1 Introduction

Ozone (O_3) is an allotrope of oxygen; it is mainly produced in stratosphere, from reactions involving the absorption of relatively high energy solar UV radiation. Atmospheric ozone has a recognized key-role in absorbing the harmful solar UV photons at short wavelengths, and its vertical distribution affects significantly the chemical and physical processes in a large part of the atmosphere. Despite the small amount of ozone in the Earth's atmosphere, the solar radiation at wavelengths below 310 nm does not reach the lower atmospheric layers because of the large absorption cross sections of the ozone at those wavelengths (see Sec. (1.2.4)). In this way the ozone layer acts as a filter for the harmful UV solar radiation and contributes to the radiative balance of the stratosphere and the upper troposphere. Although its presence in stratosphere is of a crucial importance for life on Earth, an enhancement of ozone in the troposphere may be a danger for human beings, for animals and vegetation. The ozone is highly reactive with several molecules and it can reduce human lungs capacity, worsen pre-existing cardiac and pulmonary pathologies and it can interact with crop and vegetation growing. In addition, the ozone plays a fundamental role in the tropospheric radiative balance: tropospheric ozone is a direct greenhouse gas [1] and it is considered to be the third most important gas in global warming, in terms of radiative forcing, after the carbon dioxide and methane [1]. Furthermore, tropospheric ozone is a source for the hydroxyl radical, which controls the abundance and distribution of many atmospheric constituents, including greenhouse gases [4].

An average vertical concentration profile of ozone is reported in figure 1.2. As it is possible to notice, about 90% of the total ozone is in the stratosphere, while the remaining 10% is in troposphere. Ozone profiles at different latitudes and seasons are shown in figure 1.3.

In the past few decades the public concern regarding the impact of human activities on the Earth's atmosphere has significantly grown, and a considerable effort has been made by researchers in order to understand the role of anthropogenic gas emissions in the atmospheric chemistry and its connections with the stratospheric ozone depletion, the global climate change and the increasing pollution of the troposphere. Ozone studies are of a particular interest for the understanding of both surface UV flux increase and the global warming. Efforts for a more complete depiction of ozone dynamics both in the stratosphere and in the troposphere are crucial to address the human impact on climate and to monitor the effects of possible intervention for mitigation. Long-term systematic observations of height resolved ozone concentrations from satellite platform may help

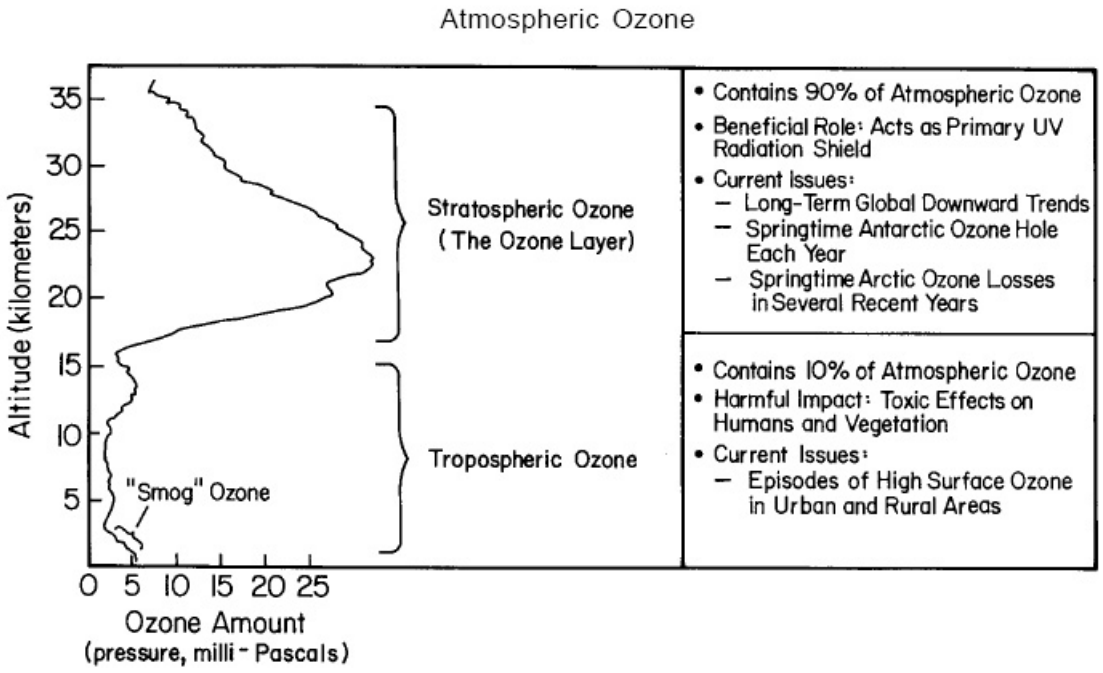

FIGURE 1.2: A standard ozone profile at mid-latitudes. Figure taken from [5]

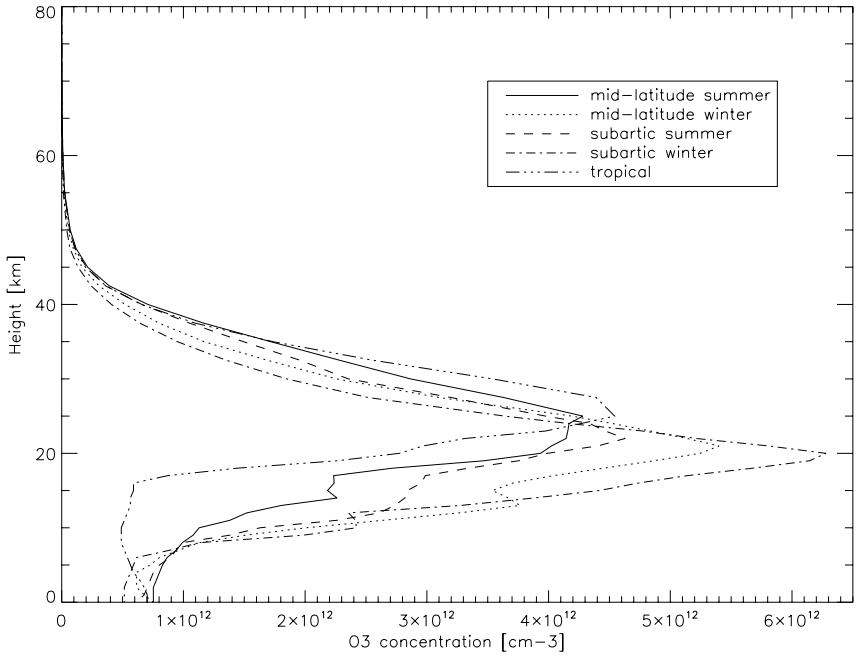

FIGURE 1.3: Standard ozone concentration profiles at different latitudes and seasons. Elaborated from data taken from [3]

in this context. In Sec. (1.4) a general state of the art of this kind of measurement approach is given, and in Subsec.s (1.4.4.4) and (1.4.4.5) a specific description of existing techniques of satellite monitoring of ozone from nadir UV/VIS measurement is reported, as well as their advantages and weaknesses over other techniques. In the next few Sec.s we will briefly discussion ozone sources and sinks in both stratosphere and troposphere, and a spectroscopic characterization of this important trace gas.

1.2.2 Stratospheric ozone

1.2.2.1 Formation and removal mechanisms

Ozone concentrations in atmosphere are determined by the balance of formation, destruction and transport.

The ozone production in stratosphere is mainly due to the photo-dissociation of oxygen molecules triggered by the incidence of UV radiation at $\lambda < 242\,\text{nm}$:

$$\text{O}_2 + h\nu \longrightarrow 2\,\text{O}(^3P) \quad \text{if} \quad \lambda < 242\,\text{nm} \tag{R 1.1}$$

$$\text{O}_2 + h\nu \longrightarrow \text{O}(^3P) + \text{O}(^1D) \quad \text{if} \quad \lambda < 175\,\text{nm} \tag{R 1.2}$$

The oxygen atoms react rapidly with the oxygen molecules to form ozone. For this reaction a third body species M is required to acquire the kinetic energy in excess:

$$\text{O} + \text{O}_2 + \text{M} \longrightarrow \text{O}_3 + \text{M} + 24\,\text{kcal/mol} \tag{R 1.3}$$

In absence of M, an unstable vibrational state of O_3 is formed, and rapidly dissociate. In any case, O_3 can dissociate by absorbing UV radiation and then it can react with the atomic oxygen as in Reac.s (R 1.4) and (R 1.5).

$$\text{O}_3 + h\nu \longrightarrow \text{O} + \text{O}_2 \quad \text{if} \quad 240\,\text{nm} < \lambda < 320\,\text{nm} \tag{R 1.4}$$

$$\text{O}_3 + \text{O} \longrightarrow 2\,\text{O}_2 + 94\,\text{kcal/mol} \tag{R 1.5}$$

The atomic oxygen can also re-combine to produce molecular oxygen in the following way:

$$\text{O} + \text{O} + \text{M} \longrightarrow \text{O}_2 + \text{M} + 118\,\text{kcal/mol} \tag{R 1.6}$$

Reac.s (R 1.1-R 1.6) are collectively known as the *Chapman cycle* and lead to a steady state, i.e. the rate of ozone loss is equal to the rate of ozone formation [6].

Additional loss cycles are attributed to highly reactive catalysts X, mainly produced in stratosphere by photolytic decomposition:

$$X + O_3 \longrightarrow XO + O_2 \tag{R 1.7}$$

$$XO + O \longrightarrow O_2 + X \tag{R 1.8}$$

giving:

$$O + O_3 \longrightarrow 2\,O_2$$

Important catalysts have been identified as the HO_x and NO_x [7, 8] or halogen species as the Cl and the Br [7]. The OH and H gases are mainly generated by the decomposition of methane and water vapor, the NO and NO_2 originate from N_2O produced in the biosphere, the chlorine and ClO come from industrial products as the chlorofluorocarbons (CFCs), and the bromine is generated by Halon, another industrial product.

A specific discussion on the so-called *ozone hole* phenomenology will be now given. Under normal circumstances, almost all of the chemically active (stratospheric) chlorine is in the form of HCl or $ClONO_2$. Br compounds are much less abundant in the atmosphere than Cl compounds, but the related loss cycles are more efficient per molecule due to the much lower fraction in (inactive) reservoir form [9]. Significant reductions in lower stratospheric O_3 at high latitude are well known from decades [10]. The phenomenon has been observed in both hemispheres, and more consistently in the Antarctic. The principal cause has been identified in the enhanced release of active chlorine from reservoir species, promoted by heterogeneous multi-phase reaction on Polar Stratospheric Cloud (PSC) particles [11]. PSC formation requires the very low temperatures (< 200 K) in the polar vortex, when, in the absence of sunlight, the stratospheric air masses cool and descend, developing a circulation mechanism which produces the vortex. The core of the vortex becomes steadily isolated from the air outside and then persists until warming and mixing occurs in the spring. Reactions, including the following, occur much more readily when the second reactant on the left hand side is absorbed onto the surface of a PSC particle (denoted here by subscript (s)) [9]:

$$ClONO_2 + HCl_{(s)} \longrightarrow Cl_2 + HNO_{3(s)} \tag{R 1.9}$$

$$ClONO_2 + H_2O_{(s)} \longrightarrow HOCl + HNO_{3(s)} \quad \text{(R 1.10)}$$

$$HOCl + HCl_{(s)} \longrightarrow Cl_2 + H_2O \quad \text{(R 1.11)}$$

The chlorine species produced in each case rapidly photolyze, given sun-light in the spring, releasing Cl which reacts with O_3:

$$Cl + O_3 \longrightarrow ClO + O_2 \quad \text{(R 1.12)}$$

Once the concentration of ClO reaches a certain level, the following cycle rapidly destroys O_3:

$$ClO + ClO + M \longrightarrow ClOOCl + M \quad \text{(R 1.13)}$$

$$ClOOCl + h\nu \longrightarrow ClOO + Cl \quad \text{(R 1.14)}$$

$$ClOO + M \longrightarrow Cl + O_2 \quad \text{(R 1.15)}$$

$$(2\times) \qquad Cl + O_3 \longrightarrow ClO + O_2 \quad \text{(R 1.16)}$$

Reac.s (R 1.13-R 1.16), together, give:

$$2\,O_3 \longrightarrow 3\,O_2$$

The described phenomenon brings to the mentioned ozone depletion at high latitudes, and in particular in Antarctica, which leads to a sensible reduction of ozone in the polar stratosphere and to a possible surface UV flux enhancement [7]. As an example, Fig. (1.4) shows the ozone concentration profile in a ozone hole situation. Please refer to the caption for further details.

1.2.2.2 Spatial and temporal variabilities

Here we want to discuss the average global features and the variabilities over the globe and the seasons of the total ozone. Owing to the fact that nearly the 90% of the ozone is in the stratosphere, patterns in total ozone can be representative of the stratospheric content. A further description of the tropospheric patterns and trends is given in section 1.2.3.2.

The Chapman cycle formulation of stratospheric ozone photo-chemistry leads to an expected distribution with a maximum at the equator and a minimum at the poles. The

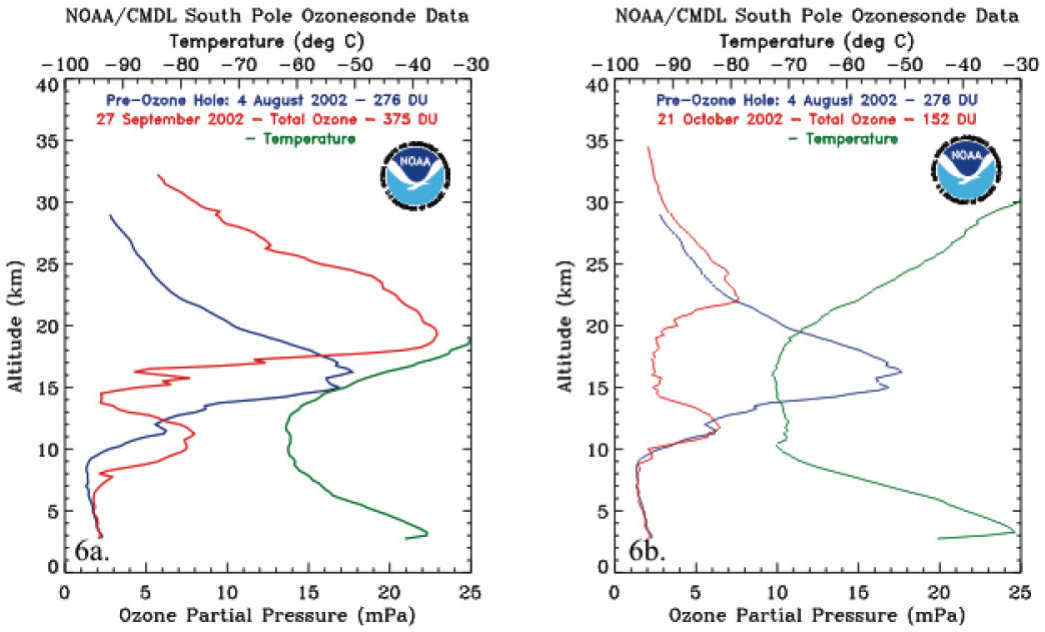

FIGURE 1.4: Two ozone soundings made at the South Pole in September and October 2002 (red line), compared to a pre-ozone hole profile taken on August 2002 (blue line). A temperature profile is also reported (green line). Figure taken from [12].

ozone production, in fact, is likely controlled by the photonic flux at sensible wavelengths, giving a maximum ozone production at lower latitudes, where the photo-chemistry is maximum due to higher illumination. The observed spatial distribution of total ozone, on the opposite, is maximum at sub-polar locations and minimum at the equator, on average [1]. A depiction of these observations is given in Fig. (1.5), where global mean total ozone for January, April, July and October 2008 is reported. Here it is also possible to see that a maximum occurs in April at about 70°, and similarly in spring for the Southern Hemisphere.

The discrepancy between the Chapman theory and the observations is due to the fact that the theory doesn't consider air masses circulation and transport phenomena. The maximum at higher latitudes, in fact, depends on the ozone transport from the higher stratosphere over the equatorial region, where the maximum of the ozone production can be located, to the lower and mid stratosphere over the polar region [2]. The northern high latitudes maximum is more marked than the analogous maximum in the southern hemisphere.

Finally, a closer view to the peculiar Antarctic ozone hole phenomenon is given in Fig. (1.6), where the evolution of the ozone hole in the period 1995-2004 is shown. The ozone hole is also visible in Fig. (1.5(d)).

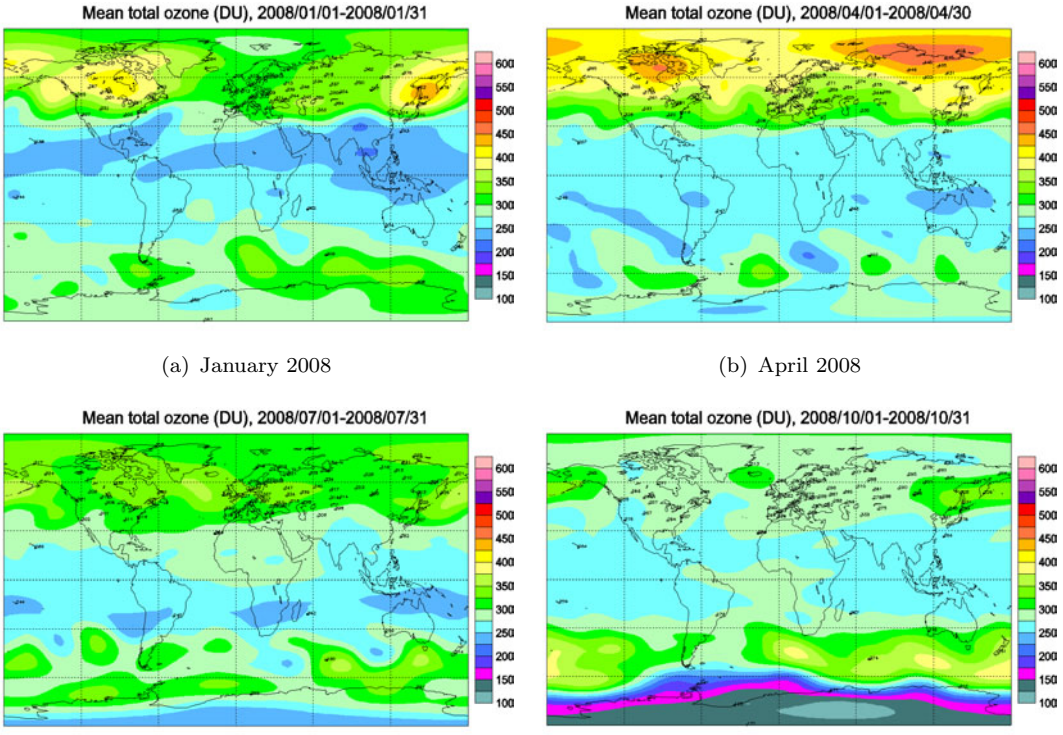

(a) January 2008

(b) April 2008

(c) July 2008

(d) October 2008

FIGURE 1.5: Global mean total ozone for different months in 2008. Elaborated from data taken from [13].

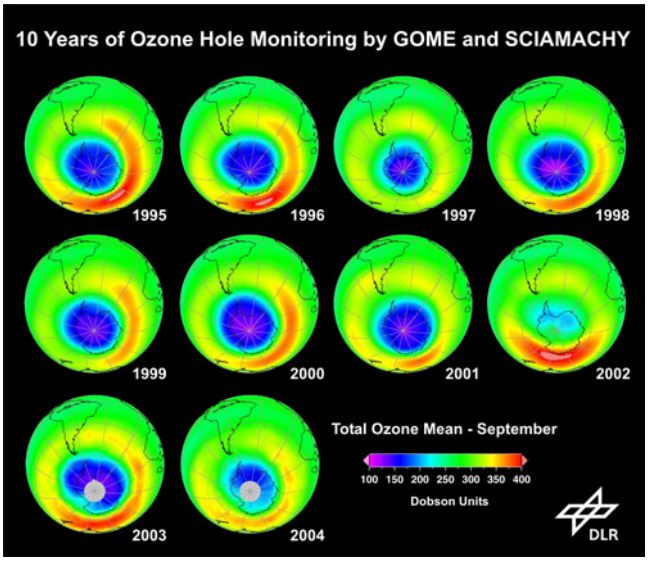

FIGURE 1.6: The Antarctic ozone hole evolution in the period 1995-2004: September's concentrations taken from GOME and SCIAMACHY data. Courtesy of DLR.

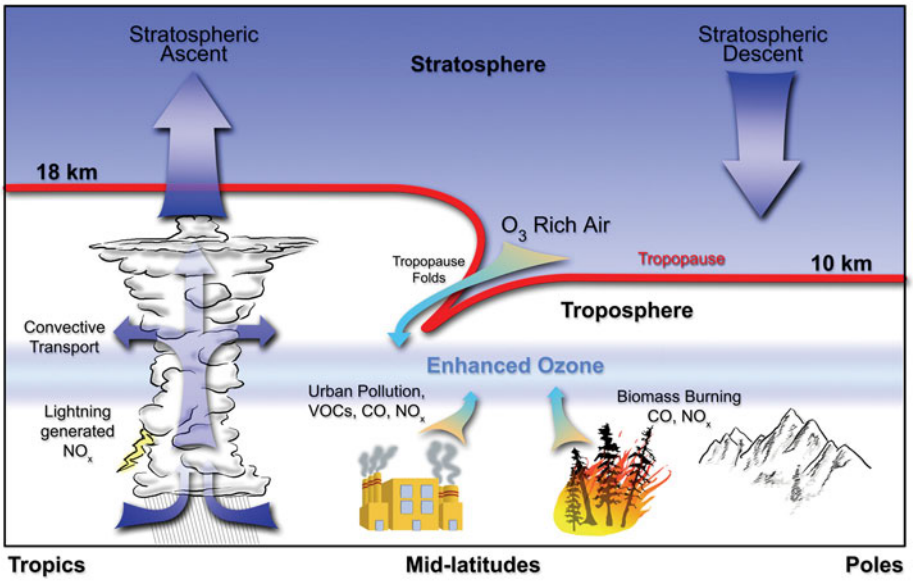

FIGURE 1.7: Scheme of the major ozone transport, formation and removal phenomena. Courtesy of NASA.

1.2.3 Tropospheric ozone

1.2.3.1 Formation and removal mechanisms

The two main sources of ozone in troposphere are Stratosphere-Troposphere Exchanges (STE), and chemical and photochemical reactions occurring in the boundary layer [14]. Figure 1.7 shows a scheme of these as well as some other minor mechanisms.

In the following we will examine more thoroughly the two mentioned components.

- STE

  The ozone has its major source in the mid stratosphere. Air masses can move down towards the low stratosphere by adiabatic circulation. Lower stratospheric levels, that are richer in ozone, can exchange air masses with the upper troposphere allowing the advection of ozone. An estimation of ozone flux in troposphere for STE is 360-820 Tg/year, globally [15]. STE-related transport of ozone is more effective in late winter and in spring, while the average lifetime of ozone in the free troposphere is about 1-4 months. It is expected that STE contribution to tropospheric ozone concentrations is dependent on latitude, tropopause height and season.

- Photochemistry

Another source of ozone in the troposphere is related to the photochemical activity involving CO, CH_4 and Volatile Organic Compounds (VOCs), in presence of nitric oxides [16]. These species are usually referred as *ozone precursors*.

The reactions involving CO are in the following:

$$CO + OH \xrightarrow{O_2} CO_2 + HO_2 \quad \text{(R 1.17)}$$

$$HO_2 + NO \longrightarrow OH + NO_2 \quad \text{(R 1.18)}$$

$$NO_2 + h\nu \xrightarrow{O_2} NO + O_3 \quad \text{(R 1.19)}$$

giving, at neat:

$$CO + 2\,O_2 \longrightarrow CO_2 + O_3 \quad \text{(R 1.20)}$$

The contribution of CH_4 is given by the following cycle:

$$CH_4 + OH \longrightarrow CH_3 + H_2O \quad \text{(R 1.21)}$$

$$CH_3 + O_2 + M \longrightarrow CH_3O_2 + M \quad \text{(R 1.22)}$$

$$CH_3O_2 + NO \longrightarrow CH_3O + NO_2 \quad \text{(R 1.23)}$$

$$CH_3O + O_2 \longrightarrow CH_2O + HO_2 \quad \text{(R 1.24)}$$

$$CH_2O + h\nu \xrightarrow{O_2} CHO + O_2 \quad \text{(R 1.25)}$$

$$CHO + O_2 \longrightarrow CO + HO_2 \quad \text{(R 1.26)}$$

$$CO + OH \xrightarrow{O_2} CO_2 + HO_2 \quad \text{(R 1.27)}$$

$$(4\times) \qquad HO_2 + NO \longrightarrow OH + NO_2 \quad \text{(R 1.28)}$$

$$(5\times) \qquad NO_2 + h\nu \xrightarrow{O_2} NO + O_3 \quad \text{(R 1.29)}$$

giving, at neat:

$$CH_4 + 10\,O_2 \longrightarrow CO_2 + H_2O + 5\,O_3 + 2\,OH \quad \text{(R 1.30)}$$

The VOCs can contribute in the following way:

$$VOC_1 + 4\,O_2 + 2\,h\nu \longrightarrow VOC_2 + H_2O + 2\,O_3 \quad \text{(R 1.31)}$$

The ozone in troposphere can be removed by reactions involving HO_x:

$$HO_2 + O_3 \longrightarrow OH + 2\,O_2 \quad \text{(R 1.32)}$$

$$OH + O_3 \longrightarrow HO_2 + O_2 \quad \text{(R 1.33)}$$

The net flux of tropospheric ozone due to photochemistry has been estimated as 500-700 Tg/year [17]. The balance of Reac.s (R 1.17-R 1.33) is given by the abundance of the ozone precursors and sinks. In particular the NO_x can drive tropospheric ozone concentrations. Tropospheric NO_x originates predominantly from fossil fuel combustion . Natural sources are about of a factor 3 lower and include soil emissions and lightnings [18]. Although the NO_x have a short lifetime (few hours near the ground, few days at higher altitude), they can be transported for large distances from localized sources, via reservoir species (e.g. peroxyacetylnitrate - PAN). Tropospheric convection can be important to transport the NO_x to high altitude and low temperature regions, where both NO_x and PAN are more stable [19]. Ozone production is strongly favored in urban regions under high-pressure meteorological conditions, since the vertical stability (associated with a temperature inversion) allows the primary pollutants, including NO_x and hydrocarbons, to accumulate. Such conditions typically occur in summer, when photolysis rates are also enhanced. High concentrations of NO_x and VOCs are also present in plumes from biomass-burning, which regularly occurs (particularly in tropical regions) during the summer season [1].

1.2.3.2 Spatial and temporal variabilities

Several studies pointed out a deviation of the tropospheric ozone content from background concentrations [1]. Temporal trends showed remarkable geographical differences with respect to average values since the '70s in the northern hemisphere, with possible enhancements in Europe, some depletion in Canada and only small variations in the United States [14]. Some studies also showed an enhancement of the surface ozone concentrations in the southern hemisphere [20]. In general the most of our knowledge about long-term variations of ozone in troposphere is inferred by ozonesondes measurements. Ozonesondes offer the best record of ozone throughout the troposphere, although measurements at many stations are made only weekly (infrequently for a variable gas like ozone). Weekly continuous data since 1970 are available from only nine stations in the latitude range 36N to 59N [21]. Different trends are seen at different locations for different periods. Most stations show an increase from 1970 to 1980, but no clear trend from 1980 to 1996. Recent measurements campaigns highlighted how the anthropic production of ozone precursors can have led to a significant enhancement of photo-chemically

produced ozone at lower levels at big urban and industrial sites and, owing to continental scale transport phenomena, to variations of the balance of tropospheric ozone concentrations over extended areas [1]. In any case a clear and complete characterization of tropospheric ozone global trends are still to be achieved, owing to the multiplicity of factors involved, the high spatial and temporal variabilities and the sparsely sited measurements locations (e.g. ozonesonde stations). Nevertheless it is recommendable an international control agreement about industrial emissions capable to interact with low level ozone concentrations.

The radiative forcing due to the observed enhancements of tropospheric ozone since the pre-industrial era is estimated as $+0.35 \pm 0.15\,\mathrm{W/m^2}$, so about $10 - 20\%$ of the total radiative forcing in the same time interval [22]. With the present tropospheric ozone growing rate at mid-latitudes locations it is possible to prefigure a possible scenario of $+2\,\mathrm{W/m^2}$ by 2100 [1].

1.2.4 Spectroscopic characterization of the ozone

Ozone molecules can absorb radiation within solar and terrestrial spectra. Let's now consider the spectral bands of interest in the field of remote sensing of ozone. The main ozone absorption bands in the UV, VIS and IR are the following:

- Hartley band (200 nm$< \lambda <$310 nm);
- Huggins bands (310 nm$< \lambda <$350 nm);
- Chappuis band (480 nm$< \lambda <$610 nm);
- Wulf bands (610 nm$< \lambda <$768 nm);
- roto-vibrational band at $\sim 9.6\ \mu$ m.

In figure 1.8(a) the spectral absorption cross sections of ozone at $T = 298.0\,\mathrm{K}$ are reported for UV and VIS bands. Figure 1.8(b) shows the spectral differences of the cross sections at different temperatures compared with the cross section at 298.0 K. As it is possible to notice there's a remarkable temperature dependence of the absorption features of ozone in the UV bands, while no temperature dependence is reported in the VIS.

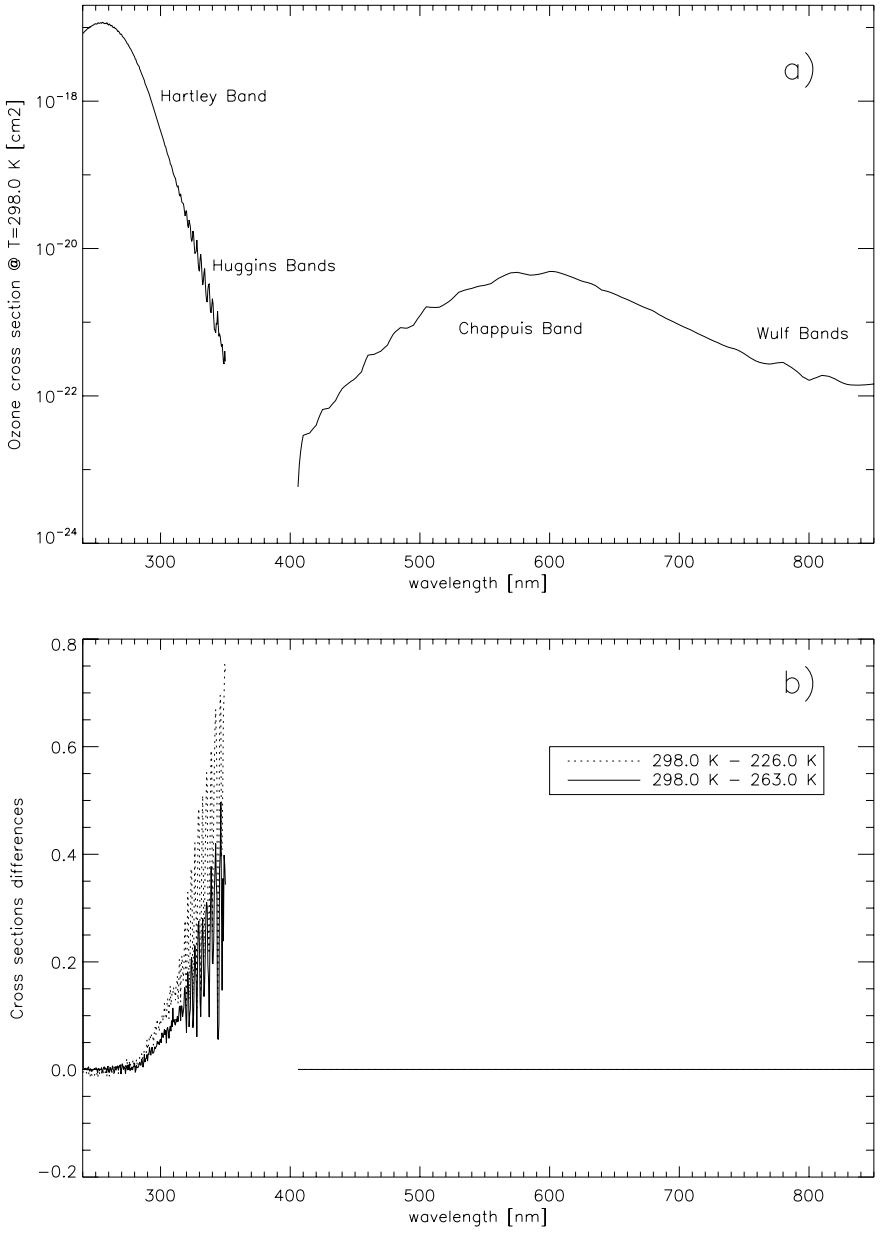

FIGURE 1.8: UV and VIS ozone absorption spectrum at T=298.0 K (a), and spectral differences of the cross sections at different temperatures (b). Elaborated from data taken from [23]

.

1.3 Radiative transfer through the Earth's atmosphere

1.3.1 Definition of radiometric parameters of interest

In this subsection the main parameters for radiative transport processes description will be defined. Please refer to [24] for more details.

The *spectral radiant flux* is defined as the rate of flow of electromagnetic energy across a surface dA whose normal versor is $\mathbf{n}_0$, at a given frequency:

$$F(\mathbf{r}, \mathbf{n}_0, \nu) = \frac{d^3E}{dt \cdot dA \cdot d\nu} \tag{1.1}$$

The spectral radiant flux units are [W/(m^2 Hz)]. The flux is dependent on the orientation of the elementary area: it is > 0 if energy is outgoing from the surface, viceversa if it is incoming. It is also possible to define two *hemispheric fluxes*, $F^{\uparrow}(\mathbf{r}, \mathbf{n}_0, \nu)$ and $F^{\downarrow}(\mathbf{r}, \mathbf{n}_0, \nu)$, both > 0, as outgoing from or incoming to the surface, respectively. The net spectral radiative flux is then:

$$F(\mathbf{r}, \mathbf{n}_0, \nu) = F^{\uparrow}(\mathbf{r}, \mathbf{n}_0, \nu) - F^{\downarrow}(\mathbf{r}, \mathbf{n}_0, \nu) \tag{1.2}$$

The quantity $F^{\downarrow}(\mathbf{r}, \mathbf{n}_0, \nu)$ is also called *irradiance*. It is also possible to define the irradiance in the wavelengths domain:

$$F(\mathbf{r}, \mathbf{n}_0, \lambda) = F(\mathbf{r}, \mathbf{n}_0, \nu) \cdot \frac{c}{\lambda^2} \tag{1.3}$$

To take into account the angular dependency of the energy flux the idea of *radiance* is introduced. Analogously to the definition of irradiance, we define a quantity d^4E as the energy that flows in a solid angle $d\Omega$ in the direction Ω in the time interval dt at the frequency interval $d\nu$. The radiance is:

$$L(\mathbf{r}, \Omega, \nu) = \frac{d^4E}{\cos\vartheta \cdot d\Omega \cdot dt \cdot dA \cdot d\nu} \tag{1.4}$$

The radiance units are [W/(m^{2}Hz sr)]. Eq. (1.5) links the radiance and the irradiance.

$$F(\nu) = \iint_{4\pi} L(\Omega, \nu) d\Omega = \int_0^{2\pi} \int_0^{\pi} L(\vartheta, \varphi, \nu) \cdot \cos\vartheta \cdot d\vartheta \cdot d\varphi \tag{1.5}$$

Finally we introduce the *reflectance* of a given surface as the ratio between reflected/scattered radiance and incident irradiance, in a given direction $\mathbf{s}_0$:

$$R(\mathbf{s}_{0i}, \mathbf{s}_{0r}, \nu) = \frac{dL_r(\mathbf{s}_{0r}, \nu)}{dF_i(\mathbf{s}_{0i}, \nu)} = \frac{dL_r(\mathbf{s}_{0r}, \nu)}{L_i(\mathbf{s}_{0i}, \nu) \cdot \cos\vartheta_i \cdot d\Omega_i} \tag{1.6}$$

1.3.2 Radiative transfer equation

Starting from the definitions given in the previous section, we now want to analytically describe the problem of transport of radiation in Earth's atmosphere. We want to derive the variations in the incident spectral radiance $L(\mathbf{r}, \mathbf{s}_0, \nu)$ that crosses a cylindrical volume of atmosphere with depth s in the direction $\mathbf{s}_0$.

The contributions to the variations in the radiance can be attributed to different sources:

- absorption of the medium;
- scattering in different directions;
- thermal emission of the medium;
- scattering from different directions.

Let's initially consider the different sources separately.

We first neglect the scattering contribution. The absorption and thermal emission contributions can be written as:

$$dL(\mathbf{s}_0, \lambda) = -k_{\text{abs}}(\lambda) \cdot \rho \cdot L(\mathbf{s}_0, \lambda) \cdot ds + k_{abs}(\lambda) \cdot \rho \cdot B(\lambda, T) \cdot ds \tag{1.7}$$

where $k_{\text{abs}}(\lambda)$ is the absorption coefficient, ρ is the medium density and $B(\lambda, T)$ is the *black body radiance* at the temperature T.

We now consider the scattering contribution and neglect the absorption and thermal emission. The loss of energy due to scattering and the positive contribution from different directions is:

$$dL(\vartheta, \varphi, \lambda) = -k_s(\lambda) \cdot \rho \cdot L(\vartheta, \varphi, \lambda) \cdot ds + \frac{k_s(\lambda) \cdot \rho}{4\pi} \int_0^{2\pi} \int_0^{\pi} P(\vartheta, \varphi, \vartheta', \varphi', \lambda) \cdot L(\vartheta', \varphi', \lambda) \cdot \sin\vartheta' \cdot d\vartheta' \cdot d\varphi' \cdot ds \tag{1.8}$$

where $k_s(\lambda)$ is the scattering coefficient and $P(\lambda)$ is the *phase function* and identifies how much radiation is scattered from an incoming direction (ϑ', φ') to a direction (ϑ, φ).

So, with some simplifications, a general form of the radiative transport equation can be the following:

$$\frac{dL(\lambda)}{d\tau(\lambda)} = -L(\lambda) + \sigma(\lambda) \tag{1.9}$$

where $\sigma(\lambda)$ is the *source function* and takes the general form:

$$\sigma(\lambda) = \frac{\tilde{\omega}_0}{4\pi} \int_0^{2\pi} \int_0^{\pi} P(\vartheta, \varphi, \vartheta', \varphi', \lambda) \cdot L(\vartheta', \varphi', \lambda) \cdot \sin\vartheta' \cdot d\vartheta' \cdot d\varphi' + (1 - \tilde{\omega}_0) \cdot B(\lambda, T) \tag{1.10}$$

The *single scattering albedo* $\tilde{\omega}_0$ is the ratio of scattering and extinction components in a radiation beam. We also introduced the *optical depth* τ, which is defined as follows:

$$\tau(\lambda) = \int_{s_0}^{s'} k_{\text{ext}}(\lambda) ds' \tag{1.11}$$

1.4 Height resolved atmospheric ozone measurements

Several methods to measure atmospheric ozone profiles and to retrieve height resolved information exist. Here we want to offer a state-of-the-art discussion on such methods; this is not intended to be a comprehensive survey but a useful summary to highlight the basic characteristics of the various ozone measurement techniques.

As for the measurement of other atmospheric parameters, atmospheric ozone measurement techniques can be divided into two main classes:

- *in situ* measurement techniques;
- *remote sensing* measurement techniques.

This latter class can be further divided into techniques with ground-based, satellite-borne and air-borne instrumentation.

1.4.1 In situ techniques

In situ measurements deal with instrumentation in contact with the object of interest. In the case of the ozone, the most typical in situ technique is related to ozonesondes (OS) [25].

The ozonesonde is a lightweight, balloon-borne instrument that is mated to a conventional meteorological radiosonde. As the balloon carrying the instrument package ascends through the atmosphere, the OS telemeters to a ground receiving station information on ozone and standard meteorological quantities such as pressure, temperature and humidity. The balloon will ascend to altitudes of about 35 km or about 4 hPa before it bursts. The heart of the ozonesonde is an electrochemical concentration cell (ECC) that senses ozone as is reacts with a dilute solution of potassium iodide to produce a weak electrical current proportional to the ozone concentration of the sampled air. Air containing ozone is directed to one of the two platinum semi-elements, and the following reaction is triggered:

$$2\,\mathrm{KI} + \mathrm{O_3} + \mathrm{H_2O} \longrightarrow 2\,\mathrm{KOH} + \mathrm{I_2} + \mathrm{O_2}$$

The produced iodine, on contact with the platinum cathode, reduces in the following way:

$$\mathrm{I_2} + 2\,\mathrm{e^-} \xrightarrow{\mathrm{Pt}} 2\,\mathrm{I^-}$$

Iodine ions produce an electric current which is proportional to the ozone concentration.

Ozonesondes provide accurate measurements with a very high vertical resolution. The main problem is the local nature of the measurements and high financial costs. The OSs are launched in a limited number of stations and typically at northern hemisphere mid-latitudes. In addition, differences in stations operations and changes in the employed technology limit the long term consistency of the method, especially when data from more than one station have to be compared. Usually OSs operates in networks as the World Ozone and Ultraviolet radiation Data Center (WOUDC) [26] or the Southern Hemisphere ADditional OZonesondes (SHADOZ) [20, 27].

1.4.2 Ground-based remote sensing techniques

Height resolved and/or integrated quantities of ozone from ground-based remote sensing stations can be retrieved by means of *passive* or *active* instruments. Among passive

instruments we can identify the Dobson [25] and Brewer [28] spectrophotometers, and the Systeme d'Analyse par Observation Zenithale (SAOZ) spectrometer [29]. An active instrument in this field is the LiDAR [30].

The total column ozone can be measured from the ground using UV-absorption spectroscopy. In particular, the two most common instruments are the spectrophotometers developed by G. Dobson and A. W. Brewer, respectively. The Dobson instrument is based on the differential absorption method in the UV band, where ozone exhibits strong absorption features. This method exploits the ratio of sunlight intensities at two wavelengths characterized by strongly different ozone absorption cross sections. The Brewer spectrometer is similar in principle to the Dobson, but the determination of the ozone column amount is obtained from a combination of five wavelengths in the UV spectral range. An analogous instrument is the SAOZ, a UV-VIS spectrometer which measures the solar radiation scattered at the zenith in the spectral range 300-600 nm.

The application of the Umkehr principle to Dobson-Brewer instrumentation enables the retrieval of ozone concentrations at 10 different altitude layers, giving an estimation of the ozone vertical profile [31]. The height-resolved ozone distribution can also be obtained by millimeter-wave radiometers , which exploit a different spectral range.

LiDAR instruments, which measure the attenuation and delay of a Rayleigh backscattered laser beam, have recently provided data of similar quality to the ozonesondes, spanning an altitude range of approximately 5-45 km [32]. Temporal sampling is potentially better than OS observations, but generally limited to cloud-free, night-time conditions.

1.4.3 Air-borne instruments

Air-borne techniques have some major advantages if compared to ground-based ones. These techniques allow the monitoring of extended areas; in addition, measurements can be directly done at the altitudes of interest and over regions that are difficult to cover by ground, as polar or tropical areas.

An interesting project that we want to mention here is the Air-Borne Lidar Experiment (ABLE), developed at "Sapienza" University of Rome [33]. This project aimed at the development of an air-borne LiDAR capable to take measurements at the typical upper troposphere/lower stratosphere altitudes.

1.4.4 Satellite-borne techniques

The orbits in which satellite-based ozone-profiling instruments can be successfully employed are limited to Low Earth Orbits (LEOs), with altitudes typically between 600 and 900 km. They generally provide a global coverage of the Earth's surface in few days.

Besides absorbing in the UV, O_3 has roto-vibrational spectral signature in the mid-IR (see Sec. (1.2.4)) and a pure rotational signature extending into millimeter-wave spectral range. Remote sensing instruments for measuring atmospheric ozone from space therefore rely on spectroscopic or radiometric techniques, depending on the spectral interval used to perform the measurements.

Active techniques for atmospheric ozone observations, which exploit an actively induced detected signal, are currently restricted to the Differential Absorption LiDAR (DIAL) technique [32, 34]. In recent years a number of remote sounding satellites have been equipped with LiDAR instruments, see e.g. the PARASOL [35] or the CALIPSO missions [36]; the technology, is mainly limited by the laser reliability and its power consumption.

Passive techniques, on the other hand, have been successfully experimented during the last decades. Ozone remote sensing from space can be performed by observing the Earth's natural radiation in different viewing geometries. The electromagnetic radiation reflected or emitted from the Earth's atmosphere and/or from the surface can be measured by looking in the nadir or limb direction (see figure 2.5). Nadir observations generally provide a good horizontal resolution and sampling, but a limited vertical resolution which depends on the optical properties of the atmosphere and on the possibility to resolve in altitude the spectral signature. Limb sounders scan the atmosphere in the vertical, viewing tangentially to the reference spherical surface. Observed radiances are therefore predominantly sensitive to relatively narrow atmospheric layers close to each tangent point, allowing profiles with relatively high vertical resolution to be retrieved. Limitations of the technique are relatively poor horizontal resolution and sampling, and possibly lack of sensitivity to the lower atmosphere, due to obscuration by tropospheric humidity, clouds, aerosols or molecular scattering. The radiation can also be observed with a direct line of sight (LOS) between the source and the detector, which is done with solar, lunar or stellar occultation techniques. The high signal-to-noise ratio allows measurements to be made down to and below the tropopause, with high vertical resolutions. Observations are however limited by geometrical constraints, such that only a few tens of profiles can be measured per day.

A brief review of space-borne passive techniques is given in next Subsec.s.

1.4.4.1 Nadir viewing instruments

The total column of ozone has been continuously measured by the series of Total Ozone Mapping Spectrometer (TOMS) instruments since 1978 [37]. The first instrument capable to provide an estimation of the ozone profile, namely the Backscatter UltraViolet (BUV) instrument, started its measurements in the early 1970s. It was followed by the Solar Backscatter UltraViolet (SBUV, 1978-1984) instrument [38] and by a series of SBUV-2 instruments [39, 40] starting in late 1984 on the operational satellite series of the National Oceanic and Atmospheric Administration (NOAA). This series is now continued as an U. S. national program with SBUV-2 instruments mounted on NOAA's next generation National Polar Orbiting Environmental Satellite System (NPOESS). All these instruments perform the spectral measurement of the solar radiation backscattered by the atmosphere at 12 channels in the UV range, and can obtain height resolved ozone profiles by exploiting the large gradient in O_3 optical depths across the Hartley-Huggins bands. The Global Ozone Monitoring Experiment (GOME) [41], on board the second European Research Satellite (ERS-2) launched by the European Space Agency in 1995, enhanced this technique, providing the continuous spectrum between 240 and 790 nm, i.e. from the UV to the near-infrared (NIR) with relatively-high spectral resolution ($\sim$ 0.2 nm). The wider spectral range of observation allows to obtain information on the ozone distribution coming also from the visible range (Chappuis band) by a Differential Optical Absorption Spectroscopy (DOAS) technique. The GOME instrument has been followed by the GOME-2 instrument carried on the Meteorological Operational (MetOp) satellite series as part of the European polar orbit satellite system [42]. The Scanning Imaging Absorption Spectrometer for Atmospheric Cartography (SCIAMACHY) on ESA's Environmental Satellite (EnviSat) launched in 2002 can be considered as the successor of GOME, providing nadir observations of the solar backscattered radiation from 240 to 2380 nm [43]. In July 2004 the Ozone Monitoring Instrument (OMI) was successfully launched on the Earth Observing System Aura (EOS-Aura) satellite. OMI has similar capabilities for ozone profiling as the GOME and SCIAMACHY instruments, but with a much higher spatial resolution and a daily global coverage [44].

1.4.4.2 Limb viewing instruments

The Limb Radiance Inversion Radiometer (LRIR) and its successor the Limb Infrared Monitor of the Stratosphere (LIMS) instruments performed thermal emission measurements in the millimeter-wave and mid-IR spectral range since 1975 [45]. These instruments can provide both day-time and night-time observations, exploiting the O_3 emission lines for the ozone profile retrieval. The same principle has been used by the three instruments launched in 1991 as payload of the NASA Upper Atmosphere

Research Satellite (UARS), the Cryogenic Limb Array Etalon Spectrometer (CLAES) [46], the Improved Stratospheric And Mesospheric Sounder (ISAMS) [47] and the Microwave Limb Sounder (MLS) [48]. Also the SubMillimeter Radiometer (SMR) on the Swedish experimental satellite Odin [49], launched in 2001, and EnviSat's Michelson Interferometer for Passive Atmospheric Sounding (MIPAS) [50] instrument exploit such a technique to obtain ozone distribution. In the second half of the 1990s the Improved Limb Atmospheric Spectrometer instruments (ILAS-I and ILAS-II) were launched (on ADEOS-I and II, respectively), and performed limb spectral observations of the solar scattered radiation [51]. Unfortunately, both only produced data for a short period due to satellite problems. Other sensors have been conceived to perform limb-observations of the solar scattered radiation in the UV, VIS and NIR range, like the Optical Spectrograph and Infrared Imager System (OSIRIS) [49], also carried on the Odin satellite, and SCIAMACHY on Envisat, see e.g. [52]. An improved version of the MLS, and the HIgh Resolution Dynamics Limb Sounder (HIRDSL), are part of the payload of NASA-Aura platform [53].

1.4.4.3 Occultation viewing instruments

Limb viewing occultation sensors observations started with the Stratospheric Aerosol and Gas Experiment (SAGE) in 1978 and are still operational [54]. Other instruments involve the second and third Polar Ozone and Aerosol Measurement (POAM-II and POAM-III on the French SPOT-3 and SPOT-4 satellites) [55], the Halogen Occultation Experiment (HALOE on UARS, still operational) [56], but also the previously-mentioned ILAS-I, ILAS-II and SCIAMACHY instruments. All these instruments view sun-rise and sun-set over the Earth horizon to measure the directly transmitted solar radiation along the line of sight. This technique has the limitation of providing only about 14 sun-rise and 14 sun-set measurement occasions per day, and in a specific latitude band, which changes with season or in time depending on the satellite orbit. The technique has been recently extended to include lunar (e.g. the SCIAMACHY) and stellar occultation (e.g. the Ultraviolet and Visible Imagers and Spectrographic Imagers (UVISI) [57] and the Global Ozone Monitoring by Occultation of Stars (GOMOS) [58]).

1.4.4.4 Ozone profiles retrieval from nadir UV/VIS satellite data

Ozone profiles can be retrieved from satellite measurements at different geometries and spectral bands. The use of nadir UV/VIS data has the advantage of providing a higher horizontal resolution than limb observations, still containing useful information in the UV/VIS sensible bands. Once the spectra are acquired the most notable problem is the

solution of the inverse problem leading from the *measurement space* to the ozone profile or *state space* (see Chapter 3). Usually this task is performed by means of OE algorithms, i.e. algorithms to invert the *physically-based* forward radiative transfer model. To do this some *a priori* or climatological knowledge is necessary, i.e. the average/climatological ozone profile and covariance matrix. OE algorithms were used for the estimation of ozone profiles from the SBUV, see e.g. [59] and the GOME, see e.g. [60]. An alternative physically-based technique is the Philips-Tikhonov regularization approach, which has been applied to GOME nadir UV/VIS data [61]. An alternative methodology is related to statistical models as the NNs. NNs algorithms were applied to GOME data, see e.g. [62, 63]. In the context of GOME data inversion, these different algorithms and their performances were compared, and results are shown in [64]. Known issues in OE methods regard the sensitivity to systematic/calibration errors and any problem regarding the incomplete formulation of the used forward model, as interactions with clouds and/or aerosols; these problems may be circumvented by the use of NNs.

1.4.4.5 Tropospheric ozone retrieval from nadir UV/VIS satellite data

The retrieval of tropospheric ozone information from space is a particularly difficult task. The problems discussed for the ozone profiles retrieval magnify at lower levels, where a scarce sensitivity is also present. Moreover, a high horizontal resolution is even more important than higher altitude levels, owing to the environmental and air quality implications and short-term space variations involved. A classical approach to this issue is the computation of the TOCs by means of the TOR technique. To separate stratospheric and tropospheric contributions, usually a cloud slicing technique is adopted. Once the tropopause height is determined, the TOC is estimated starting from two measurements, e.g. one nadir instrument operating in the UV measuring the total ozone column content, and one instrument measuring the stratospheric ozone concentrations, e.g. a MW limb sounder as MLS. Examples of this approach are in [65–70]. Another method to retrieve the TOC is the integration of ozone concentrations from OE algorithms over tropospheric altitudes.

1.5 Thesis outline

This thesis is structured in the following way:

- Chapter 2 briefly discuss the SCIAMACHY and OMI missions; data from these sensors have been considered in this thesis work;

- Chapter 3 offers a description of the existing inversion algorithms; first gives an introduction of OE methods and then an overview of the NNs. The two classes of algorithms are put in the same context of the inversion of Earth's spectra to retrieve height resolved atmospheric parameters;

- Chapter 4 presents a new approach to the direct retrieval of tropospheric ozone information from nadir UV/VIS satellite data, with a particular emphasis to the SCIAMACHY nadir states. NNs algorithms are used. The developed algorithm is discussed, as well as design issues and input vector dimensionality reduction by means of an RTM-EP combined algorithm;

- Chapter 5 presents a NNs approach to the retrieval of vertical ozone concentration profile from SCIAMACHY data. As for Chapter 4, design issues are critically discussed. Results are compared to matching retrievals based on the GOME instrument;

- Chapter 6 presents a NNs approach to the retrieval of stratospheric ozone concentration profiles from OMI data. As for Chapter 4, design issues are critically discussed. This part of the work has been performed during a 6 months visit to NASA-GSFC, Greenbel, MD, USA, under the direction of P. K. Bhartia.

- Chapter 3 gives conclusions and future outlook.

- Appendices A and B show further work performed during the PhD period, including the design of a validation activity for NNs algorithms in a GRID environment, and the development of NNs algorithms for the retrieval of additional atmospheric parameters, like temperature profiles and nitrogen dioxide concentrations.

Pasquale Sellitto: sellitto@disp.uniroma2.it

Chapter 2

The SCIAMACHY and the OMI missions

This Chapter introduces two satellite sensors whose data have been used in this work: the EnviSat-SCIAMACHY and the Aura-OMI. A description of these sensors is given in Sec.s (2.1) and (2.2), and some issues regarding operations, calibration and monitoring of their performances are discussed therein.

2.1 The SCanning Imaging Absorption spectroMeter for Atmospheric CHartographY (SCIAMACHY)

2.1.1 The EnviSat Platform

The EnviSat Platform is part of ESA's Earth observation mission [71]. Envisat is an advanced polar-orbiting Earth observation satellite that provides measurements of the atmosphere, ocean, land, and ice by means of its payload composed of 10 instruments. It is intended to give continuity to the ESA ERS missions. With an overall length of more than 25 m, it is the largest satellite ever built by ESA [71]. Fig. (2.1) shows the platform during integration at ESA-ESTEC, with reference to the various sensors in its payload.

Envisat flies in a sun-synchronous polar orbit of about 800 km altitude. The repeat cycle of the reference orbit is 35 days, and for most sensors, being wide swaths, it provides a complete coverage of the globe within one to three days [72]. Some general and orbital parameters are reported in Tab. (2.1).

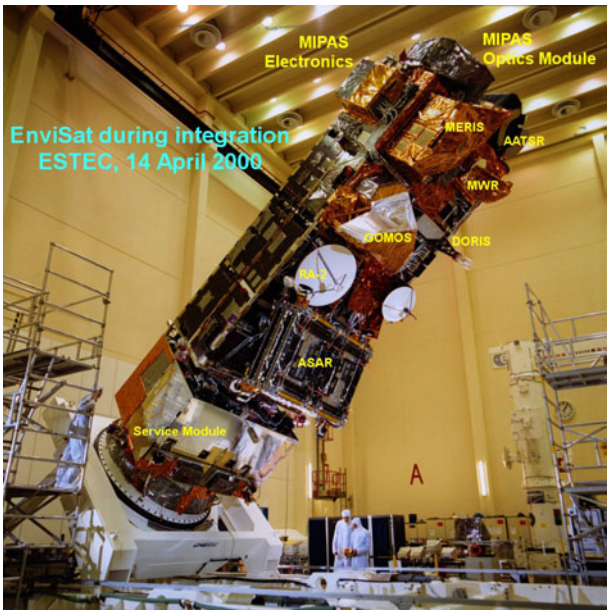

FIGURE 2.1: EnviSat during integration in ESA-ESTEC, the Nederlands. Courtesy of Dutch Space.

General Parameters	
Dimensions	26 m × 10 m × 5 m
Total Mass	8140 kg
Payload Mass	2050 kg
Launcher	Arianne-5
Launch Date	March, 1st, 2002
Orbital parameters	
Inclination	98.55 ± 3
Mean Altitude	799.8 km
Orbital Period	100.6 min
Orbital Type	Polar, sun-synchronous
Orbits per day	14 11/35
Repeat Cycle	35 days (501 orbits)

TABLE 2.1: EnviSat parameters. Adapted from [72].

2.1.2 The instrument

The SCIAMACHY instrument, onboard the ESA-Envisat spacecraft, is a nadir/limb/lunar and solar occultation viewing spectrometer that can operate in the UV/VIS/NIR range (214 to 2386 nm), with a spectral resolution of 0.24-1.48 nm (0.24-0.48 nm in our spectral region of interest) and a nadir spatial resolution of typically 30 km along track × 60 km across track [72–74]. The SCIAMACHY is a passive imaging spectrometer. It is made by the following three elements:

- optical assembly (OA), composed by a mirror system, a telescope and a spectrometer;

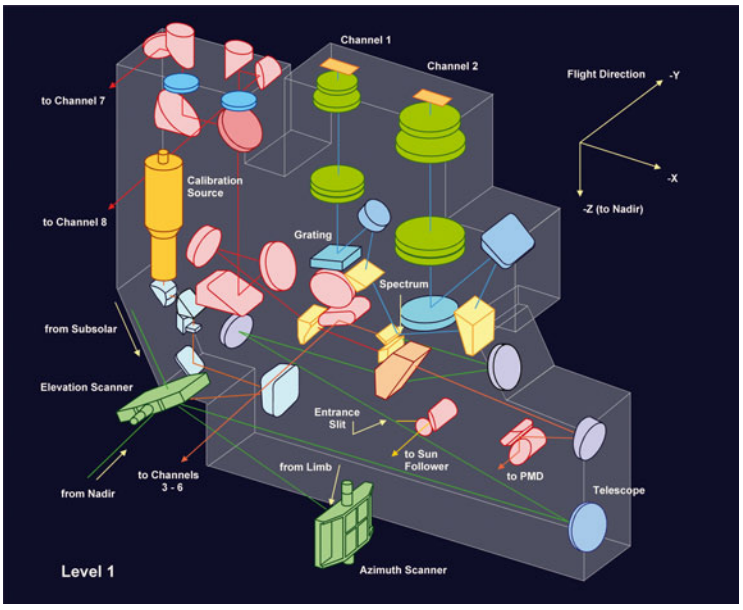

FIGURE 2.2: Sciamachy level 1 OA. Courtesy of DLR-IMF.

- thermal subsystem;
- electronic subsystems.

The OA is the part of the instrument that collects light and produces the spectral information. For maintaining the specified thermal conditions, the OA includes a radiator and the so-called Thermal Bus Unit (TBU). The OA is organized into two levels; Fig.s (2.2) and (2.3) depict these two parts of the OA. Entrance optics, pre-disperser prism, calibration unit and channels 1 and 2 are contained in level 1 OA facing in the flight direction. Channels 3-8 are located in level 2 OA. By combining the optical components various optical paths or *trains* from external and internal light sources to detectors can be established, so identifying the various observation modes of the instrument (cfr Fig. (2.4)). During nominal measurements light enters the instrument via the Azimuth (ASM) or Elevation Scan Mechanisms (ESM). Whilst the ASM captures radiation coming from regions ahead of the spacecraft, the ESM either views the ASM or the region directly underneath the spacecraft. In the first case (limb observation), the light collected from the ASM is reflected into the spectrometer, in the second case (nadir observation) the ASM is not involved in the optical path. The scanning interval of the two scanning mechanisms is limited by baffles; the effective or Total Clear Field of View (TCFoV) is then the one discussed in Sec. (2.1.3) for the different observation modes. The scanner control tasks are programmed in on-board software with supporting information being generated by the Sun Follower (SF) in the case of solar and lunar observations. The solar irradiance has to be measured via a diffuser. Two aluminium

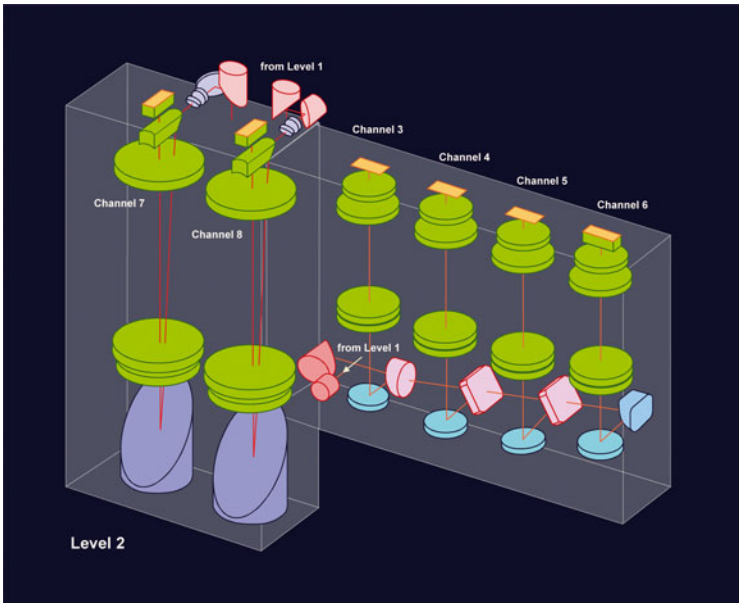

FIGURE 2.3: Sciamachy level 2 OA. Courtesy of DLR-IMF.

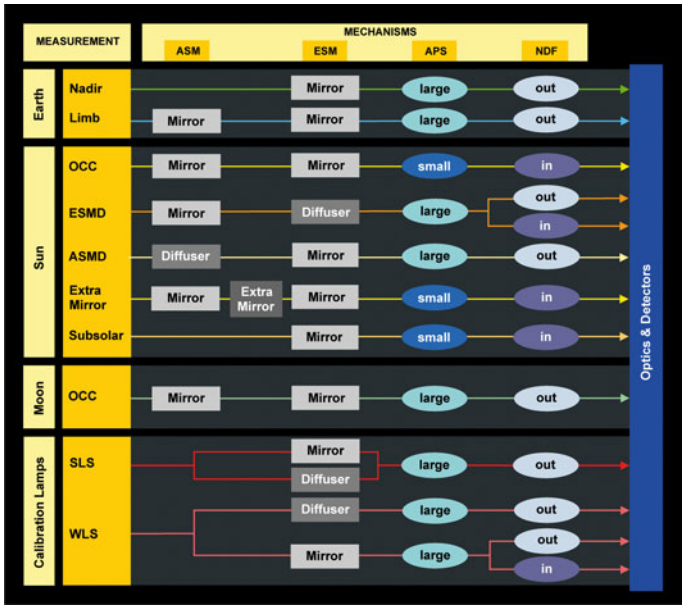

FIGURE 2.4: Sciamachy observation modes and related optical paths or *trains*. Courtesy of DLR-IMF.

Channel	Spectral Range (nm)	Resolution (nm)	Stability (nm)
1	214-334	0.24	0.003
2	300-412	0.26	0.003
3	383-628	0.44	0.004
4	595-812	0.48	0.005
5	773-1063	0.54	0.005
6	971-1773	1.48	0.015
7	1934-2044	0.22	0.003
8	2259-2386	0.26	0.003

TABLE 2.2: SCIAMACHY science channels. Adapted from [72]

diffusers are mounted on the SCIAMACHY: one on the backside of the ESM mirror, one on the backside of the ASM mirror.

The ESM reflects light towards the telescope mirror, which has a diameter of 32 mm. From the telescope mirror the light path continues to the spectrometer entrance slit. The overall spectrometer design is based on a two stage dispersion concept: first, the incoming light is pre-dispersed and projected onto a spectral image. Subsequently, this spectral image is dissected into eight spectral intervals that are diverted into eight spectral channels for further dispersion. The selected approach has the advantage of reducing stray light in the channels with average low light intensity (e.g., UV and NIR-SWIR). The pre-disperser prism, located behind the entrance slit, is used for two purposes: it weakly disperses the light and directs fully polarized light for further processing to the Polarization Measurement Device (PMD). Small pick-off prisms and subsequent dichroic mirrors direct the intermediate spectrum to the 8 science channels where the light is further dispersed by individual gratings. In the light path routed to channels 3-6 the Neutral Density Filter Mechanism (NDFM) can move a filter into the beam. With a filter transmission of 25% it can be used to reduce light levels during solar measurements.

The full resolution spectral information is generated in 8 science channels (see Tab. (2.2)). These employ two types of detectors. For the UV-VIS-NIR range covered by channels 1-5, standard Silicon photodiodes (RL 1024 SR, EG&G RETICON, California) with 1024 pixels are used which are sequentially read out. Additionally, UV channels 1 and 2 are electronically divided into two virtual bands 1a/1b and 2a/2b, which can be configured separately. The SWIR channels 6-8 employ Indium Gallium Arsenide detectors (InGaAs by EPITAXX, New Jersey) specifically developed and qualified for SCIAMACHY.

For channels 1-5, the detector pixels are read out sequentially with a time delay between the first and the last pixel of about 28.75 msec. Therefore pixels that are read out at a different time see a somewhat different ground scene because during the sequential readout the platform and the scan mirrors continue to move. The size of the wavelength

dependent spectral bias depends on the variability of the ground scene. Nominally, the minimum Pixel Exposure Time (PET) amounts to 31.25 ms. Trace gas features are distributed non-uniformly over the spectrum. The limited total data rate would therefore prohibit the detailed sampling of those ranges of interest if the full spectrum had to be downlinked as one block. SCIAMACHY avoids this situation by using spectral clusters and co-adding. The 1024 pixels per channel can be sub-divided into a number of *clusters* identifying regions where trace gas retrieval will take place. Each cluster can be sampled by on-board data processing applying *co-adding* factors f_{coadd} to the readout of the pixels of this cluster. This results in an Integration Time (IT):

$$IT = t_{PET} \cdot f_{coadd} \tag{2.1}$$

which defines how many subsequent readouts of each pixel of a cluster are added to generate one measurement data readout. By appropriately setting the integration time, high or low temporal resolution, equivalent to high or low spatial resolution, can be selected. Thus, depending on the executed measurement states, variable ground pixel sizes as a function of spectral region, i.e. trace gas features, are achieved. Overall the detector performance is characterized by low noise and high instrument throughput. This allows measuring the incoming light with the required very high signal-to-noise ratio [74].

The requirements to maintain high spectral stability and relative radiometric accuracy over the mission's lifetime is verified via an on-board calibration unit. It consists of two calibration lamps, one for white light and one for spectral lines. The White Light Source (WLS) is a 5 Watt UV-optimized Tungsten-Halogen lamp with an equivalent blackbody temperature of about 3000 K. Its signal is used to verify the pixel-to-pixel signal stability. The Spectral Line Source (SLS) is a Neon filled hollow Pt/Cr cathode lamp. Its operation allows the determination of the pixel-to-wavelength relation. The calibration unit is located close to the ESM. By rotating the ESM mirror into specific positions it is possible to reflect light from the WLS respectively the SLS towards the telescope mirror and thus onto the entrance slit.

The measurement sensitivity of the spectrometer depends on the polarization state of the incoming light. Therefore SCIAMACHY is equipped with a PMD. Six of its channels (PMD A-F) measure light polarized perpendicular to the SCIAMACHY optical plane, generated by a Brewster angle reflection at the second face of the pre-dispersing prism. This polarized beam is split into six different spectral bands. The spectral bands are quite broad and overlap with spectral regions of channels 2, 3, 4, 5, 6, and 8.

The Optical Bench Module (OBM) needs to be operated in orbit at a constant temperature to preserve validity and accuracy of the on-ground calibration and characterization.

Additionally, a low temperature level is required to keep the thermal radiation of the instrument itself at a minimum in order not to enhance the background in the SWIR channels 7 and 8. Therefore a dedicated radiator, RAD A, is used to cool the OBM and the detector module electronics to between -17.6 and -18.2 °C. While the RAD A provides cooling capacity, thermal stability of the OBM needs to be established via a closed loop Active Thermal Control (ATC) system. In-orbit operating temperatures of the detectors lie well below ambient. The detectors are cooled via the Radiant Reflector Unit (RRU) of the Radiant Cooler Assembly (RCA). SCIAMACHY's Radiant Cooler (RC) dissipates heat generated in the detector modules to deep space to permit cooling of the detector arrays to in-orbit operating temperatures. The reflecting unit and the detectors are connected via the TBU of the OA.

SCIAMACHY's *brain* resides in the Electronic Assembly (EA). It provides the processing and formatting link of the detectors generating the primary science data with the spacecraft platform transmitting the digitized science data to ground. In addition, the EA contains all electrical functions required for autonomous operation of the whole instrument. The EA consists of the primary processor called Instrument Control Unit (ICU) and the secondary processors, the Power Mechanism and Thermal Control (PMTC) and the Science Data Processing Unit (SDPU).

2.1.3 Operations

Scientific requirements of the SCIAMACHY include viewing geometries for atmospheric measurements of nadir, limb, sun occultation and moon occultation [73, 74]. In addition, external (e.g. dark current, sun reference) and internal (calibration lamps) observations supplement the measurement schedule. Fig. (2.5) reports a schematics of the science measurement modes of the SCIAMACHY. In Fig. (2.6) the TCFoV of the instrument, with reference to the different measurement modes and in connection to the baffle limitations to ASM and ESM rotation angles, is depicted.

The succession and type of measurements for each orbit is determined to fulfill the mission objectives. The general schedule for nominal operations must take into account the following *orbital mission scenario*:

- swath width of ± 480 km relative to ground track in nadir and limb scans for global coverage within 6 days (taking into account the alternating limb/nadir measurements);
- matching limb/nadir measurements in the illuminated part of the orbit;
- sun occultation measurements each orbit;

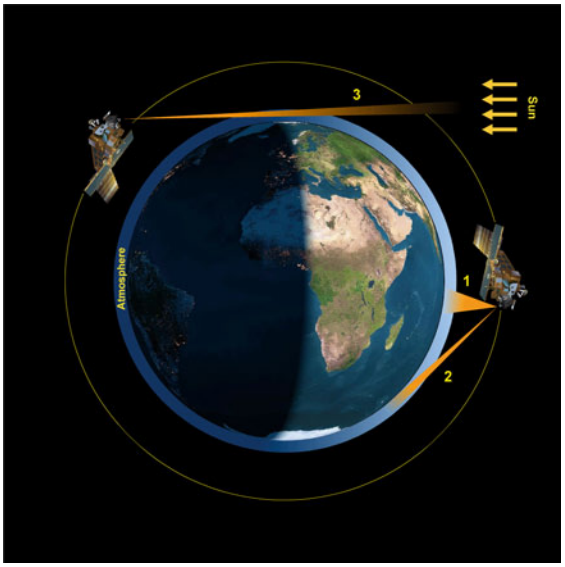

FIGURE 2.5: SCIAMACHY's science observation modes. 1 = nadir, 2 = limb, 3 = occultation. Courtesy of DLR-IMF.

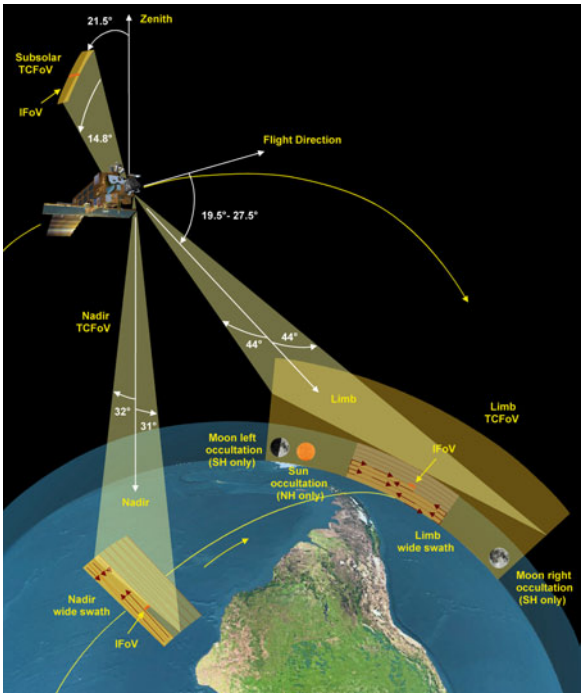

FIGURE 2.6: SCIAMACHY's Total Clear Fields of View (TCFoV) and observation geometries. Courtesy of DLR-IMF.

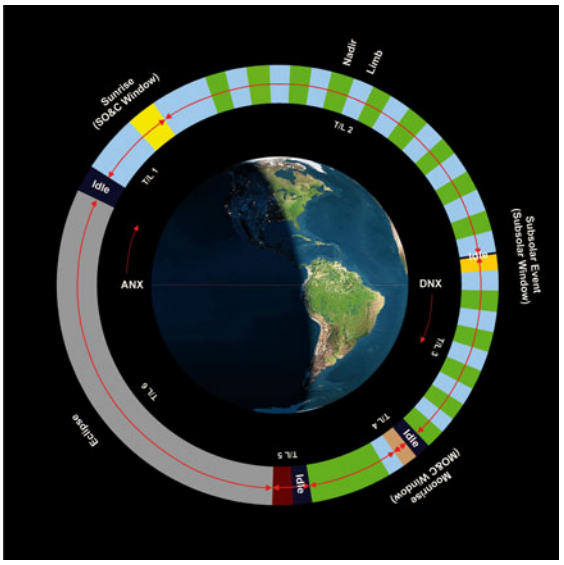

FIGURE 2.7: SCIAMACHY reference orbit with timelines. Courtesy of DLR-IMF.

- moon occultation measurements whenever possible (moonrise on nightside of Earth);
- calibration and monitoring measurements on a daily (every 14^{th} orbit), weekly (every 98^{th} orbit) and monthly basis.

A general depiction of the periodicity of measurements for an ideal orbit is given in Fig. (2.7). The alternative nadir and limb measurements can be identified in the illuminated section of the orbit while occultation measurements (SO, for Solar Occultation and MO, for Moon Occultation) occur at the sun- moon-rise.

The individual functions to operate SCIAMACHY in measurement modes are defined as *states*. A state is a sequence of activities for a particular measurement task, e.g. nadir observations with certain pixel exposure times, sun occultation with certain scan geometry, etc. In total 70 states can be defined on-board and are associated to a *state ID*, e.g. nadir states are identified by the state ID 1-7 (960 km swath) and 9-15 (120 km swath). Different nadir states exist because of different illuminations along the orbit and subsequent different PETs.

We will now give a brief overview of the nadir states, owing to the interest for this thesis work. For a nadir state, the instrument Instantaneous Line of Sight (ILoS) is pointed, via the ESM, to the sub-satellite point. Starting left of the flight direction, the ESM is then moved for 4 sec across track to the right with an angular rate yielding the required swath width on the ground. Having reached the turnaround on the right side, the ESM returns in 1 sec across track back to the left side. For each integration time, a channel dependent readout of the spectrum occurs. Depending on the measurement duration of the nadir state, a series of forward/backward scans cover a ground scene of typically 400

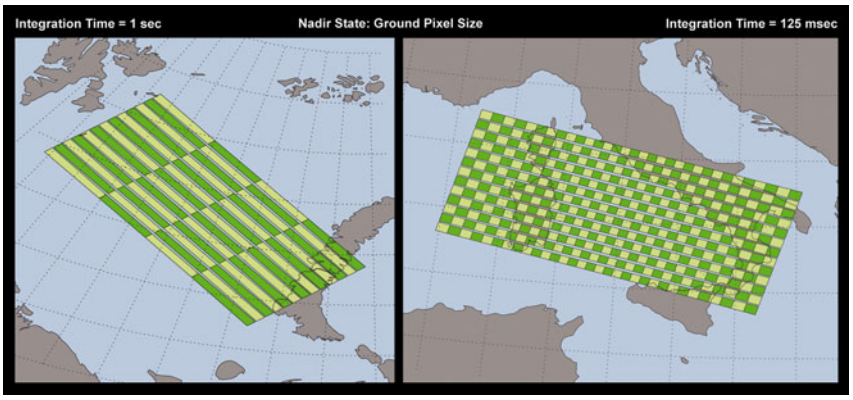

FIGURE 2.8: Ground pixels for a nadir measurement (only forward scan); integration time = 1 sec (left), integration time = 0.125 (right). Courtesy of DLR-IMF.

km along track. Within the ground scene, individual ground pixels have a size which is defined by the selected IT. They vary from about 26 km × 30 km (along-track × across-track) up to 32 km × 930 km for wide swath settings. So, across-track extent is defined by the IT while along-track's size reflects the dimension of the IFoV with only a small contribution of the integration time. As an example, in Fig. (2.8) we show two arrays of ground pixels for a nadir state, one for a IT = 1 sec and the other for a IT = 125 msec.

2.1.4 Calibration and Monitoring

The goal of calibration is to convert detectors signals, in Binary Units (BU) ranging from 0 to 65535, being the signal of the detector a 16 bit quantity, into physical quantities, e.g. W/(m^2 nm). The general calibration equation [75] for any spectrometer is:

$$S_{det} = I(\lambda) \cdot \Gamma_{inst}(\lambda) \cdot QE(T_{det}, \lambda) + S_{stray} + DC + S_{elec} \tag{2.2}$$

where S_{det} is the signal as it is measured by the detector, I the incoming radiation intensity, $\Gamma_{inst}(\lambda)$ the total transmission of the instrument, which can also be dependent on the polarization of the incoming light, QE the detector temperature dependent quantum efficiency, S_{stray} the stray light, DC the dark signal and S_{elec} electronic effects such as non-linearities.

Let's now briefly analyze the individual calibration steps in the order they're actually performed for the SCIAMACHY. Fig. (2.9) summarizes these steps. Red boxes are related to in-flight calibration measurements, green boxes refer to on-ground measurements performed under thermal vacuum and blue boxes to ambient on-ground tests.

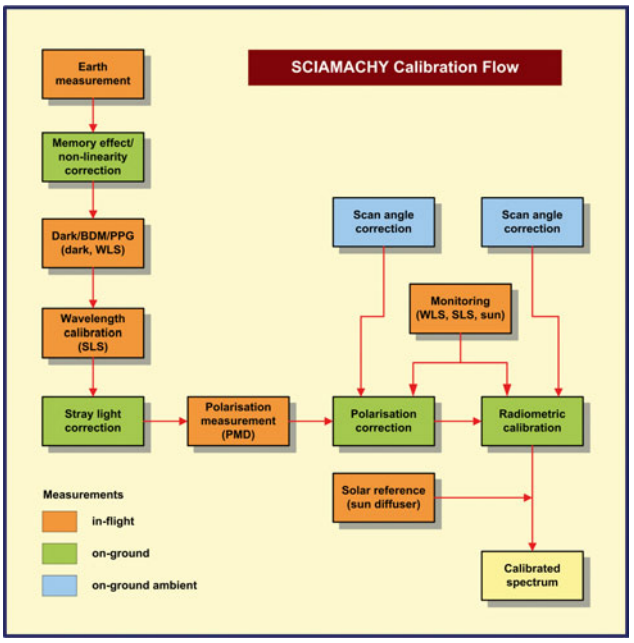

FIGURE 2.9: SCIAMACHY data calibration concept. Courtesy of SRON.

The first step is the correction for errors due to the electronics of detectors and the detectors themselves, i.e. DC and S_{elec} in Eq. (2.2). This part of the calibration of the measurements are generally handled separately for SCIAMACHY channels 1-5 (UV/VIS/NIR) and channels 6-8 (SWIR) because of their different detectors materials and readout electronics. Here only a brief description of UV/VIS/NIR calibration issues is given. The first systematic error to correct is the so-called *memory effect*: signals deviate from a linear response depending on the *previous* readout. This effect has been found more significant for detector fillings (i.e., the previous readout) of about 19000 to 21000 BU. A typical trend of the error vs the detector filling is given in Fig. (2.10) for channel 3. Another systematic error that is related to the detectors is the DC effect: ideally the instrument gives a readout not equal to 0 even with no incoming light. The DC is made of two components, the Analogue Offset (AO), independent of time and only added to the measurement to avoid negative readouts, and the Leakage Current (LC), caused by thermally created electron-hole pairs. The DC component is measured every orbit and take the following form:

$$DC_{ch\,1-5} = f_{coadd} \cdot AO + f_{coadd} \cdot PET \cdot LC \tag{2.3}$$

The subsequent correction is the *wavelength calibration*, i.e. to assign a wavelength to each individual SCIAMACHY detector pixel during the flight. In-flight spectral calibration of SCIAMACHY data uses the internal SLS measurements with the exception of channels 7 and 8. The procedure takes into account selected lines whose pixel position

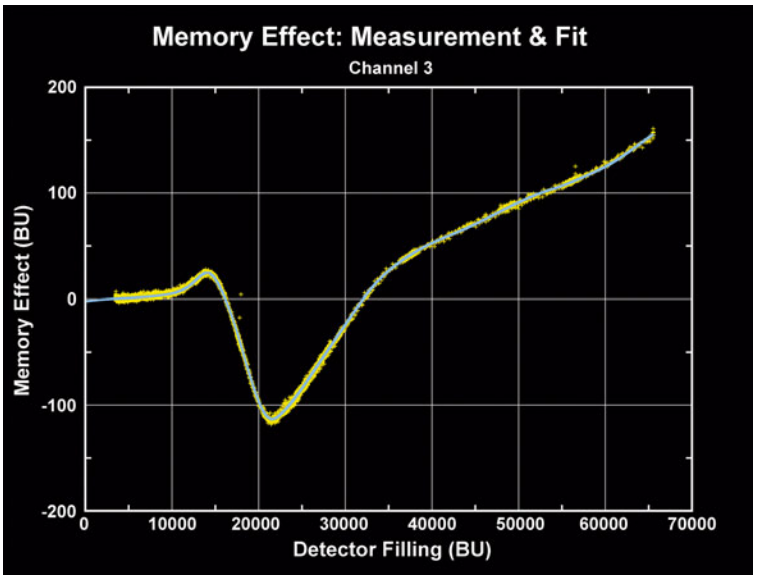

FIGURE 2.10: Memory effect for SCIAMACHY's channel 3. Courtesy of SRON.

is determined analytically and then fitted to theoretical line position provided with the calibration data. A check of the quality of this calibration is given by measurements of solar Fraunhofer lines.

Then the stray light (S_{stray} in Eq. 2.2) is taken into account. There exist two types of stray light, the spectral and the spatial stray light. Spectral stray light is light of a certain wavelength which is scattered to a detector pixel belonging to a different wavelength. It can lead to distortions in the shape of the spectrum. This type of stray light is usually caused by a reflection in the instrument after the dispersion of the light beam. Spatial stray light is light entering the telescope from outside the IFoV. It is dispersed just like light from the observation target. Depending on its sources, the spatial stray light component can add an additional offset to the spectrum and/or distort the spectrum, if the primary source of the stray light has spectral characteristics that differ significantly from the observed target. Stray light was characterized on-ground and then the data acquired are used to correct the in-flight effect. It can be noticed that for channel 1 the spectral stray light can be remarkable, reaching levels up to 10% of the incoming signal and being highly dependent on wavelength. Spatial stray light is mainly important for limb measurements and will not be considered here.

Polarization issue is also important for the correct interpretation of SCIAMACHY's readout. SCIAMACHY is sensitive to polarization because of the lack of a polarization scrambler (on the contrary, the OMI has a polarization scrambler, see Sec. (2.2.3)); so the response will not depend only on the intensity of the incoming light but also on its polarization. The polarization correction is achieved with the Mueller matrix ($\mathcal{M}$) approach. The general formulation of this problem can be reduced at the following:

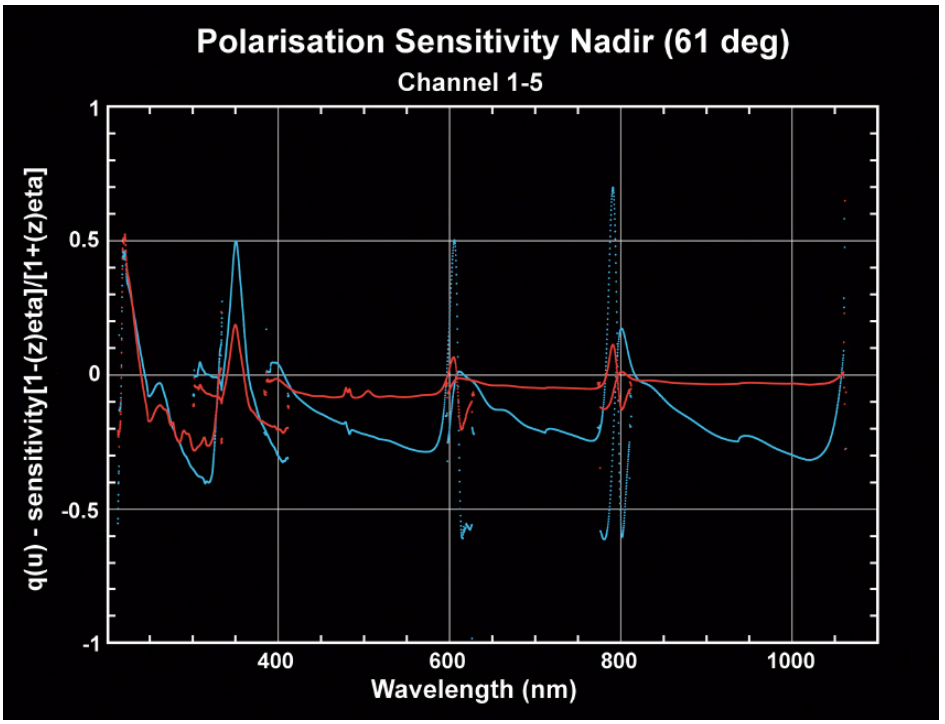

FIGURE 2.11: Q (blue) and u (red) polarization sensitivities for channel 1-5 nadir measurements (elavation angle of 61°). Courtesy of SRON.

$$S_{\text{det}} = M_{11}^{\text{D,P}} \cdot I \cdot \left(1 + \frac{M_{12}^{\text{D,P}}}{M_{11}^{\text{D,P}}} \cdot q + \frac{M_{13}^{\text{D,P}}}{M_{11}^{\text{D,P}}} \cdot u\right) \tag{2.4}$$

where D and P indicate Detector and Polarization Measurement Device, respectively, the three elements of the Mueller matrix, i.e. the first row in $\mathcal{M}$, are the radiometric sensitivity (M_{11}) and the polarization sensitivity (M_{12} and M_{13}) of the SCIAMACHY, q and u are measures of polarization along the x or y axis, and along the 45° direction, normalized to the total intensity. The term in brackets is the inverse of the polarization correction factor c_{pol}. So, the problem of the correction for polarization effects can be solved by the knowledge of the polarization sensitivity of the instrument (on-ground) and the state of polarization of the incoming light for specific measurement (in-flight). Fig. (2.11) shows the two polarization sensitivities $M_{12}^{D,P}/M_{11}^{D,P}$ and $M_{13}^{D,P}/M_{11}^{D,P}$ (referred as [1-z]/[1+z] and [1-eta]/[1+eta] in the axis text). The second step is achieved by measuring the ratio in the PMD channels and the science channel for each individual measurement.

The final step is the radiometric calibration. The retrieval of trace gases usually uses quantities proportional to the reflectance, e.g. the ratio of Earth radiance and solar irradiance. The solar irradiance is measured in-flight with on-board diffusers. From

equation 2.4 and the analogous for solar irradiance we obtain, for a nadir measurement:

$$R = \frac{\pi \cdot I_{\text{Earth}}}{\mu_0 \cdot I_{\text{sun}}} = \frac{\pi}{\mu_0} \cdot \frac{S_{\text{det}}^{\text{Earth}}}{S_{\text{det}}^{\text{sun}}} \cdot \frac{M_{11}^{\text{sun}}}{M_{11}^{\text{N}}} \cdot c_{\text{pol}} \tag{2.5}$$

with Is and Ss the Earth and sun intensities and measured signals, μ_0 the cosine of the solar zenith angle, M_{11}^{N} the radiometric response for nadir measurements and M_{11}^{sun} the radiometric responses for sun diffuser measurements. Superscript D was left out for simplicity because all quantities in equation 2.5 relates to the detectors. The wavelength and incidence angle dependent radiometric calibration parameters $M_{11}^{\text{N}}(\lambda, \alpha)$ and $M_{11}^{\text{sun}}(\lambda, \alpha)$ are determined on-ground.

The on-ground calibration activity is followed by a steady in-flight monitoring of the instrument performances in order to correct for degradation effects through the instrument lifetime [76]. It is carried out through regular trend analyses to measurement data obtained with the internal WLS and of observations of the unobscured sun above the atmosphere. Different light paths are considered, allowing the monitoring of the performances of individual optical components. At the moment, long-term monitoring results show that even after reaching its nominal life time of five years the SCIAMACHY instrument is still in good shape, although in the UV an increasing degradation is clear, which depends on wavelength, especially close to the channel edges and in channel 2. By considering the application of degradation correction factors, the SCIAMACHY can extend its mission lifetime up to 2010.

2.2 The Ozone Monitoring Instrument (OMI)

2.2.1 The EOS-Aura Platform

NASA's Earth Observing System (EOS) programme, introduced in the late '80s, is composed of three main platforms, namely Terra, Aqua and Aura, and several smaller platforms as the IceSat, the Ocean Surface Topography Mission and others. The EOS programme aims at a coordinated series of polar-orbiting and low inclination satellites for long-term global observations of the land surface, biosphere, solid Earth, atmosphere and oceans [77].

Aura, Latin for *breeze*, is a polar-orbiting satellite launched on July 15, 2004, and its payload is composed of 4 instruments for the observation of the Earth's atmosphere. Fig. (2.12) shows the platform during integration and a representation of the 4 sensors.

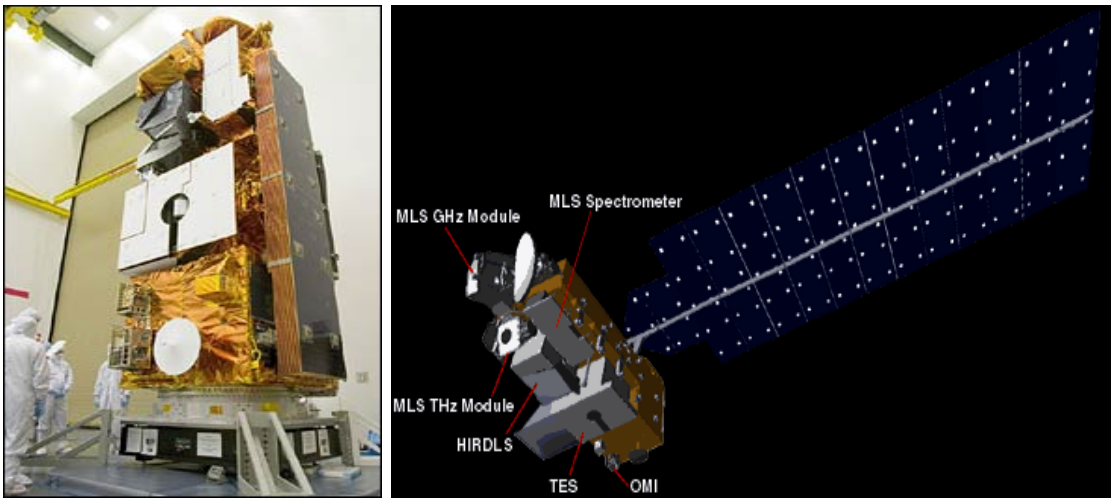

(a) Integration of Aura. Courtesy of BBC.

(b) A scheme of Aura with the four sensors. Courtesy of Dutch Space.

FIGURE 2.12: Aura during integration and a scheme of the platform with its four instruments.

General Parameters	
Structure Weight	700 kg
Launcher	Delta II 7920-10L
Launch Date	March, July 15th, 2004
Orbital parameters	
Inclination	$\sim$ 98.00
Mean Altitude	705.0 km
Orbital Period	$\sim$ 100.0 min
Orbital Type	Polar, sun-synchronous
Repeat Cycle	16 days
Equator Crossing Time	1:45 PM $\pm$ 15 minute

TABLE 2.3: Aura parameters. Adapted from [77].

Aura flies in a sun-synchronous orbit of about 700 km altitude. The repeat cycle of the reference orbit is 16 days. Some general and orbital parameters are reported in Tab. (2.3).

2.2.2 The A-Train

Aura flies in formation about 15 min behind Aqua. The Cloud-Aerosol Lidar and Infrared Pathfinder Satellite Observation (CALIPSO) [36] and CloudSat [78] are less than a minute behind Aqua. These satellites, the CNES Polarization & Anisotropy of Reflectances for Atmospheric Sciences coupled with Observations from a Lidar (PARASOL) [35] and ESSP Orbiting Carbon Observatory (OCO) [79] are usually referred as

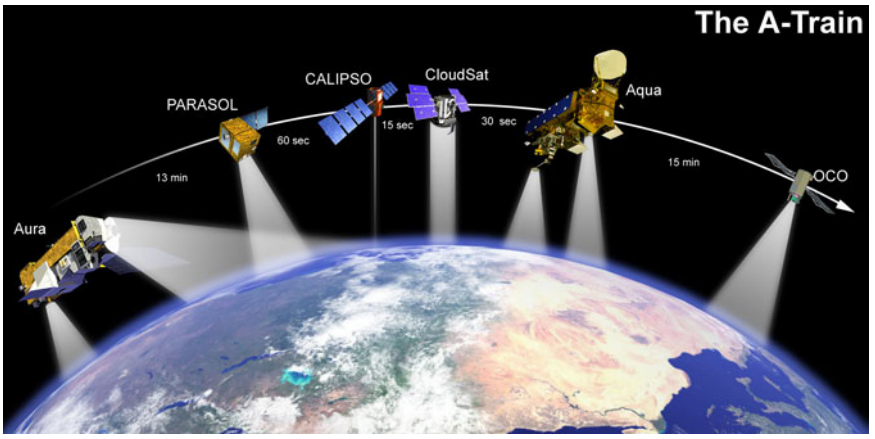

FIGURE 2.13: The A-Train. Figure taken from [80].

the *A-Train* (see Fig. (2.13)) [80]; it can be thought as an extended instrument package focusing on climate change. Flying in such a formation increases the number of, validates, and enables coordination between observations, resulting in a more complete *virtual science platform*.

2.2.3 The Instrument

The OMI, a contribution of the Netherlands and Finland to the NASA's Aura mission, flies on the Aura spacecraft. The OMI is a nadir-viewing spectrometer that can operate in the UV/VIS range (270 to 500 nm), with a spectral resolution of 0.42-0.63 nm and a nadir spatial resolution of typically 13 km along track $\times$ 24 km across track [44]. The 114° viewing angle of the telescope corresponds to a 2600 km wide swath on the surface, which enables measurements with a daily global coverage. The light entering the telescope is depolarized using a scrambler and then split into two channels: the UV channel (wavelength range 270 - 380 nm) and the VIS channel (wavelength range 350 - 500 nm). The OMI is a heritage instrument of the European GOME and SCIAMACHY instruments, which introduced the concept of measuring the complete spectrum in the UV/VIS/NIR wavelength range with a high spectral resolution. The high spatial and spectral resolutions are simultaneously possible by using a two-dimensional detector. The small pixel size enables OMI to look in between the clouds, which is very important for retrieving tropospheric information.

The OMI instrument is composed of the following three elements (cfr figure 2.14 [81]):

- Optical Assembly (OA), consisting of the OPtical Bench (OPB), two DEtector Modules (DEM), and thermal hardware;

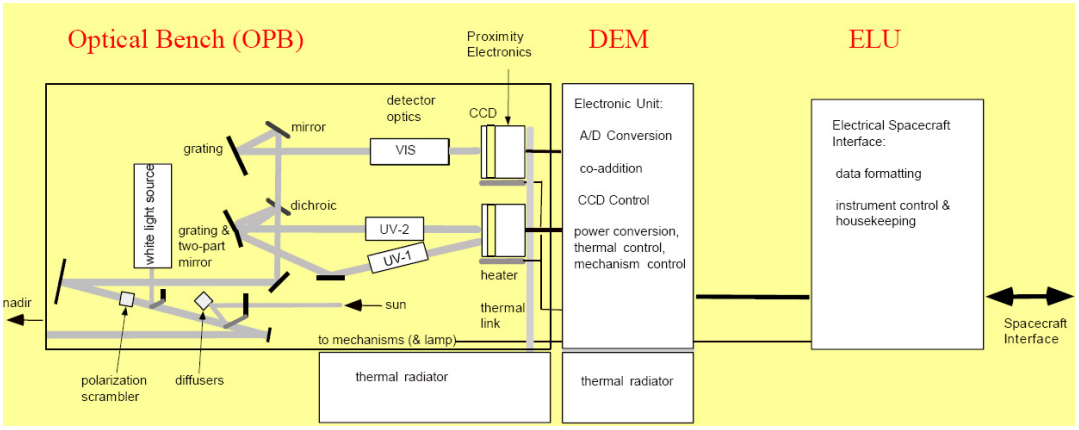

FIGURE 2.14: Conceptual design of the Ozone Monitoring Instrument. Courtesy of Fokker Space.

Ch.	Total Range (nm)	Full Perf. Range (nm)	Av. Res. (nm)	Av. Sampling Dist. (nm/pixel)
UV-1	270-314	270-310	0.42	0.32
UV-2	306-380	310-365	0.45	0.15
VIS	350-500	365-500	0.63	0.21

TABLE 2.4: OMI science channels. Adapted from [44].

- ELectronics Unit (ELU), performing CCD readout control and analogue-to-digital conversion;
- Interface Adaptor Module (IAM), performing command buffering as well as the data formatting and Satellite Bus Interface (SBI) functions.

In the OA, the radiance and irradiance is collected and then split according to wavelength and focussed on the detector modules of the two channels. The OPB consists of a single aluminium structure in which all elements are mounted. Attached to this aluminium structure are the two DEM. The OA thermal hardware consists of a thermal radiator and heaters. The radiator is thermally connected to the DEM. The heaters are attached to the OPB structure and the CCD detectors.

The OPB consists of a telescope, UV channel, VIS channel and calibration sub-systems. To switch between Earth observations and the different calibration modes, the OPB uses three mechanisms. In Fig. (2.15) and (2.16) the optical layout of the telescope, UV-1 and UV-2, and VIS channel, respectively, and the calibration optics are shown. Note that the plane of Fig. (2.16) is perpendicular to that of Fig. (2.15). OMI science channels definition and main characteristics are given in Tab. (2.4).

The telescope is a wide field reflective telecentric configuration. The telescope consists of two spherical mirrors (003 and 007, with reference to the mentioned Fig.s). Radiation from the Earth is imaged on the entrance slit (008) of the spectrometer. Between the

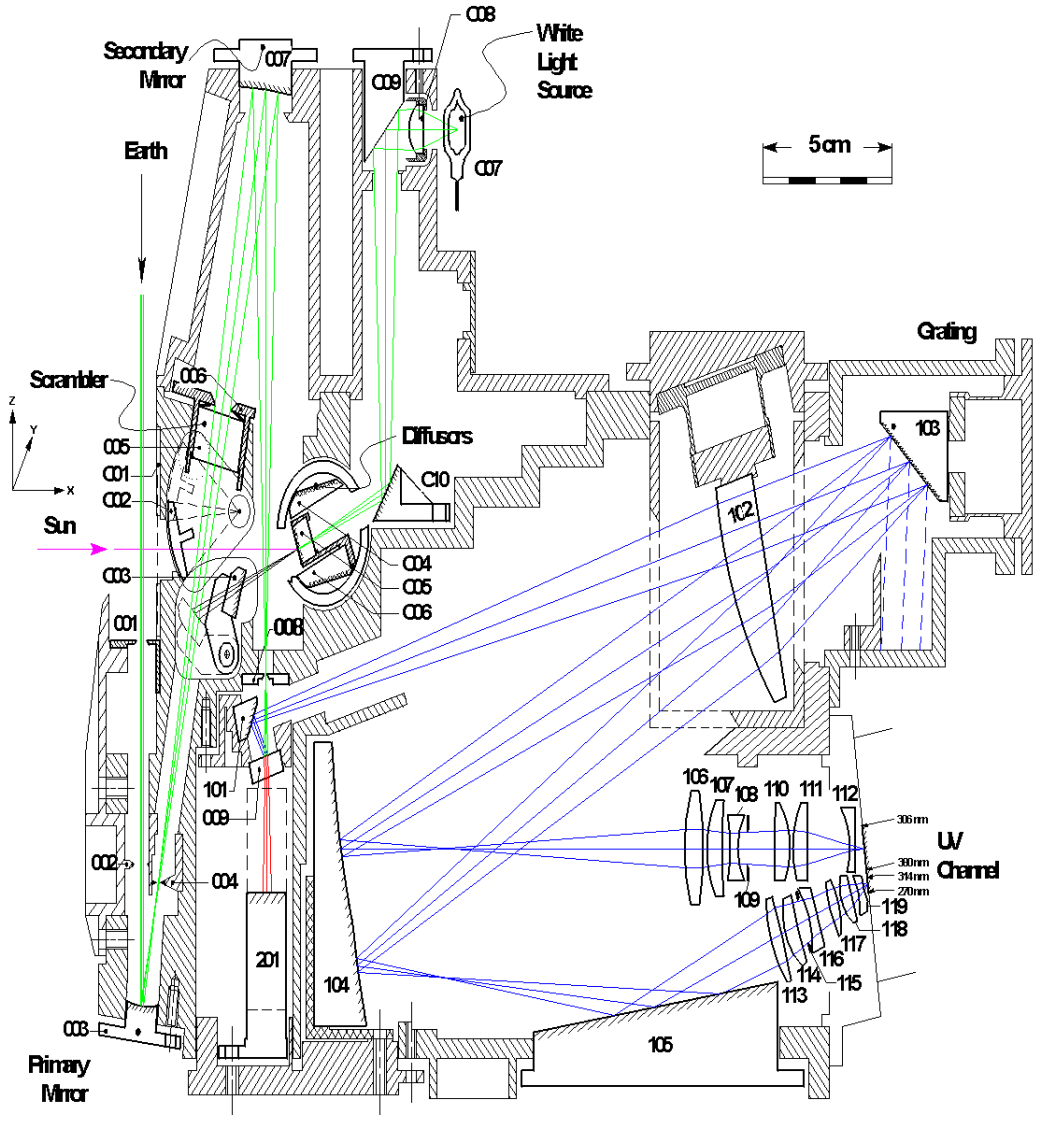

FIGURE 2.15: OMI UV OA. Courtesy of KNMI.

primary and secondary mirror a polarization scrambler (005) is positioned close to the aperture stop (006) of the telescope. The FOV is in the plane perpendicular to the plane of drawing. The secondary mirror has a coating to suppress stray light from 500 nm up towards longer wavelengths.

The OMI spectrometer is sensitive to the polarization of the incoming radiation (due to polarization dependent properties of mirrors, dichroics and gratings). Therefore, Earth radiances with exactly the same intensity but a different polarization will give a different detector signals. The purpose of the polarization scrambler is to make the instrument insensitive to the polarization of the received radiation. In principle a scrambler transforms one polarization state into a continuum of polarization states and thus not into

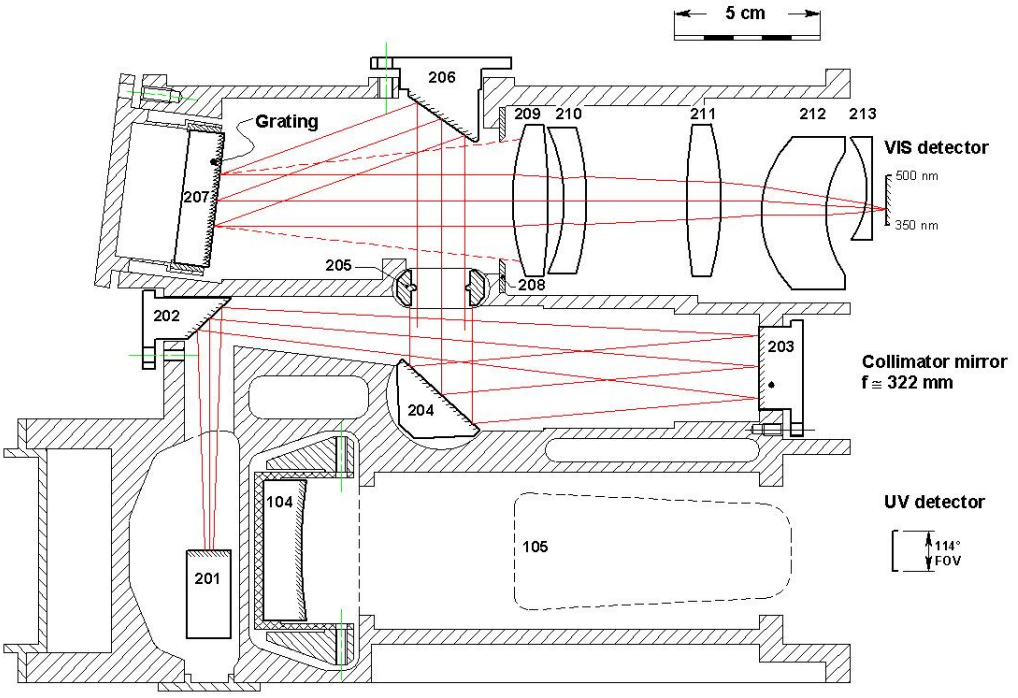

FIGURE 2.16: OMI VIS OA. Courtesy of KNMI.

totally unpolarized light. Therefore a scrambler is called a pseudo-depolarizer. For OMI a spatial pseudo-polarizer is applied, which transforms the input into an output of which the polarization state varies with position over the scrambler exit aperture. Polarization effects due to the primary mirror are compensated for by the first scrambler surface.

Behind the entrance slit, a dichroic mirror (009) reflects the spectral range of the UV channels to folding mirror (101) and transmits the VIS spectral range to a flat mirror (201), that reflects the light 90° out the plane of drawing. The UV radiation is reflected by mirror (101) to a plano convex fused silica lens (102), that collimates the beam from the entrance slit in the direction of the grating (103). The function of the collimating/imaging lens (102) is twofold: it creates a parallel incoming beam on the grating (103) and forms an intermediate spectrum of the diffracted beams close to the field mirror (104). The grating (103) is used in the first order. The layout of the UV channel is determined to a large extent by the stray light requirements especially for the UV-1 spectral area (270 - 310 nm). Within the UV spectral range the variation in radiance from the Earth between the shortest wavelength ($\lambda < 290$ nm) and the longer wavelength ($\lambda > 320$ nm) varies by more than three orders of magnitude. Without proper action the stray light at wavelengths below 290 nm can exceed the signal itself. This stray light originates from wavelengths between 310 to 380 nm. To avoid this unwanted situation, the UV channel is split into to sub-channels: UV-1 and UV-2. An intermediate UV spectrum is created, close to a field mirror (104). This field mirror is supplied with a coating with a wavelength dependent variable reflection in order to

suppress the stray light of larger wavelengths in the extreme UV. Depending on the bandwidth of reflection coating, a suppression of stray light of one order of magnitude is reached. Moreover by splitting the spectral range in two parts, the stray light that is caused by internal reflections in the UV-2 imaging objective, has no effect on the UV-1 spectrum at the detector surface. The UV-1 image is scaled down by a factor of 2 on the CCD compared to the UV-2 image, in order to improve the signal to noise performance of the UV-1 channel by a factor of 2, at the cost of doubling the ground pixel size in the swath direction.

The VIS part of the spectrum (350 - 500 nm) is reflected by mirror (201) via folding mirror (202) to a collimating mirror (203). The rest of the visible channel is rather straight forward and consists of 2 folding mirrors (204 and 206), a plane grating with 1350 gr/mm (207) and an objective (209 - 213) to image the diffracted beams on the second detector.

The main function of the DEM is to convert the optical signal provided by the OPB, to an analogue electrical signal. The OMI system includes two identical DEMs. Each DEM consists of a CCD, control electronics and thermal hardware. The OMI detectors are so-called *frame transfer* CCDs. This means that the CCDs have three sections: an image section, a storage section, and a readout register. The pixels are 22.5 $\times$ 22.5 μm in size and there are no regions in between the pixels that are not sensitive to light, which is important for accurately detecting spectral features of trace gases. Each image part of the CCD consists of 580 $\times$ 780 CCD pixels, of which 480 $\times$ 750 are used for the Earth measurements. The wavelength information is distributed along a CCD row, the spatial information is distributed along a CCD column.

The control electronics have the functionality of sequencing electronics for decoding the control signals to CCD drive signals, CCD clock drivers and their overlap generation circuits, video amplifier with four selectable gains for CCD output signal processing, CCD bias and supply voltage generation circuits, CCD temperature control components. DEM operation is controlled by the ELU. The ELU sends the clock control sequence to DEM in real time, provides DEM supply voltages and receives the video signal from DEM. The DEM contains the circuits which are required to be in the proximity of the CCD. Cable length between ELU and CCD would have detrimental effects on the signals concerned if these circuits would be part of the ELU, and therefore these circuits are accommodated in the DEM.

The IAM is the interface between the ELU and the Aura spacecraft. The purpose of the IAM is to make the OMI interface compliant to the interface of the spacecraft. The main functions of the IAM are to process the commands it receives from the spacecraft

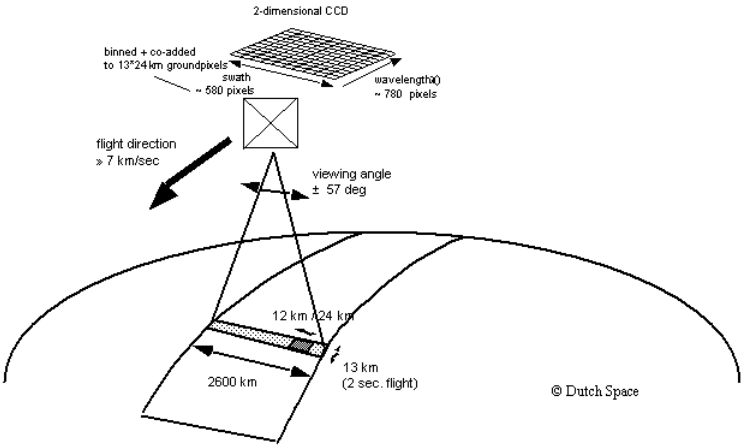

FIGURE 2.17: OMI measurements concept. Courtesy of Dutch Space.

and to send these to the ELU, to format the telemetry it receives from the ELU and send it to the spacecraft, to synchronise the clocks from the spacecraft and the ELU.

2.2.4 Operations

Apart from highly resolved spectral information, OMI's largest asset is the obtained high spatial resolution, combined with daily global coverage. The spatial resolution of OMI is unprecedented for UV/VIS satellite instruments. The nadir pointing telescope of OMI has a very large field of view of 114°, which is used for swath registration, perpendicular to the flight direction of the satellite. Due to this wide field of view of 114°, the OMI swath width is 2600 km, which provides, in combination with the 14 daily orbits, a daily global coverage. The use of 2-D CCD detectors enables to measure the spectral and spatial information at the same time.

Differently from the SCIAMACHY, the OMI can only operate in nadir. A nadir swath, in relation to the CCDs, is reported in Fig. (2.17).

Within this observation set-up, different measurement modes can be identified. The main observation mode for OMI is the Global Measurement mode. The OMI can measure with two additional modes: the Spatial Zoom-in Measurement mode and the Spectral Zoom-in Measurement mode. Tab. (2.5) summarizes these different procedures with their main characteristics.

In a normal OMI Earth's radiance observation, five measurements with an exposure time of 0.4 s are co-added, resulting in a pixel size in the flight direction of 13 km, independent of the operation mode. Other exposure times are also used; however, the total effective integration time of an exposure remains always 2 s. The nominal exposure

Channel	Spectral Range (nm)	Swath Width (km)	Ground Pixel Size (km)
	Global Observation Mode		
UV-1	270-310	2600	13 × 48
UV-2/VIS	310-500	2600	13 × 24
	Spatial Zoom-in Observation Mode		
UV-1	270-310	2600	13 × 24
UV-2/VIS	310-500	725	13 × 12
	Spectral Zoom-in Observation Mode		
UV-2	306-364	2600	13 × 12
VIS	350-432	2600	13 × 12

TABLE 2.5: Characteristics of the main observation modes. Adapted from [82].

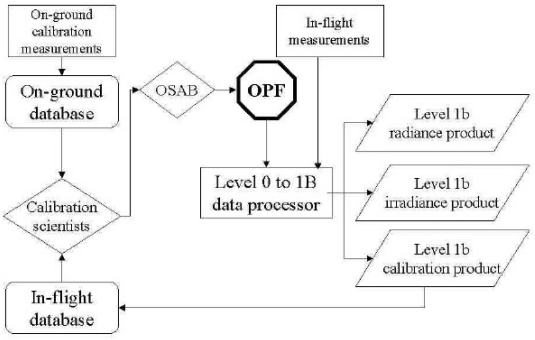

FIGURE 2.18: OPF relations with relevant products and processors [81].

time is optimized to have simultaneously a sufficient signal in the UV-1 channel and no saturation in the VIS channel.

2.2.5 Calibration and Monitoring

As discussed for the SCIAMACHY sensor in Sec. (2.1.4), the goal of the calibration effort is to convert the detectors readout to useful physical quantities. For the OMI, this is achieved with the aid of the the Operational Parameters File (OPF) [81]. This file contains the information needed to run the Level 0 to 1b processor, to convert the readout (Level 0 data) to radiances and irradiances (Level 1b data). The parameters stored in the OPF come from the on-ground and in-flight calibration activities. The inter-connections of the OPF with other relevant products and processors are shown in Fig. (2.18).

The calibration of OMI is composed of some intermediate steps [82]. The Ground Data Processing System (GDPS) performs the correction by considering twelve correction algorithms for radiances and one additional for irradiances. All correction algorithms use parameters stored in the OPF. The choice to use correction parameters from an OPF instead of the actual measurement is driven by the consideration that the parameters in

the OPF are derived from numerous (calibration) measurements and, therefore, have a better precision than correction parameters based on a single measurement. However, the processor also contains a number of flagging algorithms that set flags in the data product when a measured parameter deviates too much from its OPF value. Next to the correction algorithms and the flagging algorithms the GDPS also contains calculation algorithms that are used to evaluate OPF parameters for each measurement. Such an evaluation consists of applying, e.g., wavelength, binning factor or temperature corrections to an OPF parameter. The correction steps involved are similar to those described for the SCIAMACHY; in the following a brief description is given for the known issues in calibration.

The ELU introduces non-linearity effects. When the signal reaches the readout electronics, the accumulated charge is converted to an analogue voltage at the capacitance of the CCD. The CCD pre-amplifier causes a small nonlinearity in this process which must be corrected. A small, gain-dependent, offset voltage is applied to ensure a positive value to the resulting signal. In addition, for irradiances, a division by appropriate electronic gain ratio to convert signal to reference gain factor unity is done. A non-linearity correction is applied based on the evaluation of a fourth order polynomial [82]. Other small issues still exist but are not treated here in full details. The overall readout noise can be derived per pixel from the variance in histograms distribution of time series of dark measurements.

The dark signals are likely to increase for proton damage to the OMI CCD detectors; this well known effect is called Random Telegraph Signal (RTS) [83]. On-ground testing has shown this possibility. To minimize this effect, a 10 kg aluminium shielding was added to shield the detector modules and CCDs [82]. The RTS in dark signal measurements manifests itself as a type of behavior where the output of a pixel is unstable and shows evidence for jumps between multiple more or less stable energy levels. This is a statistical process and the time constants of such jumps can vary per pixel. It is known from literature that the time constants between jumps become longer when the CCD temperature is lowered; at this aim the temperature of the CCDs is brought to low values. Fig. (2.19) shows the time histograms (left) and dark currents (right) as a function of time, for three individual pixels . In these cases pixels were hit by a protons in the period November 25 to December 1, 2004. Before being hit these pixels behaved normally and as expected, i.e., with one dark current level and expected noise behavior with an occasional spike that causes no permanent damage. Fig. (2.19(a)) shows an example of a pixel that was hit twice in one week, but still behaves normally, albeit with higher dark current. Fig. (2.19(b)) shows an example of a pixel that shows regular RTS after being hit, at 2 or 3 energy levels, as confirmed by the histogram on the left. Fig. (2.19(c)) shows an example of a pixel that shows erratic RTS behavior after being hit,

with multiple energy levels or maybe even with a continuum of energy levels (see the histogram to the left). Fortunately, the latter category of RTS pixels, after proton hits, are a minority, with most pixels behaving as exemplified in Fig.s (2.19(a)) and (2.19(b)), if hit by a particle.

The wavelength calibration is the assignment of a vacuum wavelength to a given CCD pixel. The initial calibration was done by using a SLS. More accurate wavelength calibration is done in-flight using Fraunhofer lines in both sun and Earth spectra. The procedure for spectral calibration is based on the fact that the spectral calibration of OMI will change only slightly as a function of the temperature of the OPB. Furthermore, OMI will provide a very stable thermal environment with a high repeatability of the OPB temperature along the orbit. Therefore it has been decided to parameterize the wavelength calibration as a function of OPB temperature. The OPF contains wavelength polynomial coefficients for all image rows for a given reference temperature of the OPB. The temperature of the OPB at the time of a measurement, as measured by thermistors, is used to calculate corrected wavelength polynomial coefficients for each image row, that is, for each (ir)radiance spectrum. These corrected wavelength polynomial coefficients are provided in the Level 1b radiance and irradiance products. The reason for providing wavelength polynomial coefficients in the Level 1b data products, instead of providing actual wavelengths, is that it considerably reduces the size of a data product. The wavelength calibration of the OMI is given by:

$$\lambda_{ij} = \sum_{k=0}^{N} c_{kj} i^k \tag{2.6}$$

where i is the column number, j the row number and c_{kj} are the wavelength calibration polynomial coefficients.

The spectral stray light behavior of the instrument was extensively characterized and calibrated on the ground. The most critical wavelength range, as far as spectral stray light is concerned, is the UV1 channel with wavelength range 265 to 310 nm, and especially the wavelength range below 290 nm, where the useful radiance signal is two orders of magnitude lower than at 310 nm as a result of the ozone absorption. The optical design of the instrument has been optimized to reduce spectral stray light below 290 nm. The uncorrected measured spectral stray light fraction at 270 nm is about 8% of the useful signal. Therefore, an additional correction to reduce spectral stray light below 1% after correction is required; a spectral stray light correction algorithm is implemented in the Level 0-1b data processing, whose effect has been proved to be the reduction of the stray light effect by a factor 5-10. As a representative example, Fig. (2.20) shows the spectral stray light fraction at 290 nm in UV1 as a function of the source wavelength.

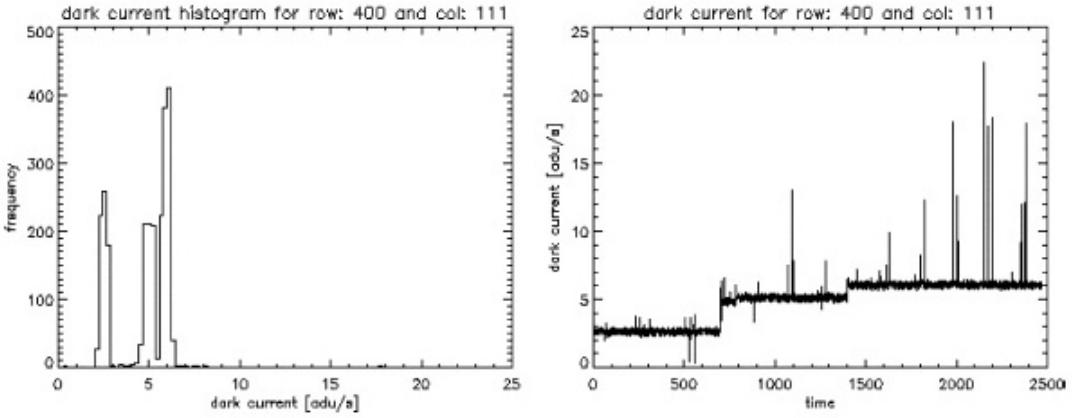

(a) Pixel at row 400 and column 111 in the UV channel

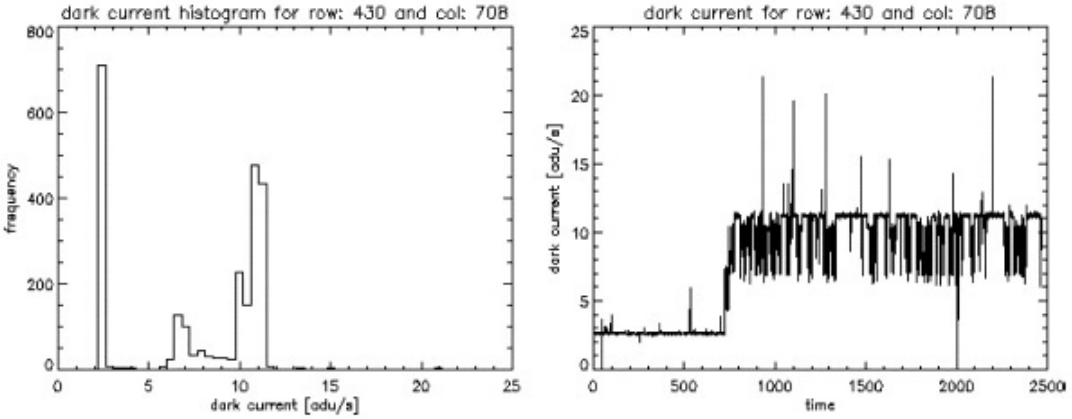

(b) Pixel at row 430 and column 708 in the UV channel

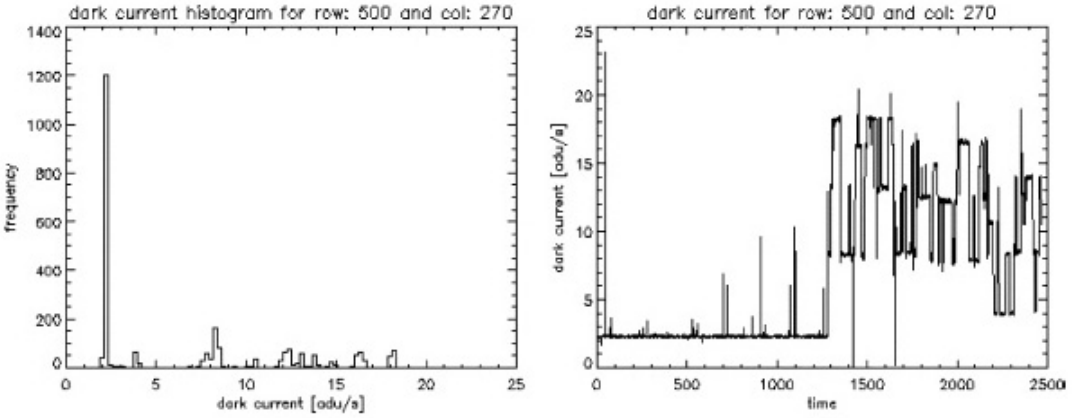

(c) Pixel at row 500 and column 270 in the UV channel

FIGURE 2.19: Time histograms (left) and dark currents as a function of time (right) for 3 pixels hit by a proton and showing a RTS behavior [82].

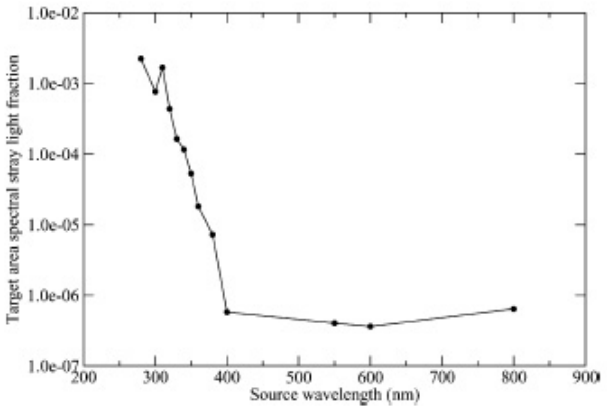

FIGURE 2.20: Spectral stray light fraction in UV1 at 290 nm as a function of the source wavelength [82].

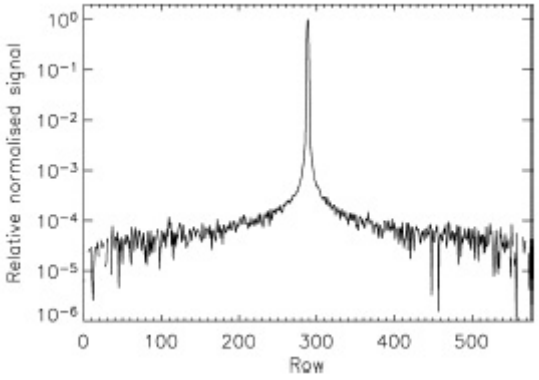

FIGURE 2.21: Spatial stray light at column 300 (about 340 nm) in UV2 with source illumination at nadir [82].

The Fig. shows that source regions above 350 nm hardly contribute to the spectral stray light in UV1 [82]. Because the ozone profiling algorithms that use the UV1 signals are sensitive to stray light it is important to validate and possibly optimize the spectral stray light algorithm and calibration parameters using in-flight radiance measurement data.

Spatial stray light is light intended for a specific viewing direction ending up at another viewing direction. In general, spatial stray light and spectral stray light are mixed, i.e., light can end up at another viewing direction as well as at another wavelength. The OMI instrument radiance port spatial stray light behavior has been characterized on the ground. Fig. (2.21) shows a representative result for UV2 channel. No correction algorithm has been implemented in the Level 0 to 1b processing for spatial stray light.

The radiometric calibration of the OMI instrument can be obtained with separate parameters. The absolute radiance and irradiance radiometric calibrations provide the radiometric calibration parameters for the Earth and sun measurements, respectively.

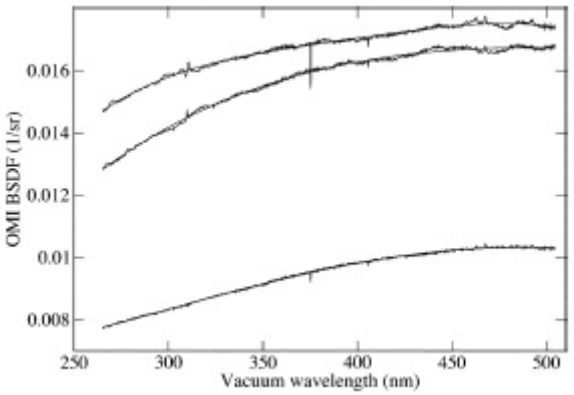

FIGURE 2.22: Measured and fitted OMI instrument BSDF for the three onboard diffusers for nadir viewing angle and nominal azimuth and elevation angles. The curves show the BSDF results for the backup aluminum diffuser, the regular aluminum diffuser, and the quartz volume diffuser from top to bottom [82].

Most of the optical components are common to the radiance and irradiance optical paths. The optical sensitivity of these common components thus cancels in the ratio of the Earth and sun measurements, and equally in the ratio of radiance and irradiance calibrations. This ratio is called the OMI instrument Bidirectional Scattering Distribution Function (BSDF). This BSDF can be determined with higher accuracy than the absolute radiance and irradiance calibration parameters. The BSDF, i.e., the ratio of the radiance and the irradiance calibrations, is in first order determined by the optical components that are not common to the radiance and irradiance modes. Thus, the BSDF can be approximated by the ratio of the primary telescope mirror 003 in the radiance mode over the solar mesh, the onboard diffuser and the folding mirror C03 in the irradiance mode. Therefore, unlike the radiance and irradiance calibrations, it is a smooth and regular function of wavelength and viewing angle. The BSDF calibration determines the calibration of the in-flight absolute Earth reflectance measurement data. The absolute Earth reflectance data are used as input for nearly all scientific atmospheric retrieval algorithms. This makes the OMI instrument BSDF the most important radiometric calibration parameter. On ground the OMI BSDF has been measured using dedicated optical stimuli. The BSDF is a function of wavelength (CCD column), viewing direction (CCD row) and incident angles of the diffuser. Fig. (2.22) shows the measured BSDF results for a viewing angle of 0° for the three onboard diffusers. It can be observed that the curves are smooth functions of wavelength, apart from some structure resulting from the optical stimulus and the onboard diffuser features. During the OMI instrument BSDF calibration the unknown BSDF of the instrument is calibrated against the known BSDF of the external spectralon plate, whose behavior is close to a perfect Lambertian diffuser. The final accuracy for the OMI instrument absolute BSDF radiometric calibration parameter as determined on ground is about 4%. The swath angle dependency

of the BSDF is accurate to about 2%. In flight the absolute irradiance calibration can be verified accurately, because the solar irradiance is known to an accuracy of 1% to 2%. The OMI BSDF is verified using techniques developed for the TOMS and the BUV instruments. Methods typically involve comparisons between observed and theoretical reflectances (e.g. measurements over the Antarctic or Greenland ice scenes), and can also include direct comparisons with other satellite measurements.

No polarization correction is needed because the instrument is made insensitive to the polarization of the incoming radiances by employing a polarization scrambler.

2.2.6 The Aura Validation Data Center

The data used for OMI-related work were taken from the AVDC database. The Aura Validation Data Center (AVDC) is a centralized, long-term, partially restricted archive for validation data hosted by the Atmospheric Chemistry and Dynamics Branch at the National Aeronautics and Space Administration (NASA) Goddard Space Flight Center (GSFC) in Greenbelt, Maryland. The AVDC mission is to support the EOS-Aura validation and science activities, and the future A-Train Earth Science satellites validation activities [84]. Data archived at the AVDC originates from e.g. several special Aura validation campaigns, NASA aircraft and balloon deployments, established measurement networks for collection atmospheric data, the Network for Detection of Atmospheric Composition Change (NDACC), the SHADOZ, the World Meteorological Organization (WMO)'s Global Atmosphere Watch (GAW), the Goddard Earth Sciences Data and Information Services Center (GES DISC). The AVDC also supports the Aura mission by providing auxiliary meteorological data to enhance the science value of the validation data. In addition, orbit prediction tools are available to locate and predict satellite overpasses, co-located data products, and provide satellite instrument Field of View (FoV) data. The access to some areas of the Aura Validation Data Center and the AVDC archive are guided by the AVDC data access protocol.

Pasquale Sellitto: sellitto@disp.uniroma2.it

Chapter 3

The inversion issue in remote sounding

3.1 Introduction

Remote sensing is the acquisition of information of an object or phenomenon by means of a sensing device that is not physically in contact with the object itself [85–87]. In general usage, this term refers to the use of sensor technology including instruments aboard aircraft or spacecraft platforms. Remote sensing applications may also be related to other fields including e.g. medical imaging, particle physics, etc. Remote sensing techniques always involve a *vector* of the information to reach the remote observer; in most cases this *vector* is the electromagnetic radiation. In Earth Observation field, radiation can originate from the Earth itself, sun radiation can be reflected or scattered from the Earth, or can be generated from the observing system (in the case of *active sensors*). Depending on the considered wavelength bands and the object to be observed, different interactions between the natural or stimulated radiation and the objects in the *optical path* may occur. This interaction is the actual *source* of information.

The remote measurement, i.e. measurement of radiation, is usually a more or less complicated function of the parameters that we actually want to estimate. The distinguishing characteristic of these measurements is not the remoteness, but the fact that the measurements are *indirect*. The observer, measuring the radiation at his remote location, must extract the useful information from the *measurements*, eventually taking into consideration systematic and instrumental errors and natural occurring disturbances (e.g atmospheric effects in observation of the ground or the effects of aerosols in remote sensing of ozone). Here originates the *inversion issue*. The general problem of the interpretation of this kind of measurements is generally known as the *inverse problem*. In

the following we will give a statement of the problem (section 3.2.1) and we will discuss this issue in the general physical approach context (overall section 3.2). Finally we will introduce statistical methods for the solution of this problem and in particular Neural Networks (NNs) algorithms (section 3.3) whose use for atmospheric sounding will be the core of this thesis work.

3.2 Physical approach to the inversion issue

We now give a brief overview of the inversion issue with a physical approach i.e. by the use of a physical *forward model*. For further reference please consider e.g. [88, 89].

3.2.1 Statement of the problem

Let's suppose we want to measure a scalar quantity from space. Let's start considering an ideal planet without atmosphere or a remote measurement without any atmospheric disturbance. Let's finally consider that we know exactly the effect of variations of radiance values measured from space in a certain geometry depending on our scalar parameter's variations. If so, our measured quantity y will be related to the quantity x we want to measure by means of the function f, the forward model:

$$y = f(x) \tag{3.1}$$

If the problem is linear or can it be linearized around the point (x_0, y_0) we can derive x in the following way:

$$x = k^{-1}(y - y_0) + x_0 \tag{3.2}$$

where k is a proportionality constant and $y_0 = f(x_0)$.

If we consider another quantity to retrieve, we'll need to measure at least another quantity from the spaceborne sensor. In the case we have exactly the same number of *ideal* measurements, e.g. the Earth's backscattered radiance at two wavelengths, and of quantities to retrieve, the forward problem takes the following form:

$$y_1 = k_{11}x_1 + k_{12}x_2 \tag{3.3}$$

$$y_2 = k_{21}x_1 + k_{22}x_2 \tag{3.4}$$

This simple inverse problem can be solved by plotting the two following straight lines on a graph of x_1 vs x_2:

$$x_2 = \frac{(y_1 - k_{11}x_1)}{k_{12}} \tag{3.5}$$

$$x_2 = \frac{(y_2 - k_{21}x_1)}{k_{22}} \tag{3.6}$$

and the solution will be the intersection point $(\overline{x_1}, \overline{x_2})$. This kind of situation is called a *well-posed* problem and has a unique solution. Suppose now to have only one equation (e.g. a radiometer that operates at only one wavelength). Than we will not have two but only one straight lines that will be the place of the infinite possible solutions for our inverse problem. This is a case of an *under-constrained* problem. It is also possible to have more equations than unknown i.e. a *over-determined* problem. In our ideal case a hypothetical third measurement tells us nothing about the quantities to retrieve. In an actual case is quiet unlikely that there's a unique solution to this problem i.e. the three straight lines intersecting at the same point.

In the case of *profile quantities* retrieval, the problem is in general under-constrained, also due to the continuous nature of the object to be retrieved. Usually, the infinite dimensionality of under-constrained problems' solutions can be reduced by the use of some *a priori* information on the searched quantity. An experimental error has also to be considered.

3.2.2 Inversion theory for profile quantities

3.2.2.1 Introducing the height dependency

Now we consider nadir sounding. Starting from a finite number of information pieces, i.e. measured radiances at different wavelengths, we want to estimate a continuous function, e.g. vertical profiles. Usually the continuous function of height is replaced with a discrete succession of values at different heights; this obviously introduces some error. We can generalize Eq. (3.1), in its linearized form, at a certain wavelength in the following way:

$$y_i = \int_0^\infty x(z)K_i(z)dz \tag{3.7}$$

or, for a discrete output:

$$y_i = \sum_{j=1}^{n} K_{ij} x_j \Rightarrow \mathbf{y} = \mathbf{K}\mathbf{x} \tag{3.8}$$

Generally $\mathbf{y}$ is called the *measurement vector* and $\mathbf{x}$ the *state vector*. Equation 3.8 is still valid for nonlinear problems if linearized e.g. by means of a Taylor series. In this latter case $K_{ij} = \frac{d(f(\mathbf{x}))_i}{dx_j}$. The rows of $\mathbf{K}$ are often called *weighting functions*.

The equation 3.8 can be regarded as a set of simultaneous equations and has different solutions depending if the problem is well-posed, under-constrained or over-determined. A general problem is that $\mathbf{K}$ usually is nearly singular and the presence of noise in the measurements vector can jeopardize the possibility of finding a solution of the inverse problem. The nearly singular nature of the matrix $\mathbf{K}$ is due to the fact that usually the weighting functions overlap to a large extent and so one satellite channel gives nearly the same information as another.

Let's start from equation 3.8. We now consider the linearized form of it around the reference state vector $\mathbf{x_r}$ and we add some instrumental noise.

$$\tilde{\mathbf{y}} = \mathbf{K}\tilde{\mathbf{x}} + \epsilon \tag{3.9}$$

where $\tilde{\mathbf{y}} = \mathbf{y} - \mathbf{F}(\mathbf{x_r}, \mathbf{b})$ is the difference between the measured spectrum and the modeled spectrum if the state is defined by the reference state $\mathbf{x_r}$, $\tilde{\mathbf{x}} = (\mathbf{x} - \mathbf{x_r})$ is the difference between the unknown states and the reference state and ϵ collects the measurement errors and uncertainties on the forward model parameters.

Usually an *a priori* knowledge $\mathbf{x_a}$ of the parameters to be retrieved is employed as the reference state to linearize the problem. The inverse problem solution is the retrieved state vector $\overline{\mathbf{x}}$:

$$\overline{\mathbf{x}} = \mathbf{x_a} + \mathbf{A}(\mathbf{x} - \mathbf{x_a}) + \mathbf{D_y}\mathbf{K_b}(\mathbf{b} - \mathbf{b_a}) + \mathbf{D_y}\epsilon \tag{3.10}$$

where $\mathbf{K_b}$ takes into account the derivatives of the forward model with respect to its parameters $\mathbf{b}$ and $\mathbf{D_y}$ is deputed to the inversion itself. In Eq. (3.10), $\mathbf{A} = \mathbf{D_y}\mathbf{K_x}$ is called *averaging kernel matrix*, with $\mathbf{K_x}$ obtained with the derivatives of the forward model with respect to the state vector elements.

To circumvent the problem of the quasi-singularity of $\mathbf{K}$ and to manage the instrumental errors we must regard all variables as random variables and solve the problem in terms of the Bayesian statistics.

3.2.2.2 A Bayesian approach

The problem here described, as many other estimation problems, can be solved in the framework of the Bayesian theory. The Bayes theorem solves the inversion problem by determining the *a posteriori* probability density function of the state vector $\mathbf{x}$ once we have made a measurement $\mathbf{y}$. This quantity is defined as:

$$\mathcal{P}(\mathbf{x}|\mathbf{y}) = \frac{\mathcal{P}(\mathbf{y}|\mathbf{x})\mathcal{P}(\mathbf{x})}{\mathcal{P}(\mathbf{y})} \tag{3.11}$$

We can calculate $\mathcal{P}(\mathbf{y}|\mathbf{x})$ using the forward model, and so derive $\mathcal{P}(\mathbf{x}|\mathbf{y})$. Starting from this latter estimate, we can find the state vector $\overline{\mathbf{x}}$ for which the probability density function is maximum.

We can assume that all the probability density functions are Gaussian distributions, that for a random vector takes the form:

$$\mathcal{P}(\mathbf{v}) = \frac{1}{(2\pi)^{\frac{n}{2}}|\mathbf{S}|^{\frac{1}{2}}} e^{\left(-\frac{1}{2}(\mathbf{v}-\overline{\mathbf{v}})^T\mathbf{S}^{-1}(\mathbf{v}-\overline{\mathbf{v}})\right)} \tag{3.12}$$

Considering the probability density function defined in Eq. (3.12), for the Bayes theorem of Eq. (3.11) we obtain:

$$-2\ln\mathcal{P}(\mathbf{x}|\mathbf{y}) + c = (\mathbf{x}-\mathbf{x_a})^T{\mathbf{S_a}}^{-1}(\mathbf{x}-\mathbf{x_a}) + (\mathbf{y}-F\mathbf{x})^T{\mathbf{S_y}}^{-1}(\mathbf{y}-F\mathbf{x}) \tag{3.13}$$

where c is a constant containing also $\mathcal{P}(\mathbf{x})$, $\mathbf{x}_a$ is the *a priori* profile, $\mathbf{S_a}$ and $\mathbf{S_y}$ are the covariance matrices of the *a priori* profile and the measurements vector i.e. taking into account the experimental errors. Both terms on the right-hand side of 3.13 are *quadratic forms*; the sum of two quadratic form is still a quadratic form, so we can say:

$$-2\ln\mathcal{P}(\mathbf{x}|\mathbf{y}) + c = (\mathbf{x}-\overline{\mathbf{x}})^T\overline{\mathbf{S}}^{-1}(\mathbf{x}-\overline{\mathbf{x}}) + c \tag{3.14}$$

From equation 3.14 is possible to derive the profile. In fact, if we consider a linear (linearized) forward model, and so $F\mathbf{x} = \mathbf{K}\mathbf{x}$, we have:

$$\overline{\mathbf{x}} = ({\mathbf{S_a}}^{-1} + \mathbf{K}^T{\mathbf{S_y}}^{-1}\mathbf{K})^{-1}({\mathbf{S_a}}^{-1}\mathbf{x_a} + \mathbf{K}^T{\mathbf{S_y}}^{-1}\mathbf{y}) \tag{3.15}$$

This problem may also be seen as related to the minimization of the following cost function :

$$\mathcal{C} = (\mathbf{x} - \mathbf{x_a})^T \mathbf{S_a}^{-1} (\mathbf{x} - \mathbf{x_a}) + (\mathbf{y} - F(\mathbf{x}))^T \mathbf{S_y}^{-1} (\mathbf{y} - F(\mathbf{x})) \tag{3.16}$$

3.2.2.3 Error estimation

The equation 3.15 can be written in several manners. A very useful way is the following:

$$\overline{\mathbf{x}} = \mathbf{x}_a + \mathbf{S}_a \mathbf{K}^T (\mathbf{K} \mathbf{S}_a \mathbf{K}^T + \mathbf{S}_y)^{-1} (\mathbf{y} - \mathbf{K} \mathbf{x}_a) \tag{3.17}$$

or, simply:

$$\overline{\mathbf{x}} = \mathbf{x}_a + \mathbf{D} (\mathbf{y} - \mathbf{K} \mathbf{x}_a) \tag{3.18}$$

Using the definition of *measurement* $\mathbf{y} = \mathbf{K}\mathbf{x}_t + \epsilon$, starting from equation 3.18 we obtain:

$$\overline{\mathbf{x}} = \mathbf{x}_a + \mathbf{D}\mathbf{K} (\mathbf{x}_t - \mathbf{x}_a) + \mathbf{D}\epsilon \tag{3.19}$$

or:

$$\overline{\mathbf{x}} - \mathbf{x}_t = (\mathbf{I} - \mathbf{A})(\mathbf{x}_a - \mathbf{x}_t) + \mathbf{D}\epsilon \tag{3.20}$$

where we used the averaging kernel matrix $\mathbf{A} = \mathbf{D}\mathbf{K}$. From equation 3.20 is possible to understand the two sources of errors in the estimated profile. The first term is referred as the *smoothing error* and is related to the vertical resolution of the instrument performing the measurement $\mathbf{y}$. The rows of $\mathbf{A}$, in particular, are called *averaging kernels*. In remote sensing problems they usually have a peak at a certain altitude; features in the true profile which are narrower than the averaging kernel width cannot be measured and are smoothed out in the retrieved profile. The second term in equation 3.20 is the measurement error. It is clear that even small errors in the measurement can produce huge oscillations in the retrieved profile depending on the values of $\mathbf{D}$ elements.

3.2.2.4 Non linear optimal estimation approach

The assumption that brought to the definition of Eq. (3.15) is that the quantity $\mathbf{x}$ that we want to retrieve is linearly related to the quantity $\mathbf{y}$ that we measure. In general

this is never exactly true, so we cannot pose the problem as in equation 3.9, but in the following way:

$$\mathbf{y} = F(\mathbf{x}) + \epsilon \simeq F(\mathbf{x}_0) + \mathbf{K}(\mathbf{x} - \mathbf{x}_0) \tag{3.21}$$

In Eq. (3.21), $\mathbf{x}_0$ is the *linearization profile*. The cost function of equation 3.16 in this case takes the form:

$$\mathcal{C} = (\mathbf{x} - \mathbf{x_a})^T {\mathbf{S_a}}^{-1}(\mathbf{x} - \mathbf{x_a}) + (\mathbf{y} - \mathbf{y}_0 - \mathbf{K}(\mathbf{x} - \mathbf{x}_0))^T {\mathbf{S_y}}^{-1}(\mathbf{y} - \mathbf{y}_0 - \mathbf{K}(\mathbf{x} - \mathbf{x}_0)) \tag{3.22}$$

If we try to minimize $\mathcal{C}$ in *moderately nonlinear* cases, we find that, e.g., putting to 0 the derivative of the cost function does not bring to a minimum but just to a value that is smaller than $\mathcal{C}(\mathbf{x}_0)$. We can take this estimation and re-apply the formula; we have an iterative solution that is a particular case of the so called *Inverse Hessian Method*. The profile at the iteration $i+1$ is related to that at the iteration i in the following way:

$$\mathbf{x}_{i+1} = \mathbf{x}_i + ({\mathbf{S_a}}^{-1} + \mathbf{K}_i^T {\mathbf{S_y}}^{-1}\mathbf{K}_i)^{-1}[\mathbf{K}_i^T \mathbf{S}_y^{-1}(\mathbf{y} - F(\mathbf{x}_i)) - \mathbf{S}_a^{-1}(\mathbf{x}_i - \mathbf{x}_a)] \tag{3.23}$$

The solution in Eq. (3.23), or similar Eq.s, is often used in ozone profiles retrieval algorithms for nadir UV/VIS satellite data, e.g see [59, 60].

3.2.2.5 Error estimation in non linear case

As for the linear case, error sources are mainly measurement errors and smoothing errors. Error estimation may include forward model errors or model parameters errors. In the iterative case, we can still use equation the following equation, valid for linear case:

$$\overline{\mathbf{S}} = (\overline{\mathbf{K}}^T \mathbf{S}_y^{-1} \overline{\mathbf{K}} + \mathbf{S}_a^{-1})^{-1} \tag{3.24}$$

where the $\overline{\mathbf{K}}$ is related to the last iteration.

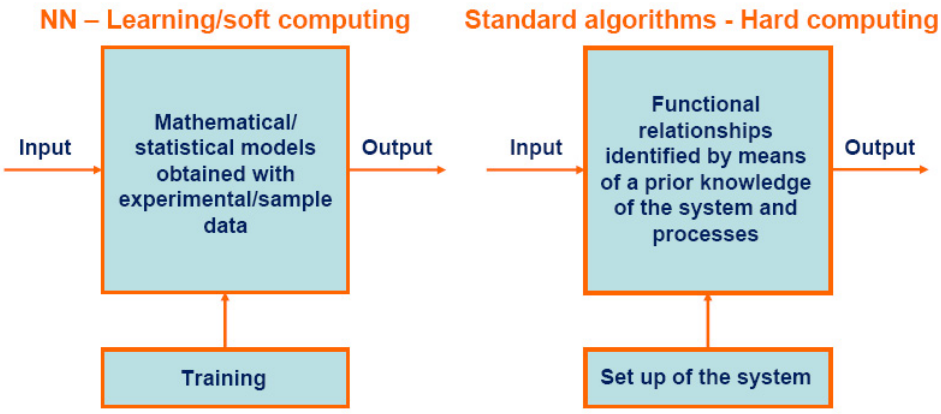

FIGURE 3.1: Summary of the differences between soft and hard computing algorithms.

3.3 Neural networks algorithms

In this Sec., a general overview of artificial neural networks, aiming at understanding the basic concepts for the application to the solution of the inverse problem, will be given. Further details can be found in, e.g., [90–92].

3.3.1 Introduction

Neural networks algorithms belong to the class of *soft computing* techniques [92]; they identify dependencies of variables by means of the so called *training phase*, using training (sample) datasets. After the training phase a NN can represents a non-linear multivariate function. Soft computing algorithms are usually counterposed to *hard computing* algorithms, which, conversely, need a prior knowledge of the functional relationships of involved variables and of the modeled systems and phenomena. Fig. (3.1) summarize differences between these two classes of algorithms.

NNs solve regression and classification problems by varying some parameters called *weights* (w) that control the way NNs *learn* through the training dataset. Model performances are monitored by means of an error (or cost) function $E = E(w)$. The error function is non-linearly dependent on the weights and the resulting hypersurface in the weights space doesn't have a unique and guaranteed minimum. So, the problem of NNs' training falls into the category of non-linear optimization problems.

3.3.2 Basic principles of the Multilayer Perceptron

Within the general category of NNs algorithms several different schemes can be identified. A first subdivision can be made in terms of the learning phase, that can be

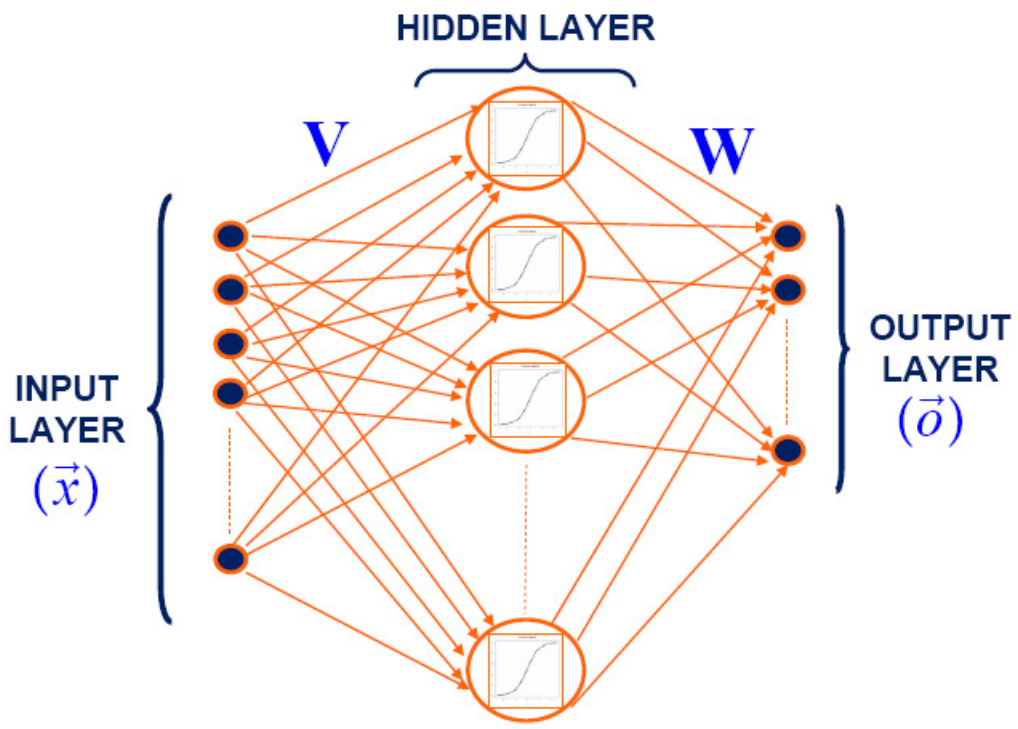

FIGURE 3.2: Scheme of a MLP.

supervised or *unsupervised*. In the first case a set of example input-output pairs are given, and the aim is to find a function, in the allowed class of functions, that matches the examples. In other words, we wish to infer the mapping implied by the data; the cost function is related to the mismatch between our mapping and the data and it implicitly contains prior knowledge about the problem domain. In the second case some data are given, and the cost function to be minimized can be any function of the data and the network's output. Tasks that fall within the paradigm of unsupervised learning include clustering, estimation of statistical distributions, compression and filtering. Further subdivisions may be made depending on NNs architecture.

We restrict our attention to the feedforward (no reaction) MultiLayer Perceptron (MLP) with supervised learning (see Fig. (3.2)).

Like different NNs, a MLP is made by elementary computing units called *neurons* linked by means of weighted synapses. A neuron accept some inputs, and then process the sum of their *weighted* values by means of the so-called *Activation Function* (AF).

Genuine NNs are those with at least two layers of neurons, a hidden layer (HL) and an output layer (OL), provided that the hidden layer neurons have nonlinear and differentiable AFs. Squashing sigmoidal functions, as the logistic function or the hyperbolic

tangent, are often used as AFs. The nonlinear activation functions in a hidden layer enable a neural network to be a universal approximator [93], see also Sec. 3.3.3. Thus, the nonlinearity of the AFs solves the problem of representation. The differentiability of the AF of the hidden layer neurons solves the nonlinear learning task. Generally, no processing will occur in the input layer, and although in its graphical appearance it looks like a layer, it is just not a layer of neurons. Rather, it is an input vector, eventually augmented with a bias term, whose components will be fed to the next layer of neural processing units. The output layer neurons may be linear, or they can have sigmoidal activation functions. There is a theoretically sound basis for the wide application of two-layered networks, which asserts that a network with an arbitrarily large number of nonlinear neurons in the hidden layer can approximate any continuous function $\Re^m \rightarrow \Re^n$ over a compact subset of $\Re^n$.

Once the MLP is trained, it represents the following mapping between the input space and the output space:

$$\mathbf{o}(\mathbf{x}, \mathbf{V}, \mathbf{W}, \mathbf{b}) = F(\mathbf{x}, \mathbf{V}, \mathbf{W}, \mathbf{b}) \tag{3.25}$$

where $\mathbf{x}$ is an m-dimensional input vector, $\mathbf{o}$ is an n-dimensional output vector, $\mathbf{b}$ is a vector of further NNs parameters called *bias vector* and $\mathbf{V}$ and $\mathbf{W}$ are input-to-hidden and the hidden-to-output weight matrices. To simplify the problem, let's first consider a mono-dimensional output. In this latter case, Eq. (3.25) is:

$$o(\mathbf{x}, \mathbf{V}, \mathbf{W}, \mathbf{b}) = F(\mathbf{x}, \mathbf{V}, \mathbf{W}, \mathbf{b}) = \sum_{j=1}^{HN} w_j \sigma_j(\mathbf{V}_j^T \cdot \mathbf{x} + b_j) \tag{3.26}$$

where the σs are the (sigmoidal) AFs of the HL.

Let us consider the two main aspects of NNs applicability: the *representation problem*, that is what can NNs approximate, and the *learning problem*, that is how can we let NNs represent what we need.

3.3.3 The representation problem

The representation problem is related to the problem of function approximation. In general if we consider the *true* unknown function that maps $\Re^m$ into $\Re^n$, with NNs we can find an approximation by means of the learning phase. It has been demonstrated that MLPs are universal approximators [93], providing a sufficiently large number of the hidden neurons with squashing sigmoidal AFs. In fact, the Weierstrass approximation

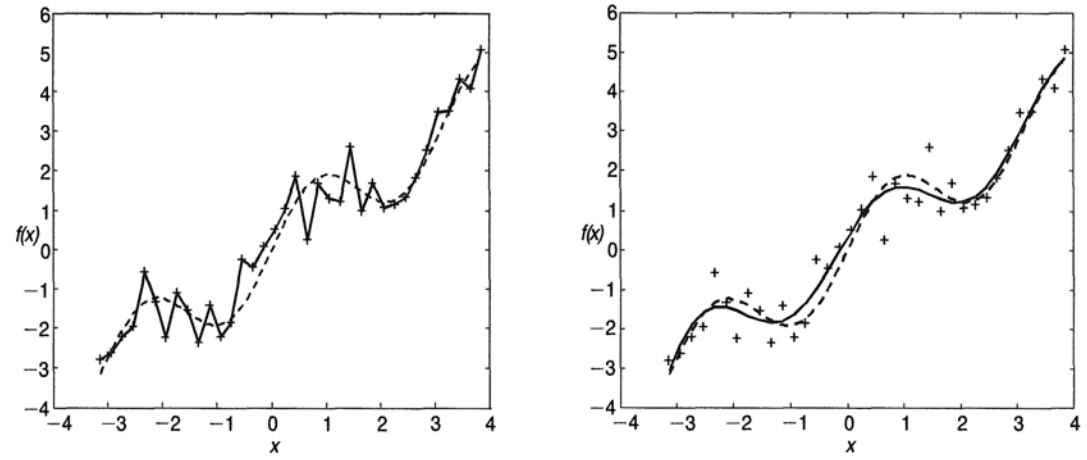

FIGURE 3.3: Two tentative approximation functions (thick line) of underlying function (dashed line) describing data (crosses). The case on the left reveals overfitting. Figure adapted from [92].

theorem, stating that every continuous function defined on an interval [a,b] can be uniformly approximated as closely as desired by a polynomial function, can be extended to sigmoidal functions by the following Cybenko-Hornik-Funahashi theorem.

Theorem 3.1. (Cybenko-Hornik-Funahashi Theorem)
$f_a(\mathbf{x}, \mathbf{W}) = \sum_{j=1}^{\bar{j}} w_j \sigma_j(\mathbf{V}_j^T \cdot \mathbf{x} + b_j)$ *is dense in* $\mathbb{C}[I_d]$, $I_d \in [0,1]^d$, *i.e.*
$\forall \mathbf{x} \in I_d$, $f(\mathbf{y}) \in \mathbb{C}[I_d]$, $\epsilon > 0$
$\exists f_a(\mathbf{x}, \mathbf{W}) : |f_a(\mathbf{x}, \mathbf{W}) - f(\mathbf{y})| < \epsilon$

with f and f_a the ideal and the approximating function between the **o** and the **x** vector variables.

As said, the order of the approximating function (number of terms in the summation in Eq. (3.26)), i.e. the number of the hidden neurons, is very important when designing a NNs algorithm. An insufficient dimensionality of the HL will not ensure a satisfactory approximating power, while an excessive dimensionality of the HL may bring overfitting, that is the interpolation of the training data and the loss of generalization abilities of the MLP; in addition it can model also the noise in the measurements, losing filter capabilities. Fig. (3.3) shows a case of overfitting (thick line on the left) and a case of reasonably successful approximation (thick line on the right) of the underlying function (dashed line) describing the data (crosses).

3.3.4 The learning problem

The learning problem in MLPs is related to the non linear optimization problem, i.e. given a parametric non linear function, one must find the more suitable configuration

of its parameters to fit the underlying unknown function describing the data. At this aim, an error or cost function must be defined to give an indication of the quality of the approximation. An example of an error function is the following:

$$E = \sum_{\overline{p}}^{p} [\mathbf{d}_p - f_a(\mathbf{x}, \mathbf{W})] = \sum_{\overline{p}}^{p} [\mathbf{d}_p - \mathbf{o}_p] \tag{3.27}$$

where the suffix p indicates the pattern through the dataset and $\mathbf{d}_p$ is the desired p-th output vector of the NN. The minimum of the error function can be found by means of adjustment of the parameters matrix $\mathbf{W}$ by learning from a dataset, exploiting a *gradient descent* criterium. Negative values of the gradient of the error function direct to the maximum decreasing of the hypersurface defined by $E(\mathbf{W})$. The error gradient is defined as follows:

$$\mathbf{g} = \nabla_w E(\mathbf{W}) = \begin{pmatrix} \frac{\partial E}{\partial w_1} \\ \vdots \\ \frac{\partial E}{\partial w_n} \end{pmatrix} \tag{3.28}$$

The weights are iteratively adjusted by the following scheme:

$$\mathbf{W}_{it} = \mathbf{W}_{it-1} + \eta_i \triangle \mathbf{W}_{it} \left(\mathbf{g}(\mathbf{W}_{it-1})\right) \tag{3.29}$$

In the next section we will more thoroughly analyze an application of the gradient descent criterium and we will introduce the error backpropagation algorithm.

3.3.4.1 The Error Backpropagation Algorithm

The basic idea behind the error backpropagation (EBP) algorithm is based on the consideration of a backpropagating error signal terms δ_{yj} for hidden layer neurons, calculated by backpropagating the error signal terms of the output layer neurons. This quantity is supposed to bring the gradient descent information. Fig. (3.4) schematically depicts this situation.

Backpropagation is still the most commonly used learning algorithm in the field of soft computing. The backpropagation of error through nonlinear systems was used in the field of variational calculus more than a hundred years ago. This approach was also used in the field of optimal control long before its application in learning in neural networks.

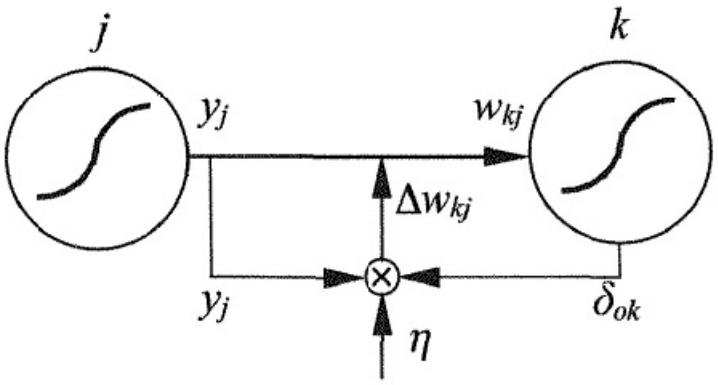

FIGURE 3.4: Weight w_{kj} connecting the j-th hidden layer neuron with the k-th output layer neuron and its adaptation Δw_{kj} in relation to backpropagating error signal δ_{ok}.

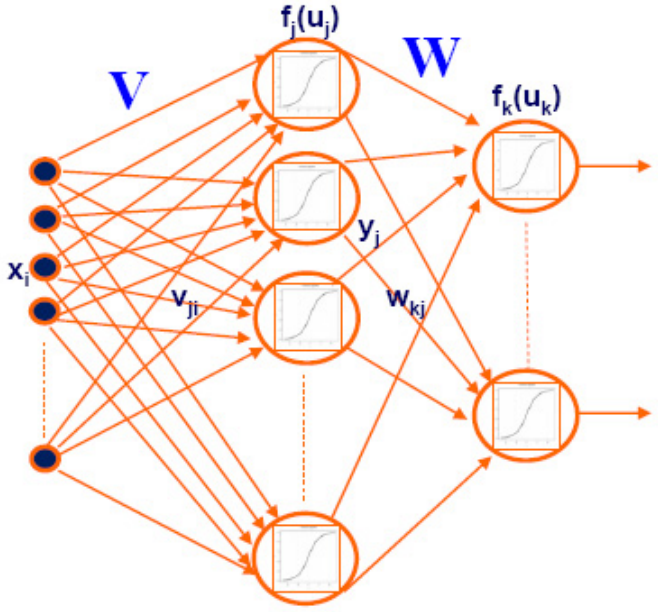

FIGURE 3.5: Detailed MLP scheme, with indication of backpropagating errors signals.

Rumelhart introduced the EBP within the framework of learning in neural networks [94].

Now we will give a brief analytical formulation of the EBP algorithm, with reference to Fig. (3.5). We start from the formulation of the cost function for a singular pattern of sample input-output data, see Eq. 3.29; the results presented here are easily extendible to a given number of patterns.

$$E = \frac{1}{2}\sum_{k=1}^{K}(d_k - o_k)^2 \tag{3.30}$$

The error signal from the k-th output is defined as:

$$\delta_{o_k} = -\frac{\partial E}{\partial u_k} = (d_k - o_k) f'(u_k) \tag{3.31}$$

In Eq. (3.31), u_k is the input to the k-th output neuron, and takes the form:

$$u_k = \sum_{j=1}^{J} w_{kj} y_j \tag{3.32}$$

with y_j the output of the j-th hidden neuron, and w_{kj} the weight of the synapsis connecting the j-th hidden to the k-th output neuron.

The k-th output is described by the following Eq.:

$$o_k = f_k(u_k) \tag{3.33}$$

The function f_k is the (sigmoidal) AF of the k-th output neuron.

Analogously to Eq. (3.31) we can define an error signal propagating from the hidden to the input layer:

$$\delta_{y_j} = -\frac{\partial E}{\partial u_j} = f_j'(u_j) \sum_{k=1}^{K} \delta_{o_k} w_{kj} \tag{3.34}$$

with obvious interpretation of the symbols (see also Fig. (3.5)).

As depicted in Fig. (3.4), the weights must be updated by the use of the backpropagated error signals, So the weight values, at the iteration it, take the form:

$$w_{kj}(\text{it}) = w_{kj}(\text{it}-1) + \eta \delta_{o_k} y_j \tag{3.35}$$

$$v_{ji}(\text{it}) = v_{ji}(\text{it}-1) + \eta \delta_{y_j} x_i \tag{3.36}$$

with δ_{o_k} and δ_{y_j} resulting from Eq.s (3.31) and (3.34), respectively.

Instead of the standard EBP learning algorithm, we have chosen the use of the scaled conjugate gradient (SCG) scheme [95] in all training phases within this thesis work. The SCG algorithm allows optimization in times shorter of more than one order of magnitude, by the use of a second derivative approach. The SCG underlying idea is analogous to

the standard EBP, dealing with a backpropagated error signal, and we will not give a detailed description here, sending the interested reader to the relevant references.

3.3.5 NNs and the retrieval of profile quantities

The problem of the retrieval of profile quantities from nadir spectra with NNs has similarities and symmetries with the OE approach. Let's now introduce a similar notation for NNs, starting from Eq. (3.21).

Essentially, we assume that an inverse mapping between spectral data and profile quantities exists, which can be approximated by the neural network model R according to the following Eq. (the inverse of Eq. (3.21)):

$$\mathbf{x} = R(\mathbf{y}, \mathbf{c}, \mathbf{w}) + \epsilon \tag{3.37}$$

where $\mathbf{x}$ is the ozone profile, $\mathbf{y}$ the spectral measurement data, $\mathbf{c}$ a vector of supplementary input parameters, ϵ an error vector, and $\mathbf{w}$ contains the network model parameters (the weights). The notation is quite similar than the one described in the previous sections for the OE. As for OE, to obtain the mapping that better approximates the underlying function that links the measurements to the atmospheric state, a cost function (the error function) must be minimized. Here the task is performed by varying the model parameters, i.e. the weights, to obtain the best configuration with respect to a set of training data from whom the net *learns* the inverse model.

3.3.6 Advantages and disadvantages of NNs algorithms

Once the training is done, the resulting mapping $\hat{\mathbf{R}}$ is optimal in a global sense, and can be applied to all observations solely as a forward model. This is in contrast to the OE method, which determines a new, locally optimal solution from each individual observation. Moreover, the iterative steps and the use of a forward model in OE can cause a significant computational effort to find the solution of the inverse problem. Another relevant advantages of the NNs over the OE is the more robustness to systematic errors in input data. Finally we have to consider that the use of an explicit forward model can introduce additional errors to the retrievals; this is particularly important in atmospheric applications, were clouds and aerosols can be difficult to be modeled.

Chapter 4

NNs for tropospheric ozone column retrieval from nadir UV/VIS SCIAMACHY data

Part of this Chapter's contents is extracted from the publications: [96–98].
This activity is performed in the context of ESA Cat-1 project no. 2930.

4.1 Introduction

Ozone is of crucial importance for the life in the Earth's biosphere, for its role in screening the harming UVB and UVA solar radiation. About 90% on average of atmospheric ozone is in the stratosphere where it absorbs almost all the UVB radiation, mainly owing to the Hartley and Huggins bands. The absorption of the UV radiation by ozone also determines the vertical temperature gradient in the stratosphere and contributes to the airmasses general circulation. The analysis of the observed ozone depletion in the stratosphere is a topical subject in environmental research as well as the managing of the application of international agreements such as the Montreal Protocol [4]. About 10% on average of atmospheric ozone is in the troposphere. Tropospheric ozone is a direct greenhouse gas [1]; its concentration is mainly determined by STE, and by photochemical reactions involving volatile organic compounds, nitrogen oxides, carbon monoxide, and other anthropogenic and natural occurring compounds. Other tropospheric ozone sources are transport from polluted areas and large-scale biomass burning. In the last decades enhancements in anthropogenic emissions of photochemical ozone precursors in the lower troposphere may have changed the balance, leading to an increase of ozone

concentration in the troposphere. In particular, a possible increasing trend of free tropospheric ozone has been observed up to the mid 80s when compared with pre-industrial ozone levels; in the following period no clear worldwide trend has emerged [7, 21, 99]. The tropospheric ozone radiative contribution has been estimated to provide the third largest increase in direct radiative forcing since the pre-industrial era [1]. Besides climatic effects, the increase of tropospheric ozone can have dramatic effects on public health and on vegetal culture growth. For these reasons, a global and continuous monitoring of ozone levels in the troposphere is necessary.

Measuring tropospheric ozone trends is a difficult task given its large interannual variability, variability of source and sink phenomena, and the scarce temporal and geographical coverage of observations [99]. Ground-based and ozonesonde measurements are mainly used for locally monitoring the ozone and are not apt to provide global and/or continuous coverage. Suitable complementary means may be satellite observations. The remote sensing technique, however, has a number of problems in terms of spatial resolution and sensitivity to the ozone in the lower layers of the atmosphere. Limb measurements can be used to gain height-resolved ozone information also at lower altitude levels. Nevertheless, it has to be noted that current limb measurements rarely measure tropospheric ozone below 200 hPa with a good quality; however their poor horizontal resolutions may compromise the quality of TOR retrievals (see Sec. 1.4.4.5, or in the following), in which stratospheric limb concentrations of ozone are subtracted from the total ozone measured by nadir observations. This could prevent from resolving short-range features of pollutants and atmospheric parameters. On the contrary, nadir measurements have better horizontal resolutions, but the nadir signal is weakly sensitive to ozone variations in the troposphere. The two measurement modes can be complementary, also considering the different spectral ranges at which they are acquired. The present techniques of satellite monitoring of tropospheric ozone are based on indirect retrievals such as TOR, e.g. [65–70, 100], or integration of the tropospheric concentration of ozone from pre-inferred ozone profiles [60, 101]. The first method uses measurements of two instruments, e.g. one nadir instrument operating in the UV measuring the total ozone column content, and one instrument measuring the stratospheric ozone concentrations, e.g. a MW limb sounder as the MLS in [65, 66]. The second method is generally based on optimal estimation schemes to derive vertical profiles of ozone concentration from nadir measurements; tropospheric ozone information is derived by using the known tropopause height to single out the stratosphere and troposphere. Besides the heavy computational requirements and the need of some a priori data, the results may show significant errors in tropospheric concentrations. It has to be mentioned that tropospheric ozone information can be retrieved from IR measurements like Aura-TES with high spatial resolution but very limited spatial coverage [102].

In this Chapter we discuss a novel direct methodology based on Neural NN algorithms and using only nadir UV/VIS measurements for the retrieval of the ozone contents in troposphere, e.g. by inferring the total TOC. NNs are particularly suited to solve complex nonlinear problems like the inversion of satellite radiance measurements for the atmospheric profiles retrieval [103]. Experience on ERS-2 GOME demonstrated the suitability of NN schemes as an alternative method to obtain ozone information with less time and computational efforts, and without the need of any a priori or climatological data [62–64, 104–106] (e.g. as intended for OE, i.e. in terms of a priori profiles and covariances matrices). In addition the NNs can be less sensitive to (wavelength dependent or not) radiometric calibration errors and don't need a forward model, as the OE, which can bring model errors and can be of difficult operations in cloudy scenarios or with significant aerosols burdens. The algorithm has been tailored on the SCIAMACHY instrument. The instrument channels 1 to 4 have been considered for our purposes. The operating wavelengths and spectral resolution of these measurement channels are: Channel 1, spectral range 240-314 nm, spectral resolution 0.24 nm; channel 2, spectral range 309-405 nm, spectral resolution 0.26 nm; channel 3, spectral range 394-620 nm, spectral resolution 0.44 nm; channel 4, spectral range 604-805 nm, spectral resolution 0.48 nm. In our work we considered only measurements in nadir mode.

The development and optimization of our algorithm has been based on a sensitivity analysis of the measurements to tropospheric ozone variations carried out by simulations of SCIAMACHY measurements (see Sec. (4.2)). Afterwards, the relative importance of the UV/VIS bands in this context has been analyzed and the spectral information budget has been explored by means of a combined radiative transfer model-neural network feature extraction methodology (see Sec. (4.2.3.1)). Finally a neural network algorithm for the inversion of the Earth's radiance spectra measured by SCIAMACHY has been designed. Its performance has been tested at mid-latitudes with a set of experimental SCIAMACHY UV/VIS data (see Sec. (4.3)), and the results are critically discussed.

4.2 Analysis of the Sensitivity of Satellite Measurements to Tropospheric Ozone Variations

To investigate the possibility and limits of inferring tropospheric ozone variations from satellite data, and to preliminarily assess the information budget in the UV/VIS SCIAMACHY observations, we analyzed the variations in Earth's radiance resulting from changes of ozone concentration at different tropospheric heights. We used the UVSPEC radiative transfer model and the LibRadtran [107] libraries to simulate backscattered radiances observed by SCIAMACHY for a mid-latitude summer urban environment. As

for atmospheric state, we used Air Force Geophysics Laboratory (AFGL) mid-latitudes climatological standard profiles of air density, pressure and temperature, and ozone, oxygen, water vapor, carbon dioxide and nitrogen dioxide [3]. These profiles are defined at 1 km thick layers in the troposphere. Aerosols optical properties and distribution were set as in a standard state, and the absorption lines of the active species were modeled by a Correlated K band parametrization [108]. The solar spectrum was chosen to a resolution of 0.05 nm (*ATLAS PLUS MODTRAN* spectrum in the LibRadtran) and then interpolated at the operating wavelengths of SCIAMACHY in the interval 220-800 nm. The solar zenith angle (SZA) has been set at the fixed value of 30° (mean value of SZA at Rome, Italy, overpass, taken as a reference), and the observation has been assumed at nadir. Our simulation is based on the following steps: a) the model was forced to solve the radiative transfer equation at the operating SCIAMACHY wavelengths, b) a Gaussian slit function with a FWHM = 0.3 nm was imposed to simulate the sensor's spectral resolution, and 3) a 1% Gaussian noise was added to the modeled radiances. For this latter assumption, some considerations must be done. As well known, the knowledge of measurement errors is very critical for retrieval purposes. In the UV/VIS the signal varies by several orders of magnitude, so the measurement error vary strongly with wavelength. The random noise error in SCIAMACHY data can vary from about 10% at about 290 nm to about 0.1% at about 330 nm. A sensitivity of 0.2% at wavelengths with 0.1% noise levels will provide much more information than 1% sensitivity at wavelengths with 10% noise levels. So the assumption of a fixed 1% noise error is just a provisional approach and an enhanced sensitivity analysis will be considered in the future to improve the methodology. A more complete sensitivity analysis may consider measurement error estimates varying with wavelengths (e.g., random noise error estimate in the SCIAMACHY level 1b data). The ozone concentrations were systematically enhanced in the tropospheric layers (0-14 km in our case, as the tropopause was set at 14-17 km) and the changes in backscattered UV/VIS spectra were analyzed. Fig. (4.1) shows the differences (%) of Earth's radiance in the spectral range 220-800 nm, for a doubling of ozone at 14 km with respect to the standard case. Fig. (4.2) shows the same differences (%) when doubling the ozone concentrations in layers centered at different heights below 14 km. To more clearly display the obtained patterns, the Gaussian noise has not been considered here.

Even though the maximum sensitivity is in the range 302-307 nm, some sensitivity is also apparent in the VIS range, mostly around the interval 550-650 nm, in the Chappuis bands. Here the spectral range with nonnegligible sensitivity is wider, although the sensitivity weaker.

To quantitatively assess the overall tropospheric information budget, we performed an integration of the mentioned radiance differences over the sensible UV and VIS spectral

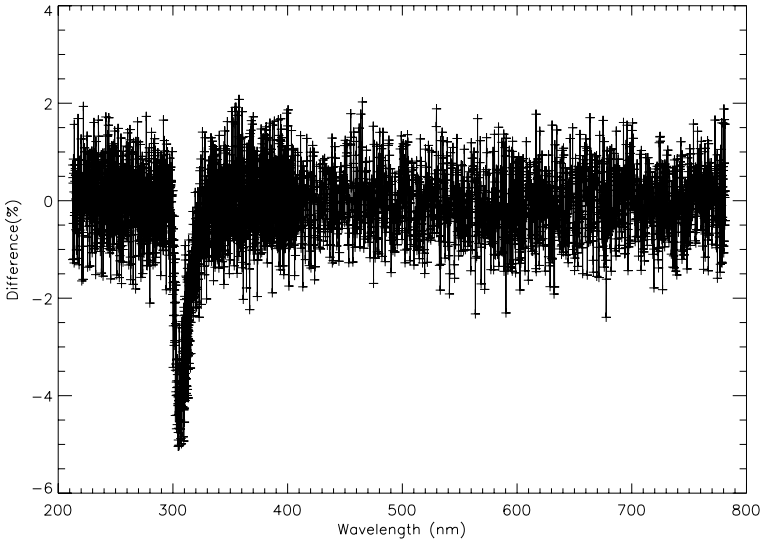

FIGURE 4.1: Spectral differences (%) of Earth's radiance for a doubling of ozone concentration at z=14 km with respect to AFGL mid-latitude standard, with noise. Please refer to the text for the model settings.

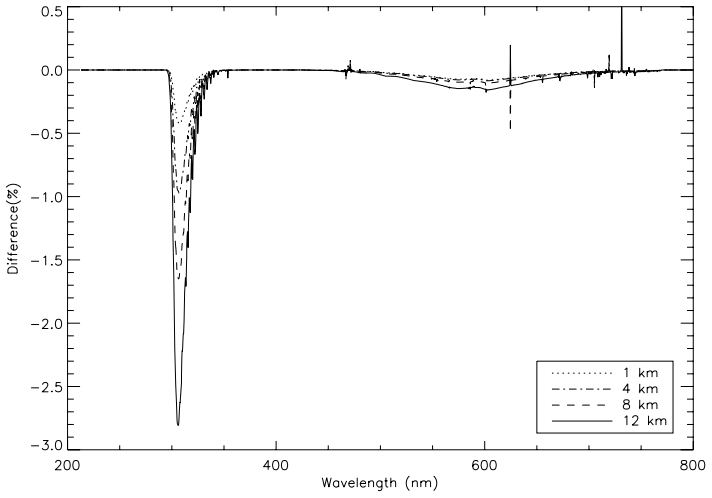

FIGURE 4.2: Spectral differences (%) of Earth's radiance for a doubling of ozone concentration at z=1, 4, 8, 12 km with respect to AFGL mid-latitude standard, without noise. Please refer to the text for the model settings.

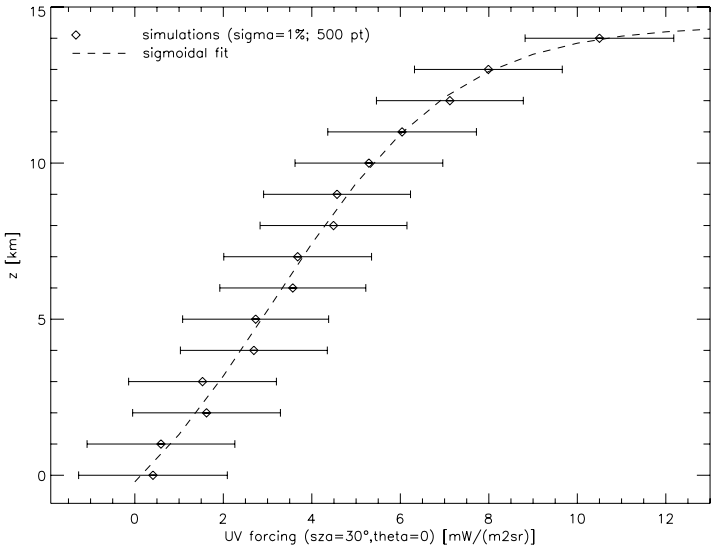

FIGURE 4.3: UV radiative forcing vs. height at a fixed observation angle (SZA=30°, $\vartheta = 0$) for ozone doubling. A sigmoidal fitting function is shown. Each point represents the mean value and the bar is the standard deviation of a set of 500 spectral simulations; each simulation includes a 1% level Gaussian noise.

intervals resulting from the enhancements at each considered layer, and calculated the UV and VIS radiative forcings due to ozone doubling at a fixed observation angle. The trends of these quantities are reported in Fig.s (4.3) and (4.4). Fig. (4.3) also shows the fitting of the UV forcing with a sigmoidal function (five parameters); it seems to approximate the vertical trend with a good accuracy ($R^2 = 0.99$). Both Fig.s refer to the previously mentioned noise level $\sigma = 1\%$; annotations on the graphs also show the number of modeled spectra for each height level.

Although the dispersion is considerable, VIS forcings, i.e. the VIS tropospheric ozone information budget, look significant. Hence, the sensitivity in the Chappuis ozone bands seems exploitable, in combination with the UV information, to retrieve tropospheric ozone information from satellite data, provided the surface albedo is known with sufficient accuracy. In general a systematic evaluation of the spectral response of surface and aerosols, as well as the variation of solar zenith angles, should be considered be and will be explored in the future.

An interesting parameter is the ratio of the UV and VIS forcings mentioned above. Fig. (4.5) shows the variation with height of this quantity for our simulations. The UV/VIS forcing ratio has a linearly increasing trend in the first height levels, and then it does not vary much with altitude above 8 km. This simulated parameter exhibits an appreciable sensitivity to the ozone concentration vertical variations in the lower tropospheric levels, though uncertainty is large.

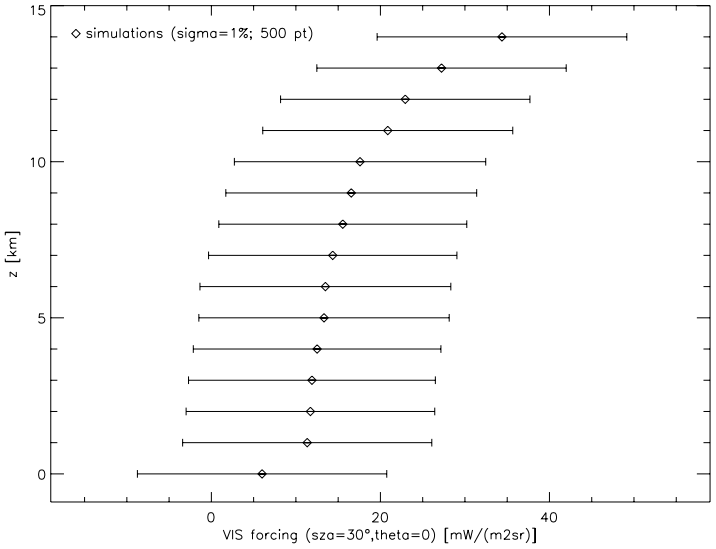

FIGURE 4.4: VIS radiative forcing vs. height at a fixed observation angle (SZA=30°, $\vartheta = 0$) for ozone doubling. Each point represents the mean value and the bar is the standard deviation of a set of 500 spectral simulations; each simulation includes a 1% level Gaussian noise.

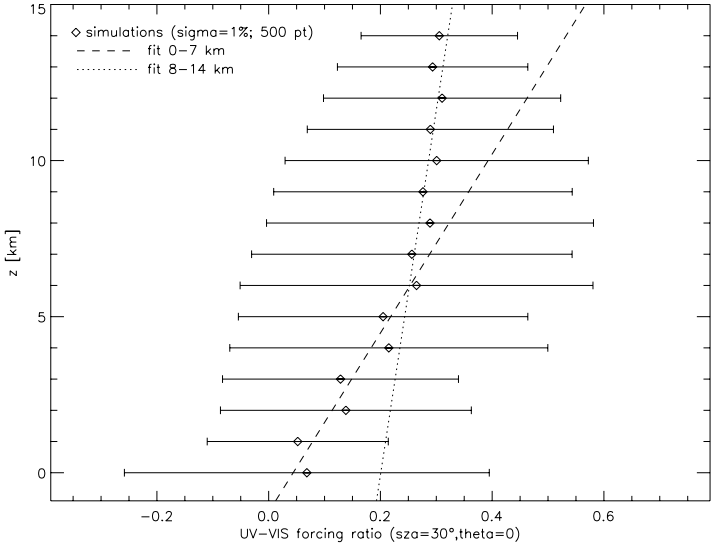

FIGURE 4.5: UV/VIS forcing ratio vs. height at a fixed observation angle (SZA=30°, $\vartheta = 0$) for ozone doubling. Each point represents the mean value and the bar is the standard deviation of a set of 500 spectral simulations; each simulation includes a 1% level Gaussian noise. Two different straight lines for the ranges 0-7 km and 8-14 km are shown.

The results of our simulation suggest that: a) although the sensitivity of the Earth's radiance spectra to tropospheric ozone variations is low, especially in the lower layers and the expected standard deviations are large, the retrieval of height resolved information on tropospheric ozone seems still feasible, and b) measurements in the VIS range carry useful information. The preceding feasibility analysis hints at a demanding retrieval problem. An inversion algorithm sufficiently robust and carefully designed is essential to the successful exploitation of the scant information contained in the measurements. NNs are known to handle non-linear and weak relations between physical quantities. To this end, the topology of the net, the various parameters controlling its behavior and the training procedure must be carefully determined to optimize its performance. The design of the net includes, as an essential element, the selection of the wavelengths contributing independent pieces of information. This selection has been carried out based on a combination of a radiative transfer model and neural network extended pruning (RTM-NN EP) aimed at singling out the measurements at the wavelengths contributing information rather than noise, as it will be described in the following. Our RTM-NN EP procedure led to the definition of the input vector of our UV/VIS net.

4.2.1 Dataset Generation

Starting from the AFGL mid-latitude standard atmosphere, we changed the ozone concentration profile to produce a large database for training the net. We generated 4000 ozone profiles and we computed the corresponding Earth's radiance by means of the UVSPEC model set as described in the previous section. The total ozone was varied between 350 and 250 DU. For a subset of the profiles, an additional contribution modeled by an exponential function to simulate production of ozone at ground with some vertical transport has been considered. These profiles have been assumed as in Eq. (4.1).

$$O_3'(z) = O_3(z) + A \cdot O_3(z) \cdot e^{-\frac{z}{H}} \tag{4.1}$$

Parameter A was varied from 0 to 4 and H was varied from 1 to 5 km. A random fluctuation with Gaussian distribution of mean value 0 and standard deviation 0.3 has been added to both A and H, for each profile. All profiles were also modified by adding a random fluctuation with Gaussian distribution of mean value 0 and standard deviation equal to 50% of the concentration at each height. The procedure provided a database of synthetic profiles and spectra, aiming at simulating photochemical induced ozone generation in mid-latitude summer urban environments. It has to be noticed that this dataset generation doesn't attempt to model specific pollution phenomena with a given

TABLE 4.1: Selected wavelengths for UV TCO NN input vectors.

UV1 band	UV2 band
305.739 nm, 305.849 nm, 305.960 nm	322.051 nm, 322.163 nm, 322.275 nm
306.070 nm, 306.180 nm, 306.290 nm	322.387 nm, 322.500 nm, 322.612 nm
306.401 nm, 306.511 nm, 306.621 nm	322.724 nm, 323.397 nm, 323.509 nm
306.731 nm, 306.842 nm	323.612 nm, 323.733 nm, 323.845 nm
	323.957 nm, 324.069 nm, 324.181 nm
	324.293 nm

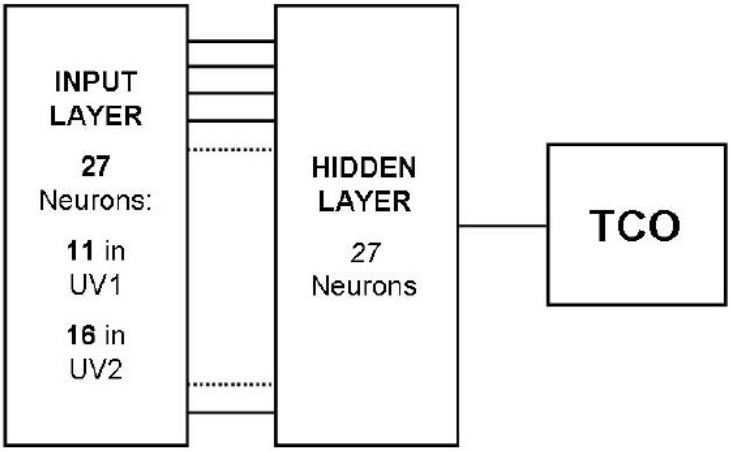

FIGURE 4.6: TOC NNs scheme.

accuracy but is intended only to provide an extended set of ozone concentration profiles to tailor the NNs.

4.2.2 Neural Net Inversion of UV Radiances

For the time being, our purpose is the Tropospheric Ozone Column (TOC) retrieval. As a first step in the design, we consider only measurements in the UV range, selected on the basis of physical considerations and of the results of the sensitivity study in Sec. (4.2). Tab. (4.1) lists the chosen wavelengths.

Two ranges were selected: 305.75-306.85 nm (UV1) and 322.05-324.30 nm (UV2). Both bands are in the range in which the analysis of Sec. (4.2) suggested sensitivity; in particular, the NN UV1 band is in the interval of maximum sensitivity (see Fig. (4.1)).

We chose the dimensionality of the hidden layer by monitoring the retrieval error as a function of the number of hidden neurons. We obtained the minimum error for 27 hidden neurons. A scheme of the used UV NN is in Fig. (4.6).

A crucial point of NNs design is the scaling of the input and output vectors to fit the optimal dynamic interval of the neurons. In our case the radiance values vary over one

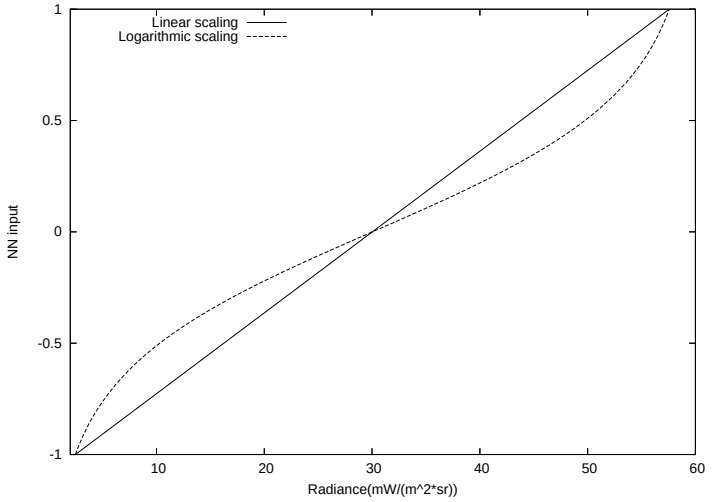

FIGURE 4.7: Scaling function of the input training vector in TCO dedicated UV NN. Overlapped a linear scaling function is reported to underline the larger slope of our scaling function near the boundaries of the selected radiance interval.

order of magnitude from UV1 to UV2. The neurons acceptance interval is set in the range from -1 to 1. For a more uniform exploitation of the spectral information, we performed a nonlinear scaling of the input vectors, using Eq. (4.2).

$$NN_{\text{input}}(\text{RADIANCE}) = b \cdot \ln\left(-\frac{a}{\text{RADIANCE}} - 1\right) \tag{4.2}$$

with a and b to be searched to fit the radiance values of the training dataset with the mentioned NN_{input} acceptance interval. Fig. (4.7) shows the used function for the chosen dataset with the superposed linear scaling. It can be noticed that there is a very large dynamic range in the two regions of interest (near 0 for UV1 and near 55-60 mW/(m^{2}sr) for UV2), so that the signal both in UV1 and in UV2 bands can be better exploited. In fact, this scaling procedure yielded more accurate results than the commonly adopted linear scaling.

The overall dataset has been split into two ensembles: the training and the test dataset, consisting of 3000 and 1000 patterns, respectively. The output of our net is the TCO value, i.e. the ozone concentration of our synthetic profiles integrated over the range 0-14 km, linearly scaled in the range from 0 to 1. The simulated spectra have been inverted with a 1% additive random fluctuations in the radiance values, modeling noisy measurements.

Fig. (4.8) reports the scatterplot of the retrieved vs. the "true" values, i.e., those assumed in the independent test subset.

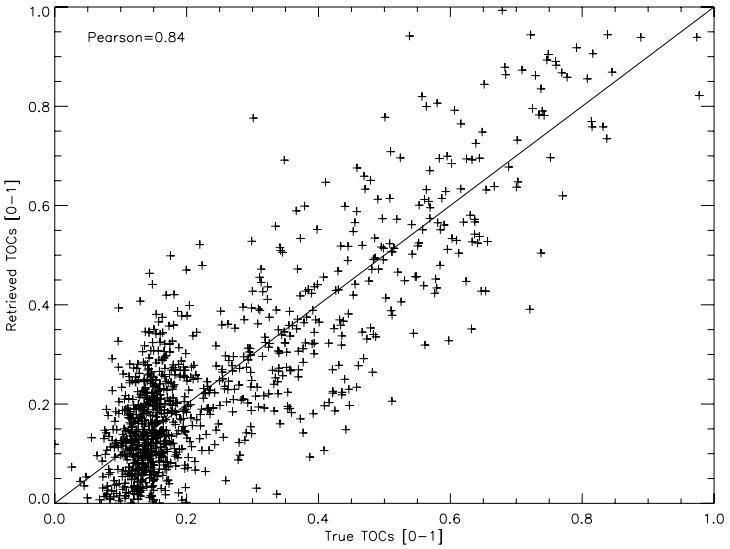

FIGURE 4.8: Retrieved normalized TOCs vs. "true" noisy simulated data, for UV-only measurements. Pearson coefficient value is reported.

The Pearson correlation coefficient, equal to 0.84, indicates that the information on the TOC has been retrieved, although with a considerable dispersion due to the relatively low sensitivity of the Earth's radiation to tropospheric ozone.

4.2.3 Neural Net Inversion of UV-VIS Radiances

4.2.3.1 Wavelength Selection by Combined RTM-NN EP Procedure

The analysis reported in Sec. (4.2) points out that also measurements in the visible spectral range can contribute useful information on tropospheric ozone. However, the addition of further input data could worsen the conditioning of the inverse problem, since the additional measurements, being only partially independent, might contribute more noise than useful information [88]. A careful selection of the measurement wavelengths must be carried out within our UV/VIS enlarged set of data to exploit the maximum of potentially available information while keeping the effect of ill-conditioning under control. To this end, we followed the Extended Pruning (EP) procedure, which at the same time selects the input measurements set and yields the optimal NN topology. We applied this technique to selected bands of the SCIAMACHY with the intent of providing some hint on the potential of this instrument in monitoring tropospheric ozone. We considered the dataset of Sec. (4.2.1), that is the set of 4000 spectra-TOC pairs. As said, the TOC is the ozone concentration integrated over the range 0-14 km. For each atmospheric profile, i.e. for each TOC, the input spectra consisted of about 2000 radiances computed at wavelengths in the ranges of about 290-340 nm, 400-410 nm,

450-720 nm and 790-800 nm. Note that we considered also the low-sensitivity bands for the sake of completeness of the analysis. To reduce the computational time and effort, we did not consider the whole UV/VIS range but we discarded a large part of the low-sensitivity ranges as resulted from Sec. (4.2). The starting neural network, with as many input neurons as the selected wavelengths, had an hidden layer of the same dimension, and a mono-dimensional output layer yielding the TOC value.

We first trained the net until the mean square error of the retrieved values vs. the "true" values didn't vary when the net was trained further on. An early stopping criterion was applied. Then we started the pruning procedure based on the following iterative steps:

1. the synapsis with the lowest weight is pruned;
2. the net is re-trained for a limited number (10% of the first training cycles) of cycles without re-initialization;
3. the mean square error MSE is re-calculated and the pruning is stopped if MSE>MSE_{max}, where MSE_{max} is a threshold to control the EP performance.

An input is pruned when all its connections are removed. This indicates that no useful information is carried by that measurement, while the remaining wavelengths contribute to the retrieval. Fig.s (4.9(a)) , (4.9(b)) and (4.9(c)) show the density of the surviving wavelengths after 10000, 40000 pruning steps and at the end of the whole procedure (about 90000 steps). Some interesting features emerge. The measurements in the low-sensitivity 400-410 nm and 790-800 nm bands are eliminated first. The inputs at wavelengths in the region 307-322 nm are then quickly pruned and their density becomes quite low even after a few pruning steps. At the end, the higher density can be found in the range 298-307 nm, whose relative importance became more and more pronounced as the pruning went on; this band also showed the maximum sensitivity in the analysis of Sec. (4.2). The range 322-340 nm is second in importance; it can be noticed that this band contains the whole required wavelengths range for the GOME NN described by [62]. The density of wavelengths in the visible follows the structure of the Chappuis band and is in agreement with the results of Sec. (4.2), with a maximum density of information in the 550-650 nm range.

At the end of the overall EP procedure, we have 28 input measurements left contributing to the retrieval (Tab. (4.2)).

The topology of the net adapted according to the pruning process, strongly reducing the number of neurons and of the connections. The scheme of the obtained net is reported in Fig. (4.10).

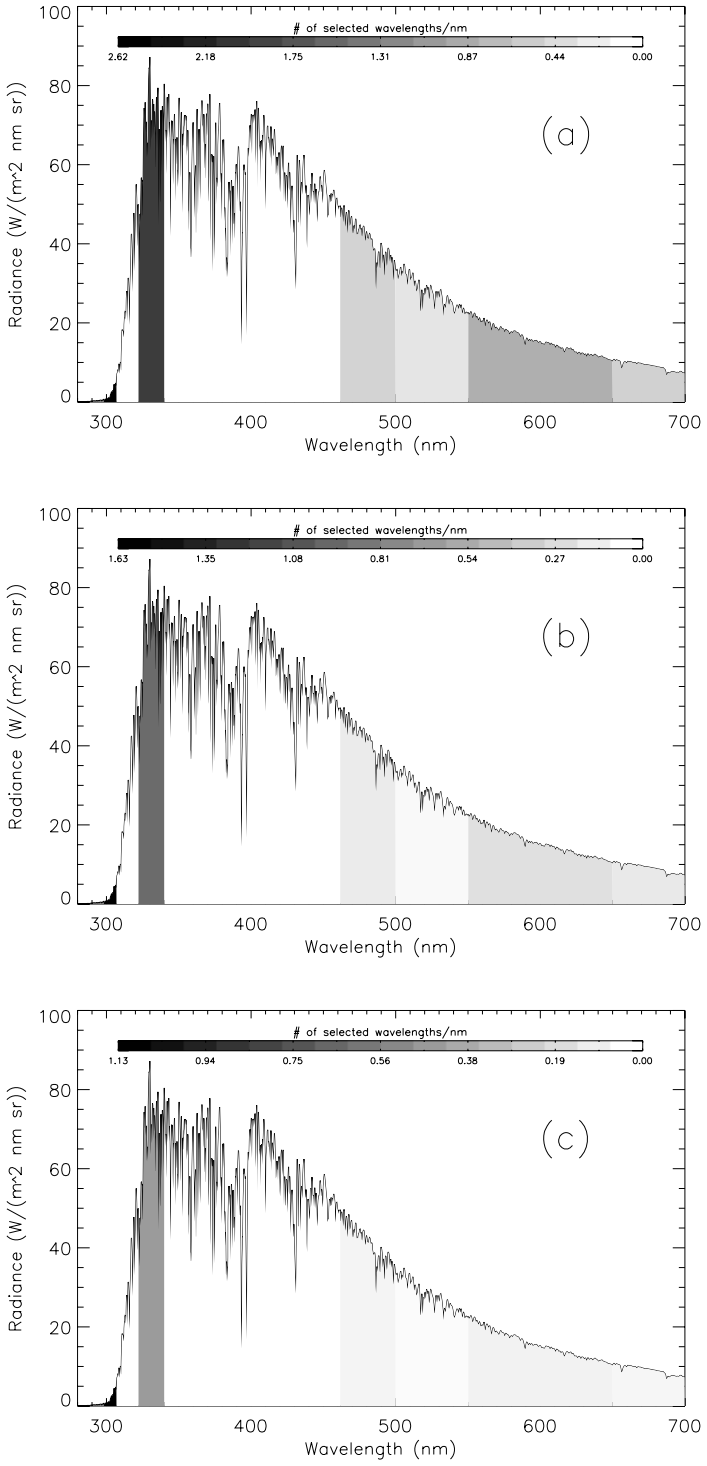

FIGURE 4.9: Density of the selected wavelengths after 10000 (a), 40000 (b) pruning steps and at the end (about 90000 steps) of the whole procedure (c). The gray scale represents the density at some selected ranges, i.e. the number of useful measurement wavelengths per nm. A standard Earth's radiance spectrum calculated by means to the UVSPEC code is overlapped.

TABLE 4.2: Final wavelength selection for UV/VIS TCO NN input vectors.

UV band	VIS band
298.694 nm, 300.944 nm, 301.444 nm	482.185 nm, 484.302 nm, 546.912 nm
301.664 nm, 302.765 nm, 305.188 nm	571.949 nm, 615.398 nm, 619.799 nm
306.180 nm, 306.401 nm, 306.731 nm	629.636 nm, 635.713 nm, 648.204 nm
323.509 nm, 324.181 nm, 324.628 nm	652.696 nm, 664.181 nm
325.969 nm, 327.528 nm, 327.973 nm	
334.144 nm, 335.377 nm	

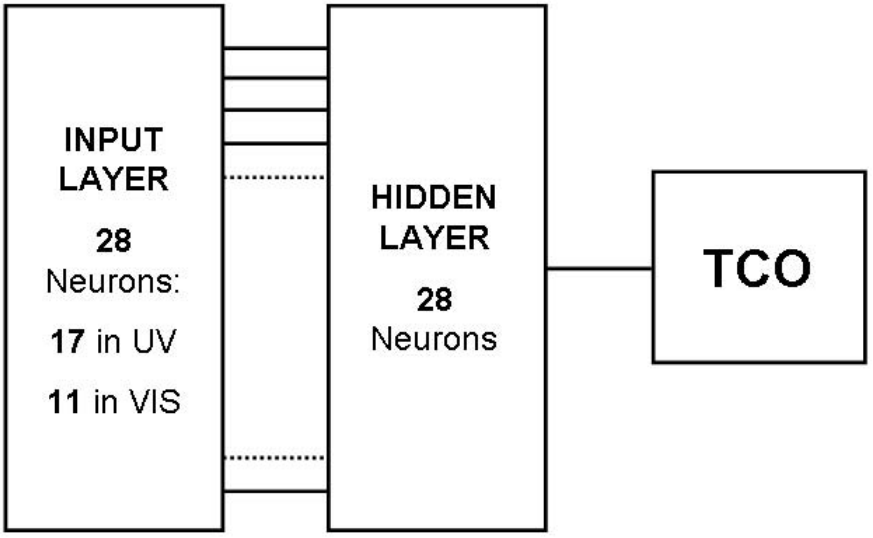

FIGURE 4.10: UV/VIS TOC NN scheme. The subdivision of the UV and VIS input bands are indicated.

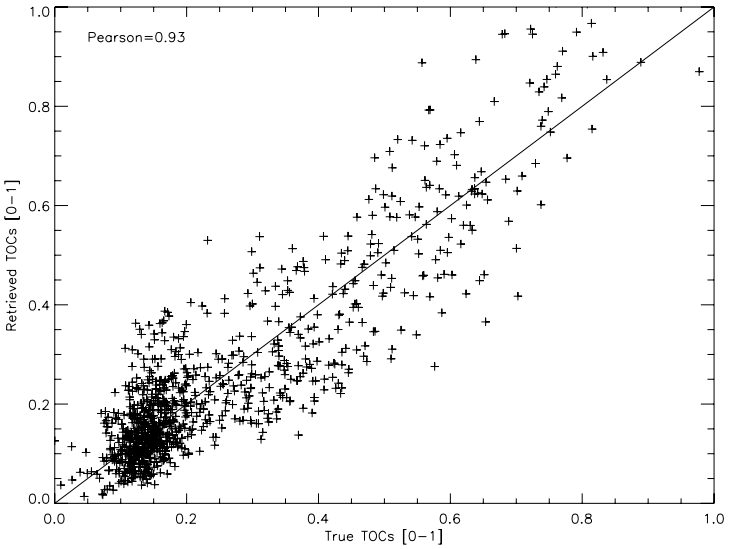

FIGURE 4.11: Retrieved normalized TOCs vs "true" noisy simulated data, for UV/VIS input measurements. Pearson coefficient value is reported.

The final NN showed a better retrieval performance, increasing of more than 10% the correlation coefficient of the retrieved TOCs with respect to UV-only case. In Fig. (4.11) we report the scatterplot of the retrieved TOCs vs "true" data for the independent test set consisting of 1000 input-output pairs.

4.3 A Case Study With Experimental SCIAMACHY UV/VIS Data

4.3.1 Dataset Generation

We validated the neural network algorithm optimally designed as described above in the inversion of a set of actual SCIAMACHY Level 1b data. Satellite data were matched with ozonesondes measurements extracted from the WOUDC [26] database.

The net has been trained and tested with measurements at selected locations with latitudes between 30°N and 60°N, i.e., approximately the northern mid-latitudes. A careful inspection of the tropospheric ozone variability in a global dataset (the mentioned WOUDC data and the available data from the SHADOZ [20, 27]) led us to a selection criteria to match the satellite and ozonesondes data. Indeed, the standard deviation of the ozonesonde-derived concentrations generally shows a minimum at the equator and a maximum at the poles. Following this consideration, in [106] a cosinusoidal relationship between matching distance and latitude was assumed, and GOME and ground based lidar measurements were considered as co-located when the GOME ground pixel center

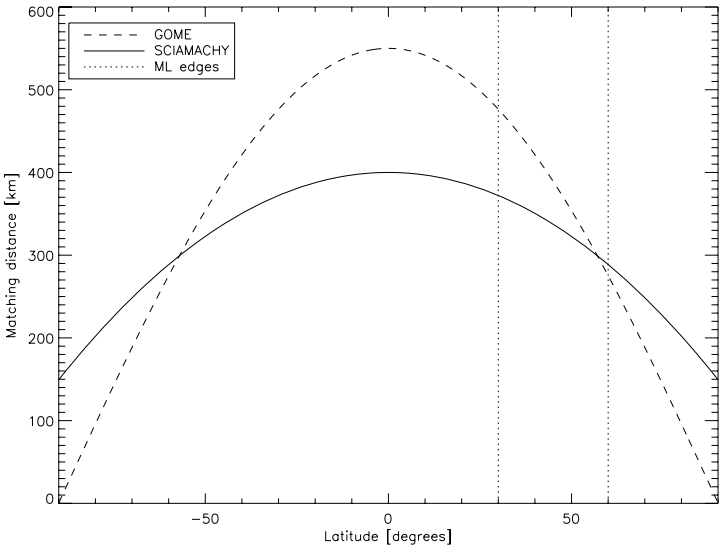

FIGURE 4.12: Matching distance vs. latitude of SCIAMACHY measurements vs. ozonesondes stations (solid line) and GOME measurements vs lidar stations as described by [106] (dashed line). The vertical lines identify the 30°N-60°N latitude range.

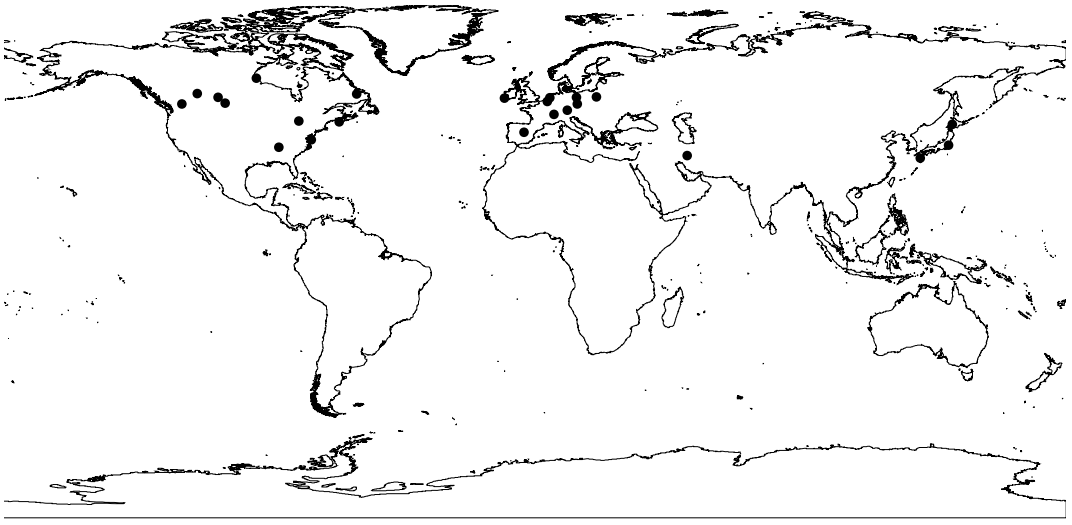

FIGURE 4.13: Map of the matching points between mid-latitude ozonesondes stations and SCIAMACHY overpasses.

was within ±2.5° in latitude and ±5.0° in longitude from the lidar station. In the mid-latitudes region of interest, we adopted a matching distance criterium stricter than the one adopted for GOME by [106]. The dependence of the matching distance with latitude is shown in Fig. (4.12) for SCIAMACHY and, for comparison, for GOME. The matching distance has been assumed independent of longitude, and data have been considered temporally matching if taken within a 12 h time interval. Fig. (4.13) shows the ozonesonde sites in which we found at least one matching satellite overpass.

In this way we obtained over 4000 input-output vector pairs. We normalized the satellite

measurements with respect to the solar spectrum to single out the atmospheric contribution, then the concentrations measured by the ozonesondes were integrated over the range 0-14 km to obtain the TOC. We assumed the tropopause starting at 14 km, according to the AFGL mid-latitude standard climatology.

4.3.2 Results

Independent subsets of the mid-latitude data were used to train and test the net; about the 75% of the dataset is used for training and the remaining part for testing. The algorithm was validated on a further independent subset consisting on data overpass Uccle, Belgium (50.8°N-4.4°E) and De Bilt, the Nederlands (52.1°N-5.2°E). These two stations have been considered together because their distance is lower than the matching distance discussed previously. The time series of the NN-retrieved TOC and corresponding ozonesondes TOCs in a time window of over a year is reported in figure 4.14. Although a systematic underestimation is clearly visible, the trend is well reproduced by our NN retrievals. Underestimations may be due to the larger airmasses sounded by the satellite. Indeed, the Uccle/Debilt area is in a relatively polluted urban environment [109], hence the localized ozonesondes measurements are probably affected by high local pollutant concentrations. In any case, a further analysis for the interpretation of the observed biases, that can reach values as high as 30%, is necessary, and will be considered in the future. In addition it is worth to be mentioned that a thorough validation, e.g. based on several stations in polluted/clean areas, is still to be achieved and will be considered to complete this work.

4.4 Summary and Conclusion

Satellite observation of tropospheric ozone is a powerful tool for environmental monitoring both at regional and at global scale. We designed a neural network algorithm for estimating the TOC from nadir UV/VIS Earth's radiance spectra measured by the ESA-Envisat SCIAMACHY sensor. A combined radiative transfer model-neural network extended pruning sensitivity analysis has been implemented to design the optimal input layer in terms of spectral information. The role of the VIS radiation in the Chappuis ozone bands has been investigated and critically discussed. Indications were gained on the importance of the VIS band in tropospheric ozone sounding: the retrieval accuracy, in terms of the Pearson coefficient for a test set of 1000 simulated input-output vectors pairs, improved of over 10% with respect to UV-only input. The designed algorithm, trained by WOUDC ozonesondes data, was provisionally validated with SCIAMACHY measurements over a mid-latitude site. The retrieved TOCs reproduced the time trend

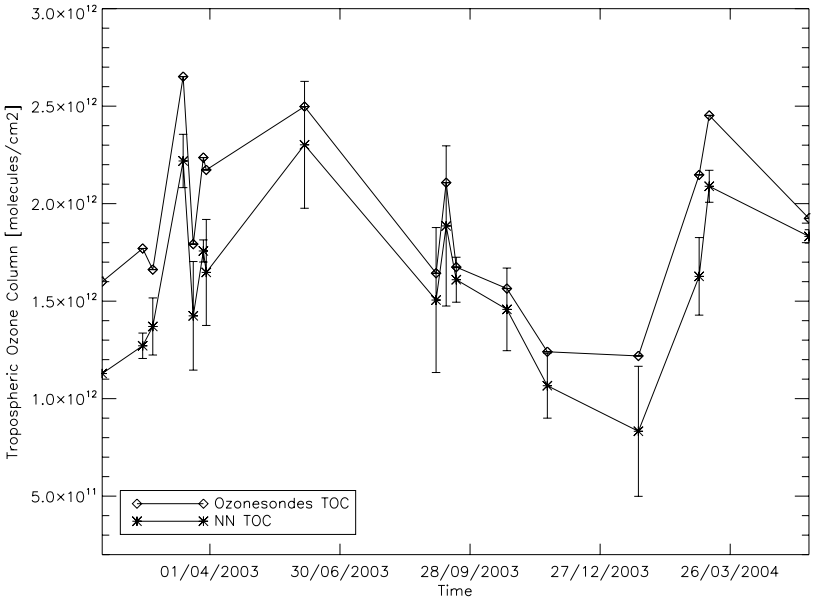

FIGURE 4.14: Time series of the retrieved (asterisks with errorbars) and simultaneous reference ozonesondes TOCs (diamonds) at Uccle and Debilt stations, in the period january 2003-may 2004.

of the in situ data, though a systematic underestimation appears to occur, probably related to a local effect. This result has been obtained for a single particular location. Nevertheless, it looks encouraging towards the effective exploitation of satellite measurements for monitoring ozone in the troposphere.

Pasquale Sellitto: sellitto@disp.uniroma2.it

Chapter 5

NNs for ozone profile retrieval from nadir UV/VIS SCIAMACHY data

Part of this Chapter's contents is extracted from the publications: [110–112].
This activity is performed in the context of ESA Cat-1 project no. 2930.

5.1 Introduction

The derivation of height resolved information on atmospheric parameters from satellite remote sensing instruments plays a key-role in monitoring the Earth's atmosphere and understanding the chemical and physical processes therein. However, the atmospheric structure and trace gases concentrations result from a complex interaction between radiative, physical and chemical processes. In this context, a typical problem is related to the difficulty of inverting the measured radiance data to obtain height resolved information on ozone concentration (see Chapter (2)). The most widely used methods to obtain ozone concentration profiles from nadir satellite data are based on OE schemes, that involve the use of a direct radiative transfer code and some a priori information. NNs emerged in the last years as an alternative useful tool to face with such complexities. Owing to the fact that NNs algorithms can approximate nonlinear functions, it can be assumed that they are suitable for nonlinear problems like those related to the transfer of radiation in atmosphere. Moreover, once trained, NNs allow ozone profiles retrievals in a very short computational time, and they're less sensitive to calibration uncertainties. Several works have demonstrated the effectiveness and reliability of NN-based inversion algorithms for ozone retrieval from satellite data, see, e.g., [62, 63].

In this Chapter we present the results of our NNs algorithm application to EnviSat-SCIAMACHY Level 1b data to infer ozone concentration profiles. In Sec. (5.2) we will discuss the dataset preparation for the training and test phases. We have trained the Nets with a significant set of input-output pairs; the radiance at the selected wavelengths in UV/VIS bands (input data), extracted from SCIAMACHY Level 1b data, have been pre-processed and matched with collocated WOUDC and SHADOZ ozonesonde height resolved concentrations (output data). Sec. (5.3) will present the several algorithms design issues. In Sec. (5.4), reporting the results of this algorithm, we'll show a comparison exercise of the retrieved ozone concentrations with independent ozonesonde datasets and with ERS2-GOME simultaneous vertical ozone profile retrievals [62, 104]. The intercomparison results are analyzed and critically discussed.

5.2 Training and test sets generation

We decided to train our nets exclusively with ozonesondes data. This choice has been made to train the algorithm with profiles characterized by high vertical and horizontal resolutions; however this restricts the height interval of our retrievals. We used WOUDC/SHADOZ ozonesondes datasets. We first analyzed data distribution and variabilities to optimize SCIAMACHY vs ozonesondes dataset preparation. We found that a good choice for the height interval to be considered was the range 1000.0-6.5 hPa. Indeed this allowed the maximum extension of the dataset in the period 2002-2006. By fixing these maximum/minimum values we found a sensible downward trend of available WOUDC and SHADOZ profiles, as depicted in Fig. (5.1). The geographical distribution of the active and reliable public ozonesondes stations in the period 2002-2006 is depicted in Fig. (5.2); the number of available measurements versus latitude is reported in Fig. (5.3). As clear in the picture, we found a much higher density of ozonesondes data in the northern mid-latitude than in every other part of the globe. Starting from these data distributions, we performed a time-space matching of ozonesondes and SCIAMACHY spectra, obtaining about 11000 input-output pairs.

The obtained dataset has been split into a training (about 80% of the matchings) and a test independent subset. We considered first only UV radiance as input; afterwards we also tried to add VIS data in the Chappuis band. The results of these NNs configurations are reported in Sec. (5.4).

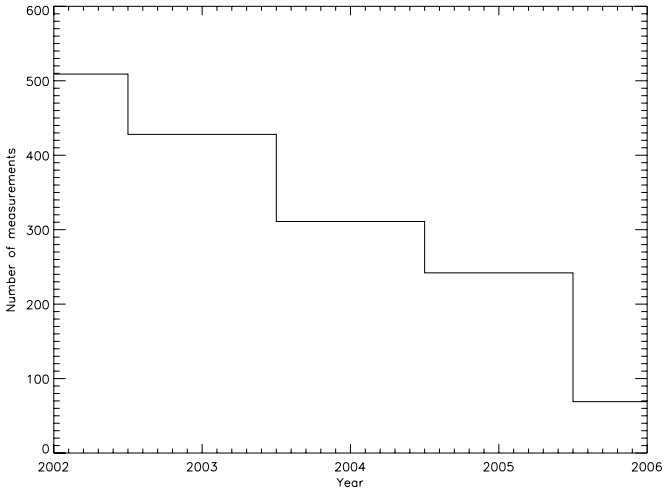

FIGURE 5.1: Trend of available ozonesondes profile measurements in the interval 2002-2006.

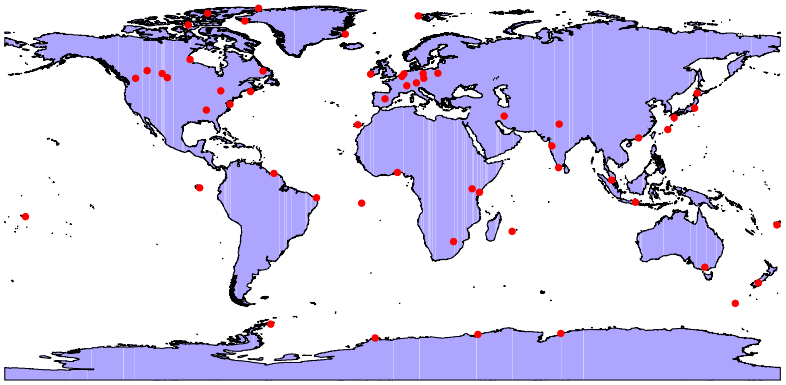

FIGURE 5.2: WOUDC and SHADOZ active ozonesonde stations (red circles) in the period 2002-2006. Only stations with at least one measurement in the complete range 1000.0-6.5 hPa have been considered.

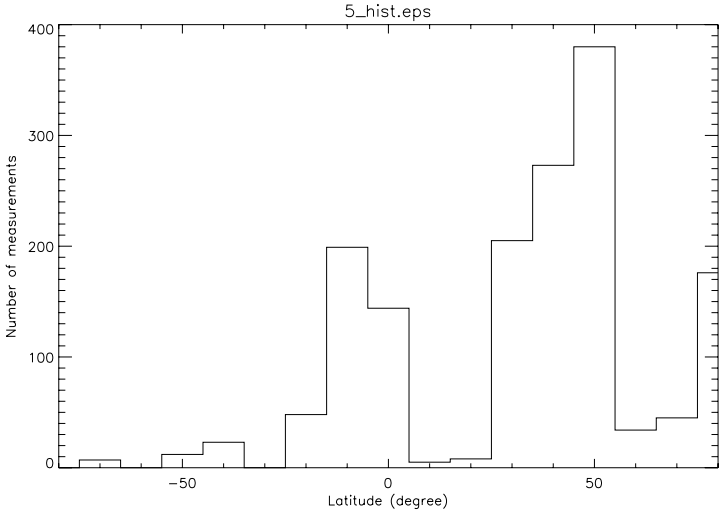

FIGURE 5.3: Number of available ozonesondes measurements versus latitude.

5.3 Algorithm optimization

The first step in the design of our algorithm is the reduction of the input vector by means of a NN-based EP procedure. In fact, as discussed in Chapter 4, the overall UV/VIS reflectance spectra consist of hundreds of wavelengths, and this high number of inputs and the resulting complex topology is expected to worsen the performance of the net, which can loose its generalization capabilities. Thus a reduction of the input vector dimensionality is of crucial importance. Here we recall the EP procedure. Please cf. [104] or Chapter 4 for a more elaborated discussion of EP. We first trained the Net for several hundreds of learning cycles. Then we started the pruning procedure by applying the following iterative steps: 1) the weakest synapse is pruned; 2) the net is re-trained without re-initialization; 3) the error E is calculated and the pruning is stopped if $E > E_{max}$. An input neuron is eliminated when all its connections are pruned. We used part of the dataset to this aim. After several thousands of pruning iterations we obtained 19 input wavelengths, mainly in the range 300.0-325.0 nm.

Afterwards we studied the optimal net's topology for our purposes. We investigated the number of hidden layers and the numbers on neurons in a layer. We found that the best performance is obtained with 1 hidden layer containing 29 neurons. Finally, the selected topology was 19-29-9.

5.4 Results

We trained and tested the net with the remaining input-output pairs in the SCIAMACHY-ozonesondes database. It has to be noted that the test set was independent from the training one, i.e. data were taken from matching over different ozonesondes stations. We applied an early stopping procedure: we stopped the training when the error on the test subset started to rise. This approach ensures generalization capabilities to the net. Fig. (5.4) shows an example of a retrieved profile compared with the corresponding measured ozonesondes target profile. As it is possible to see, the enhancement of ozone concentration in the 2 tropospheric layers, i.e. 1000.0 and 421.7 hPa, is fully detected. In general the net showed a good sensitivity in the detection of tropospheric ozone variations.

Two scatterplots of NN estimations versus ozonesondes target concentrations for the test subset is reported in Fig.s (5.5) and (5.6) for two pressure level, P=178.5 hPa and P=31.6 hPa. The Pearson correlation coefficients are 0.95 and 0.94.

We also tried to add information in the Chappuis band by the inclusion of one or more input located in SCIAMACHY band 3. In particular we have considered the signal at

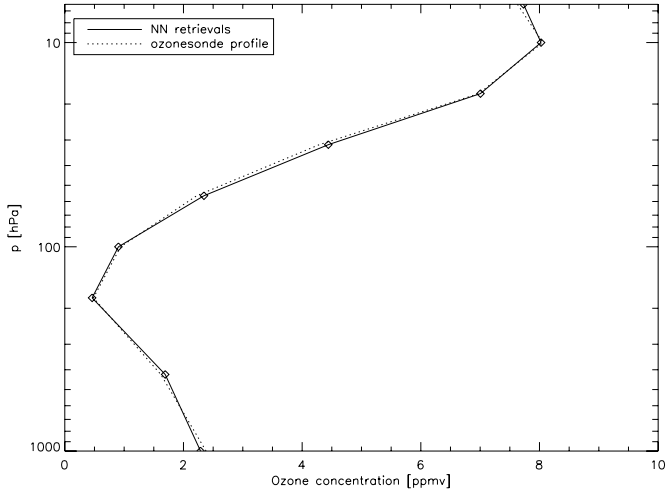

FIGURE 5.4: Example of a SCIAMACHY-NN retrieved profile (line with diamonds), with ozonesondes target profile (dotted line) as a comparison. Lat/lon = N41.92, E12.50, JD = 201/2003.

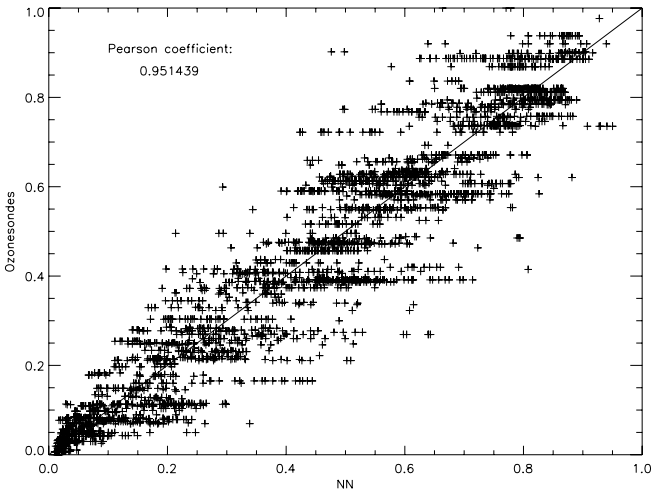

FIGURE 5.5: NN estimations vs ozonesonde data at pressure level P=178.5 hPa, for an independent ozonesondes subset. Pearson coefficient is reported.

about 572 nm, where the Chappuis yellow peak can be found. Although the use of VIS radiation in the Chappuis band seems important for the retrieval of tropospheric ozone in dedicated nets (see Chapter 4), here we did not observe a similar level of significance.

A subset of SCIAMACHY UV NN retrievals (45 days in the period January-August 2003) was compared with matching GOME UV NN concentrations, calculated with the algorithm described in [104]. The two algorithms use the same input-output dimensionality and definition. Fig. (5.7) shows the RMS of GOME UV NN and SCIAMACHY UV NN ozone profile retrievals with respect to ozonesondes reference. SCIAMACHY UV NN profiles show a smaller RMS at each pressure level.

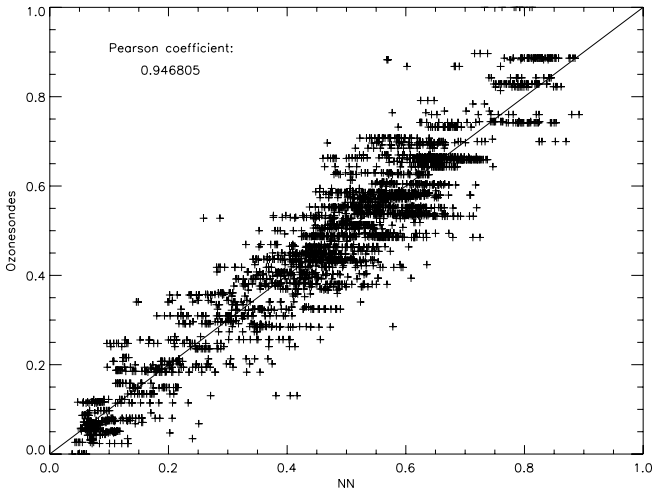

FIGURE 5.6: NN estimations vs ozonesonde data at pressure level P=31.6 hPa, for an independent ozonesondes subset. Pearson coefficient is reported.

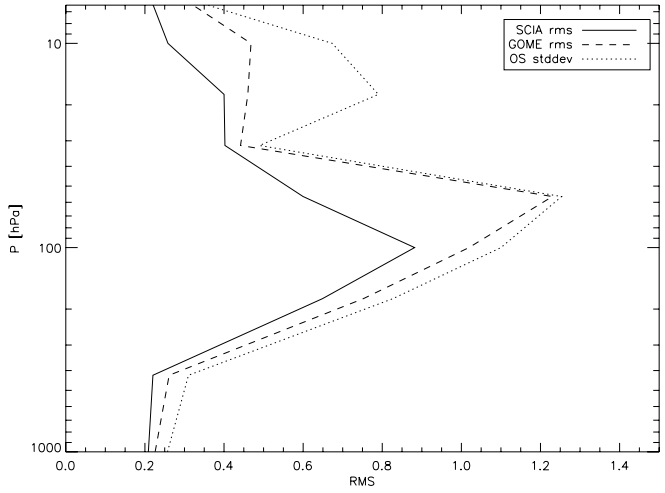

FIGURE 5.7: Height resolved RMSs for SCIAMACHY and GOME NN ozone profile retrievals, and OS standard deviations for the subset in the period Jan.-Aug. 2003 (see text for details).

5.5 Conclusion

We have reported on the development of some NNs algorithms for the retrieval of ozone concentration profiles from ESA-Envisat SCIAMACHY Level 1 measurements. We used exclusively ozonesondes data (from WOUDC and SHADOZ datasets) as *truth* reference. From analyses performed with independent ozonesondes datasets, quite encouraging results emerged. A subset of retrieved ozone profiles was compared with matching concentration profiles retrieved with a previously developed NN scheme for ESA-ERS2 GOME measurements. SCIAMACHY NN concentrations seem to be of a better quality. We also investigated on the possible improvement on the retrieval performance stemming

from the use of measurements in the VIS band, but at the moment we did not find encouraging results concerning this aspect. Further analyses on wavelengths selection and vertical resolution estimation are however ongoing, as well as a systematic validation.

Pasquale Sellitto: sellitto@disp.uniroma2.it

Chapter 6

NNs for stratospheric ozone profile retrieval from OMI data

Part of this Chapter's contents is extracted from the publications: [112].
This activity is performed in the context of ESA Cat-1 project no. 2930.

6.1 Introduction

The ozone is an atmospheric constituent of crucial importance for life in Earth's biosphere, owing to its role in screening the harming UVB and UVA solar radiation. About 90% of atmospheric ozone is in the stratosphere where it mostly absorbs UV radiation in Hartley and Huggins bands, contributing to the determination of the vertical temperature structure and dynamics of airmasses. The remaining 10% of atmospheric ozone is in the troposphere. Reliably monitoring the ozone both in the stratosphere and in the troposphere is one of the main issues in Atmospheric Sciences, due to the reported downward trend in stratospheric ozone and subsequent risks in the enhancement of surface UV radiation, and to the possible upward trend of tropospheric ozone and subsequent risks in global warming, and, at lower levels, for the toxicity of this gas.

The derivation of atmospheric parameters from satellite remote sensing instruments plays a key-role in monitoring the Earth's atmosphere and to address the many related scientific issues. As mentioned in the previous Chapters, a typical problem is related to the inversion of the measured radiance data to obtain height resolved information on ozone concentration. To this aim, the most frequently adopted inversion algorithms have been, historically, OE schemes; they rely on the use of forward radiative transfer calculation and some a priori information. In addition, an accurate calibration of the

input data is crucial. In the previous Chapters, we proposed alternative NN based schemes to retrieve the TOC from Earths radiance UV/VIS nadir measurements (see Chapter 4), as well as ozone profiles (see Chapter 5). Both approaches have been tailored to EnviSat SCIAMACHY data. NN algorithms are particularly suited to solve complex nonlinear problems like the inversion of satellite radiance measurements for atmospheric profiles retrieval, without the need of direct radiative transfer calculation or accurate calibration/systematic error correction of input data. The nets were trained using both simulated and experimental data.

In the present Chapter we present our NN algorithms for height resolved ozone concentration retrievals from Aura OMI UV/VIS measurements. Indeed, the enhanced horizontal resolution of the OMI sensor is more satisfactory with respect to the needed spatial resolution, as indicated in [113], for reliably monitoring atmospheric pollution phenomena; in addition this sensor ensures a daily global coverage. Design issues of the net are analyzed in Sec. (6.3); results are presented and discussed in Sec. (6.4); in Sec (6.5) conclusion is given and future work is pointed out.

6.2 Training and test sets generation

The data used here were taken from the AVDC database, please refer to Sec. (2.2.6). We decided to train our net for OMI data with v2.2 MLS stratosphere-to-upper-troposphere ozone volume mixing ratio profiles. The MLS on Aura spacecraft can observe thermal emission from the atmospheric limb in broad spectral ranges centered near 118.0, 190.0, 240.0 and 640.0 GHz, and 2.5 THz [53]. Amongst the available Level 2 products, the MLS can provide ozone mixing ratios. These measurements are widely regarded as reliable in the altitude range $\sim 215.00 - 0.02$ hPa. After some analyses on vertical resolution, we found that only 9 pressure levels, i.e. in the interval $\sim 200.0 - 1.5$ hPa can be reliably derived with our nets, so we re-sampled the MLS profiles accordingly. The obtained vertical resolution is about 4 to 5 km. As input we chose OMI spectral UV/VIS reflectances derived from OMI Level 1b data. Accurate quality checks on the data have been applied, based on the several quality flags in the Level 1b data. A very strict time-space matching procedure has been applied to collocate the OMI and the MLS measurements. It has to be noted that, due to the fact that the two instruments are on the same payload of Aura spacecraft, a huge amount of matching pixels have been found. This allowed the application of very short time and space matching windows. The (randomly) selected input-output pairs to the net were finally 20000 out of millions available in the period 2005-2006. Our exercise was restricted to mid-latitudes.

6.3 Algorithm optimization

We started with an EP procedure to reduce the input measurement vector. We used 10000 out of the 20000 input-output pairs for this issue. After several thousands iterations we obtained an input vector of 29 wavelengths. Most of these wavelengths were in the interval 300.0-310.0 nm (with no $\lambda > 315.0$ nm), which lie in the most sensitive spectral band to stratospheric and upper tropospheric ozone profile variations. It can be noted that the input vector to SCIAMACHY NN (see Chapter (5)) has also higher wavelengths, maybe due to the fact that it retrieves concentrations also at lower altitude levels.

To find an optimal topology, we investigated the number of hidden layers and the numbers on neurons in a layer. We found that the best performance is obtained with 1 hidden layer containing 29 neurons. Finally, the selected topology was 29-29-9. The ratio between hidden and input neurons is lower than that for SCIAMACHY NN, see Sec. (5.3), maybe due to a higher computational complexity for tropospheric retrievals; in any case it has to be noted that the number of hidden neurons, and then the order of the approximating function (see Sec. 3.3), is the same for the two nets.

6.4 Results

We trained and tested the net with the remaining 10000 input-output pairs in the OMI-MLS database. 7000 pairs were used for the training phase, while 3000 of them were used to test the obtained net. Training and test set data were taken from different orbits. We applied an early stopping procedure: we stopped the training when the error on the test subset started to rise. This approach ensures generalization capabilities to the net. Fig. (6.1) shows two examples of retrieved profiles compared with measured MLS target profiles. We found that different trends in the upper troposphere/tropopause and different heights of the ozone peak can be detected.

In Fig. (6.2) two scatter plots of the retrieved ozone concentrations at two levels versus target values for the test dataset is reported. As it is possible to see correlation is 0.94 and 0.93 in terms of the Pearson correlation coefficient. Also correlations at upper tropospheric levels are remarkable. In general, Pearson coefficient values are higher than 0.88 at all levels.

Fig. (6.3) shows the RMS deviation profile in the overall test dataset versus the standard deviation profile of the MLS target dataset. At all heights the RMS is lower than the standard deviation of the target measurements. In Fig. (6.4) the absolute mean

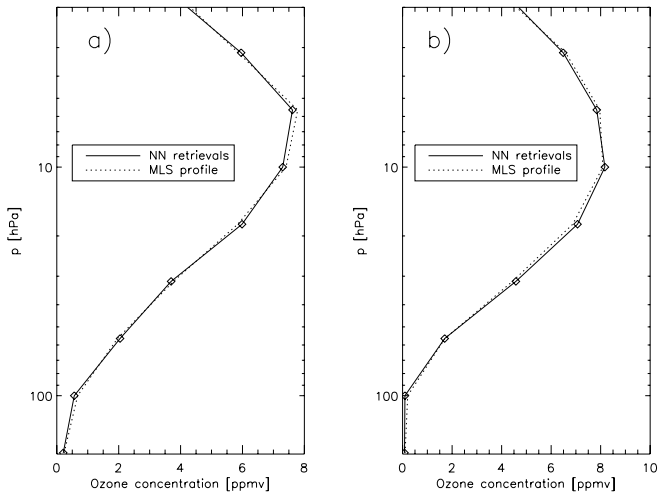

FIGURE 6.1: Two examples of OMI-NN retrieved profiles (line with diamonds), with MLS target profile (dotted line) as a comparison. a) Lat/lon = N43.00, E62.48, JD = 126/2005; b) Lat/lon = N39.41, E22.56, JD=180/2006.

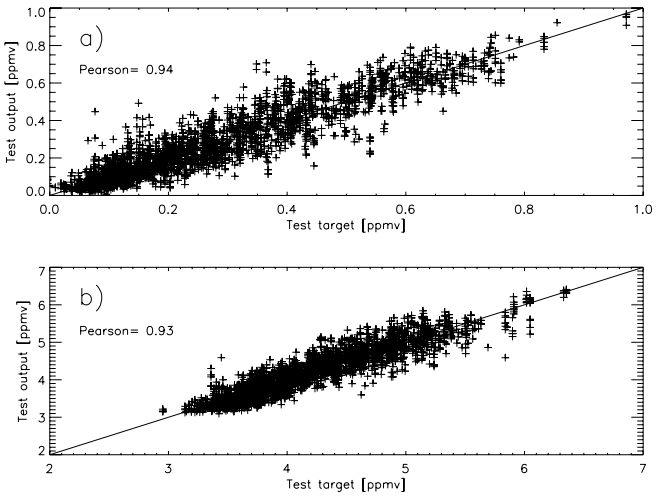

FIGURE 6.2: Two scatter plots of the retrieved ozone mixing ratios vs MLS target values for the test dataset. a) P = 177.83 hPa; b) P = 1.78 hPa.

differences (%) are reported. As it is possible to notice, the differences are lower than 7% at the seven higher altitudes, while reaching values higher than 20% at lower levels.

6.5 Conclusion

In this Chapter we have reported on some experiments on NNs based inversions of Aura OMI UV/VIS reflectance data for height resolved ozone concentration retrievals. OMI data have been matched with Aura MLS measurements; we derived stratospheric-to-upper-tropospheric profiles. The net demonstrated encouraging retrieval capabilities,

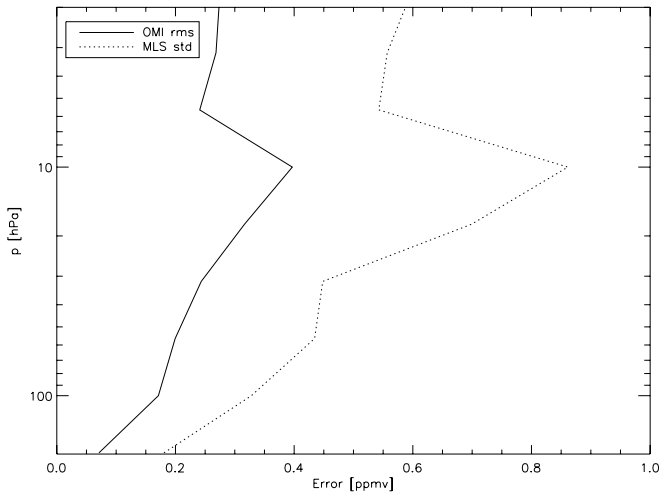

FIGURE 6.3: RMS deviation profile of the retrievals (line) and MLS target values' standard deviation (dotted line), over the test dataset.

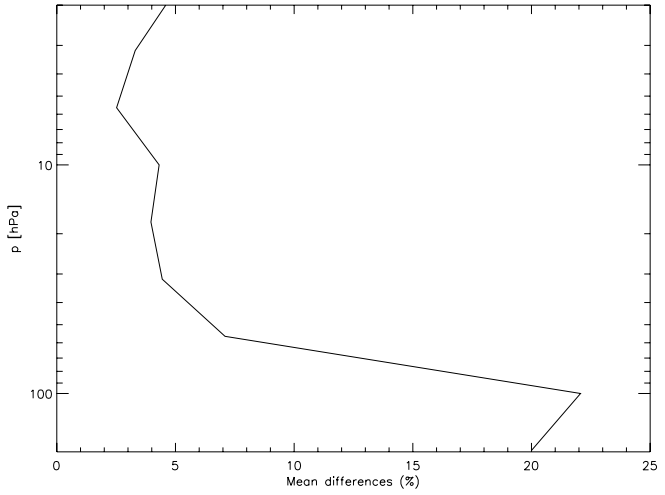

FIGURE 6.4: Mean absolute differences (%) of our retrievals over the test dataset.

being the correlations of the retrieved values versus *true* values > 0.88. The nets appear to catch tropospheric ozone phenomena and variations, though additional investigation has to be carried out, as well as a thorough validation of the algorithm. Generally the retrievals from OMI data appear to be of a better quality than those from SCIAMACHY (see Chapter 5), probably due to the stricter matching with correlative data. It has to be noted that the daily global coverage of this instrument's measurements process, with the aid of NN techniques, can help in short time monitoring of ozone related phenomena. Finally we'd like to stress that NNs, unlike OEs, don't need in principle the removal of systematic errors on input data and radiative transfer calculations. Investigation on how well our nets deal with systematic errors and how well they behave in situations of difficult direct radiative transfer calculation (e.g. aerosols and clouds) are ongoing.

Pasquale Sellitto: sellitto@disp.uniroma2.it

Conclusion

Monitoring ozone from satellite platform is a powerful means to address climate change and environmental issues both locally and at a global scale. The inversion of nadir observations is usually carried out by the OE technique. This approach is very useful and was successfully applied to several nadir UV/VIS sensors, but it presents some limitations. In fact, OE is sensitive to systematic errors in the input measurements and to particular atmospheric scenarios as cloudy pixels or aerosols. NNs can circumvent these problems. In addition, traditional approaches for solving nonlinear inverse problems, as is the retrieval of the vertical distribution of an atmospheric component from electromagnetic measurements, are based on numerical solutions by iterative methods, and with the use of a forward model. This implies large computational burdens and long times for processing. Even if computing technology will provide faster and faster processors, the amount of available satellite data to be processed is also increasing. Moreover, large re-processing activities of archived datasets are often envisaged, in order to improve the information extracted from measurements. Hence, faster inversion algorithms are always welcome, and neural networks can represent a powerful tool for achieving this goal.

The work described in this thesis reports on some NNs algorithms to retrieve a) tropospheric ozone columns, and b) ozone concentration profiles, from nadir UV/VIS satellite data. The considered sensors were SCIAMACHY and OMI. We described the design of:

1. a NN algorithm for retrieving TOCs from simulated/experimental SCIAMACHY data (Chapter 4);
2. a NN algorithm for the retrieval of stratosphere-to-troposphere ozone concentration profiles from SCIAMACHY data (Chapter 5)
3. a NN algorithm for retrieving stratospheric ozone concentration profiles from OMI data (Chapter 6).

The datasets for the training/test phases were generated using concentration profiles from WOUDC/SHADOZ ozonesondes and Aura-MLS satellite data. The selection of

input measurements , i.e. of the measurements which carry the larger information content, were systematically carried out by means of combined RTM-NN/EP procedures. The application of the NN retrieval technique to estimate other relevant atmospheric parameters has also been investigated. The cases considered in Appendix A concern the retrieval of temperature profiles and nitrogen dioxide columns from the same input data (i.e. radiances measured by UV/VIS sensors) to better characterize the atmospheric state. Finally the project for an extensive validation of the algorithms in a GRID environment is presented in Appendix B.

The obtained results demonstrate the great versatility of NNs in addressing inversion problems, and confirm their capability to catch the functional relationship between electromagnetic measurements and height-resolved atmospheric parameters. NNs can be therefore considered a very competitive approach for solving this kind of problems. This approach can easily be extended to next generation satellite sensors, as the GOME-2 on MetOp-a, or the new GMES-Sentinel 4 and 5.

Pasquale Sellitto: sellitto@disp.uniroma2.it

Appendix A

NNs for the retrieval of other atmospheric parameters

Part of this Chapter's contents is extracted from the publication: [114].

A.1 Introduction

Nitrogen dioxide (NO_2) is a major air pollutant, it contributes to the photochemical ozone production in the troposphere and it is toxic for inhalation. The bulk of nitrogen dioxide is of anthropogenic origin and is produced at the ground level of continental areas by industrial activity and combustion of fossil fuel. NO_2 concentrations at low altitudes are expected to vary from daytime to nighttime, due to variations of road traffic flow and of atmospheric dispersion. Variations from weekdays to Sundays are also observed, while seasonal variations are less important. Meteorological and topographic features can contribute in conjunction with the pollution sources to create events of severe air pollution. Subsiding air masses prevent the air in the boundary layer from moving upwards and dispersing the pollutants. Such kind of stagnation can be monitored by analyzing the vertical thermal structure of the atmosphere.

The availability of retrieval methods suitable to cope with the atmospheric system complexity is crucial. Recent results have demonstrated the effectiveness and reliability of NN-based inversion algorithms for ozone retrieval from UV/VIS satellite nadir data. In the previous Chapters we discussed NN algorithms to retrieve both tropospheric ozone columns (Chapter 4) and ozone concentration profiles (Chapter 5 and 6) from UV/VIS satellite nadir data. Retrieving a set of atmospheric parameters from the same input

satellite data vector is a tantalizing task, given the possibility of a comprehensive depiction of the air pollution event (e.g., concentrations of ozone and of ozone precursors and relevant meteorological parameters) from co-located and inter-calibrated measurements.

Here we propose a synergistic approach to air pollution monitoring based on the simultaneous retrieval of NO_2 concentrations and temperature vertical profiles from the same UV/VIS nadir satellite measurements. The two novel NN algorithms and their design issues are described in Sec.s (A.2) and (A.3) together with a preliminary sensitivity analysis. The results and the performances of the algorithms, referring to simulated data, are finally discussed.

A.2 NNs for the retrieval of temperature profiles from satellite UV/VIS simulated radiances

A.2.1 Sensitivity analysis

A height resolved climatology of temperature and ozone is described in [115]. The considered measurements come from both ozonesondes/radiosondes and satellites. The total ozone is used as a parameter, and profiles are clustered versus its measured values. In particular, the authors derived a set of 7 seasonal climatological profiles with respective standard deviations for each 30 latitude interval, sorting the profiles in 30 DU total ozone ranges. Later in the Chapter, we will refer as *Lamsal climatology* for the set of climatological profiles, from the name of the first author of the publication [115].

We used this dynamical climatology to analyze the sensitivity of a simulated satellite UV/VIS radiance measurement to temperature profile variations, as well as to assess the possible screening from ozone profile variations. We started from the AFGL mid-latitude standard temperature and ozone profiles and the UVSPEC radiative transfer model [107] to study the computed radiances variations when varying the temperature and ozone profiles according to the mentioned 7 climatologies. The analysis has been restricted to the summer conditions. The analysis is based on the quantity:

$$R\left(O_3^{\mathrm{AFGL}}(z), T^{\mathrm{AFGL}}(z), \vec{P}^{\mathrm{AFGL}}\right) = R^{\mathrm{AFGL}} \tag{A.1}$$

i.e., the radiance R computed from the AFGL profiles of temperature and ozone. In Eq. (A.1), $\vec{P}$ is a vector summarizing the effect of other model parameters as aerosols optical properties, surface albedo, etc. The values (A.1) have been compared with 2 groups of 7 quantities:

$$R\left(O_3^{\mathrm{Lamsal(n)}}(z), T^{\mathrm{AFGL}}(z), \vec{P}^{\mathrm{AFGL}}\right) = R^n_{O_3} \tag{A.2}$$

$$R\left(O_3^{\mathrm{AFGL}}(z), T^{\mathrm{Lamsal(n)}}(z), \vec{P}^{\mathrm{AFGL}}\right) = R_T^n \tag{A.3}$$

with n = 1, ..., 7 denoting the 7 *Lamsal* climatological profiles. Quantities (A.1), (A.2) and (A.3) have been computed in the range 220.0-800.0 nm by modeling ESA-Envisat SCIAMACHY measurements via its slit function and operating wavelengths. Then the spectral differences (%) have been computed by:

$$\mathrm{Diff}_{O_3,T}^n = 100 * \frac{R_{O_3,T}^n - R^{\mathrm{AFGL}}}{R^{\mathrm{AFGL}}} \tag{A.4}$$

As can be seen from Fig. (A.1), at shorter wavelengths, the variation caused by the ozone change masks the effect of the temperature variations; analogously, at wavelengths higher than 400 nm, the effect of $\vec{P}$ dominates the interactions with radiation [116]. However, if we investigate more closely the 320.0-325.0 nm interval, where the ozone cross section is more dependent on temperature profile, we can notice some interesting features. For a better understanding, we introduced the following parameter:

$$\mathrm{Diff}_{\mathrm{rel}}^n = \frac{\mathrm{Diff}_T^n}{\mathrm{Diff}_{O_3}^n} = \frac{R_T^n - R^{\mathrm{AFGL}}}{R_{O_3}^n - R^{\mathrm{AFGL}}} \tag{A.5}$$

which is displayed in the 320.0-325.0 nm interval, for the 7 total ozone classes by Fig. (A.2). The diagrams indicate that, for many of the 7 classes, the sensitivity to temperature profile variations is higher than that to ozone profile variations, especially close to about 321.2 nm and about 323.8 nm. In Fig. (A.3) we report the absolute value of the relative sensitivity given by Eq. (A.5) at 323.8 nm versus total ozone. A similar behavior is observed at 321.2 nm. Hence, a reasonable relative sensitivity to temperature exists for moderate values of total ozone, whereas the sensitivity is scarce for both the highest and lowest values. It can be remarked that the extreme values are quite uncommon at mid-latitudes [115]. It has to be remembered that: a) in the selected band the aerosols optical depth can damp the sensitivity, b) a dependency on the surface albedo exists, and c) although the relative sensitivity is significant, the absolute sensitivities remain quite low (Fig. (A.1)). Despite these points, retrieval seems feasible in the 320.0-325.0 nm band.

A.2.2 Algorithm design and optimization

Following the sensitivity analysis, we decided to exploit the 320.0-325.0 nm spectral interval. At this stage, we only used simulated data. As for the sensitivity analysis, we produced a radiance database through the UVSPEC radiative transfer model. Both the

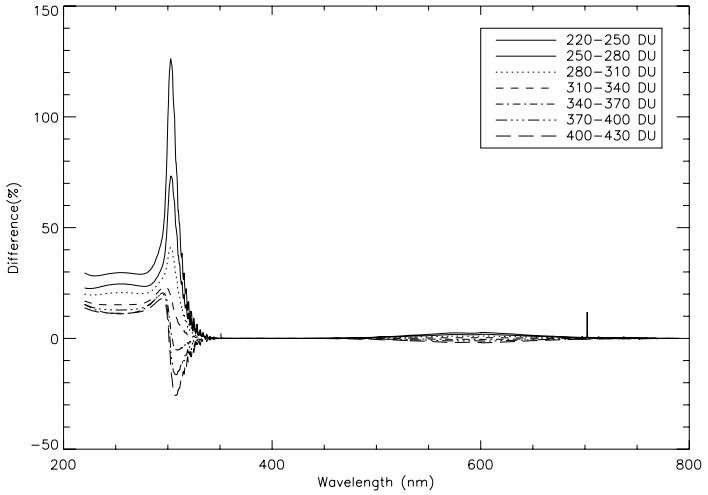

(a) O_3

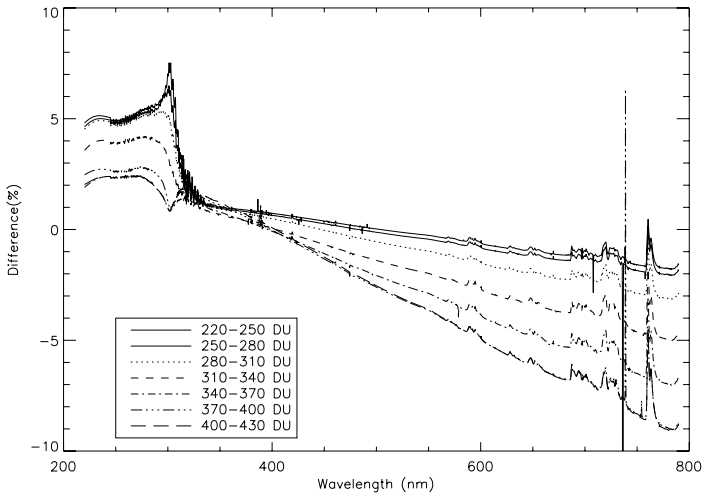

(b) T

FIGURE A.1: Spectral radiance differences (%) of Eq. (A.4) for the 7 total ozone dependent climatologies of [115]. (a) Lamsal ozone profiles, fixed AFGL temperature profile, (b) Lamsal temperature profile, fixed AFGL ozone profile.

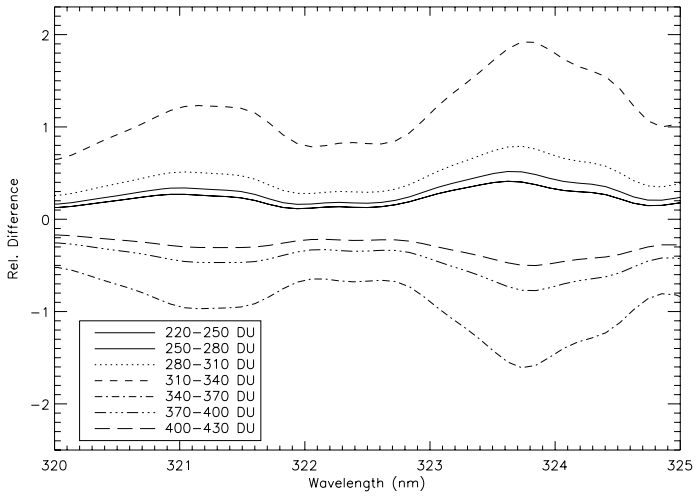

FIGURE A.2: Relative spectral differences of Eq. (A.5).

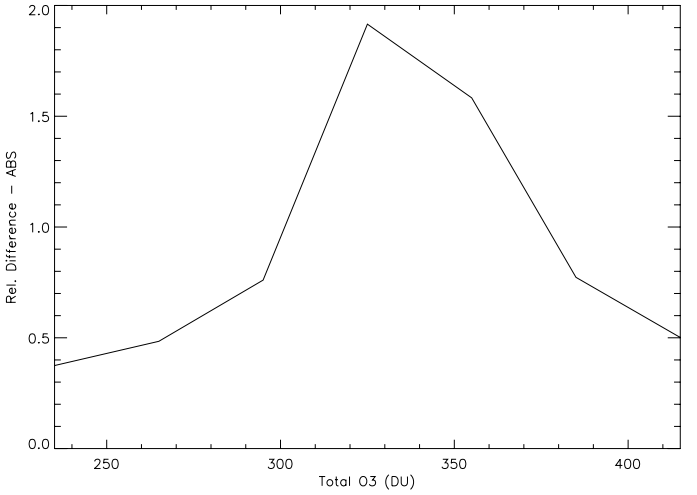

FIGURE A.3: Absolute relative differences of Eq. (A.5) versus total ozone, at $\sim$ 323.8 nm

temperature and the ozone profiles were varied, starting from the most populated climatology in [115], i.e., for total ozone $\sim$320 DU. Zero-means variations of ozone concentrations and temperature were randomly generated, with a Gaussian distribution having the same standard deviation as in the considered climatology. We finally obtained 8000 spectral radiances-temperature profiles pairs. Temperature has been interpolated at 13 altitude levels, spanning from troposphere to stratosphere, with a height resolution of about 5 km. The input vector, initially containing the spectral radiances at 45 wavelengths, was reduced by an NN-based EP procedure [104]. We used 4000 out of the 8000

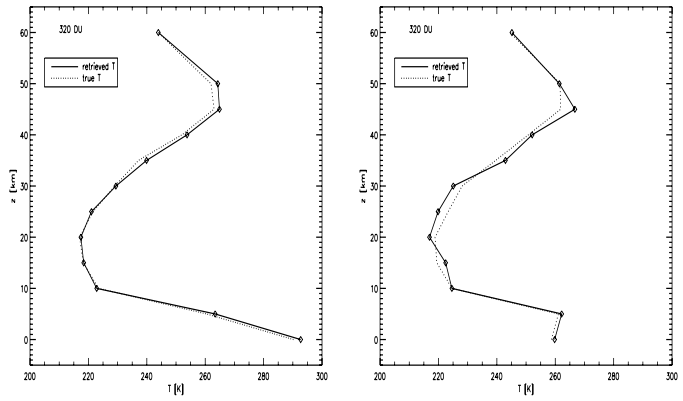

(a) Example 1 (b) Example 2

FIGURE A.4: Examples of a retrieved profile (diamond with line) with the corresponding true profile (dotted line). Total ozone is 320 DU.

pairs to this aim. The most informative wavelengths were found in the ranges 321.0-321.4 nm and 323.5-324.1 nm, consistently with the results of the sensitivity analysis of Sec. (A.2.1). Finally, 23 wavelengths were selected. Once defined the input structure, the optimal NN topology, i.e., the number of hidden layers and the number of neurons in a layer has been found in a heuristic way. The best performance was yielded by a single hidden layer with 23 neurons, so that, the selected topology was 23-23-13.

A.2.3 Results

We trained and tested the net with the remaining 4000 input/output pairs of the synthetic database. 3000 pairs were used for the training phase, while 1000 of them were used for testing. The obtained nets retrieval capabilities have been assessed with simulated measurements corresponding to different atmospheric states, including tropospheric temperature inversions and extreme total ozone values. Figs. (A.2.3(a)) and (A.2.3(b)) display retrieved and *true* profiles. It can be noticed that also tropospheric inversions can be identified (Fig. (A.2.3(b))). However, it should be remembered that the obtained results refer to mid-latitudes and total ozone around 300-320 DU.

A.3 NNs for the retrieval of nitrogen dioxide columns from satellite UV/VIS simulated radiances

A.3.1 Sensitivity analysis

As for temperature, we studied the sensitivity of simulated satellite radiance measurements to nitrogen dioxide profile variations. The climatological standard NO_2 concentration profiles have been varied to reproduce a set of HALogen Occultation Experiment (HALOE) data [56]. The HALOE limb sensor on board the Upper Atmosphere Research Satellite (UARS) has been routinely measuring vertical profiles of several atmospheric parameters since 1991. HALOE NO_2 profiles in the period 2003-2005 have been used to compute a mean profile with height-resolved standard deviation. We restricted our analysis to mid-latitudes and winter, resulting in about 2500 profiles. Winter was chosen, given the larger number of measured profiles available. HALOE Volume Mixing Ratios (VMRs) are considered reliable in the height range 10-50 km. We varied the profile at different levels and computed the corresponding radiance spectrum in the range 350.0-550.0 nm. We observed an exiguous sensitivity to the NO_2 concentration profiles (results not shown here). Rather, a small but non-negligible sensitivity was found to the total column nitrogen dioxide, hence we carried out further analyses on the retrieval of this parameter.

A.3.2 Algorithm design and optimization

The set of spectral radiance-NO_2 total column has been computed by the UVSPEC radiative transfer model. We varied the mean HALOE profile within with the standard deviation profile range thus generating a database of 8000 NO_2 profiles. Then we computed the corresponding 8000 radiance spectra in the range 350.0-550.0 nm and we matched the spectra with the corresponding integrated profile. As for temperature, a reduction of the NN input vector was carried out by an EP using 4000 out of the 8000 pairs. The most informative wavelengths were found in the range 405.0-465.0 nm. This finding is consistent with the selected band for the operational NASA algorithm for NO_2 column OMI product [117]. Finally, 40 wavelengths were selected. We also determined the optimal number of hidden layers and the numbers on neurons in them. The best performance was obtained with 1 hidden layer containing 40 neurons, so that the selected topology was 40-40-1.

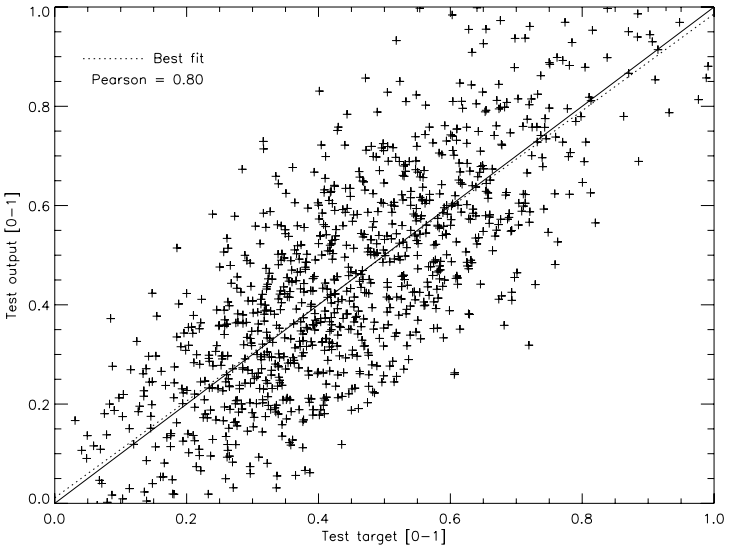

FIGURE A.5: Scatterplot of the NN retrieved NO_2 columns vs true values for the test dataset.

A.3.3 Results

We trained and tested the net with the remaining 4000 input/output pairs of the synthetic database. As before, 3000 pairs were used for training and 1000 for testing. A scatter plot of the retrieved NO_2 columns versus *true* values is reported In Fig. (A.5). A reasonable correlation appears, with a Pearson coefficient about 0.80.

A.4 Conclusion

In this appendix we reported experiments on NN-based inversions of a simulated ESA-EnviSat SCIAMACHY UV/VIS radiance single set to retrieve height-resolved temperature and nitrogen dioxide. The study was based on a sensitivity analysis performed by the LibRadtran suite. The nets demonstrated retrieval capabilities both for temperature profiles and nitrogen dioxide total column. No satisfactory results were achieved for height-resolved nitrogen dioxide concentration retrievals. Given the ability of neural algorithms to handle heterogeneous quantities, the NN tools can lead to a comprehensive understanding of air pollution phenomena. Testing and validating the developed algorithms with actual SCIAMACHY and OMI data are planned towards applications to atmospheric pollution monitoring. Investigations on the ability of our nets in discriminating tropospheric to stratospheric nitrogen dioxide columns, hence the identification of anthropogenic nitrogen dioxide production, are also ongoing.

Pasquale Sellitto: sellitto@disp.uniroma2.it

Appendix B

Grid technology for the validation of NNs algorithms for ozone retrieval

This activity is performed in the context of ESA Cat-1 project no. 4069. The project is ongoing.

Neural networks algorithms need an accurate validation work. In the last years several validation activities have already been performed for retrieval algorithm exploiting ESA-ERS2 GOME data, and the results are satisfactory [104, 105]. However, a global and long term validation work still has to be carried out due to the huge amount of data to be processed for this purpose; on the other hand, the algorithms that use SCIAMACHY and OMI data are only provisionally validated. Grid computing is the application of several computers to a single problem at the same time, usually to a scientific or technical problem that requires a great number of computer processing cycles or access to large amounts of data. Grid computing depends on software to divide and apportion pieces of a program among several computers, sometimes up to many thousands. Grid computing can also be thought of as distributed and large-scale cluster computing, as well as a form of network-distributed parallel processing. A grid environment like the ESA G-POD [118] could provide the computational means to fulfill this kind of needing. Therefore a work is ongoing for embedding already designed NNs algorithms in a grid environment, using SCIAMACHY and GOME datasets for global and long-term validation, and, eventually, to refine the algorithms by re-training the nets with the extended dataset available in the G-POD. The work is at a very early stage; the prototype design has been defined (see Fig. (B.1)), and a part of the overall processes has been transferred in the operational G-POD platform in the last few weeks.

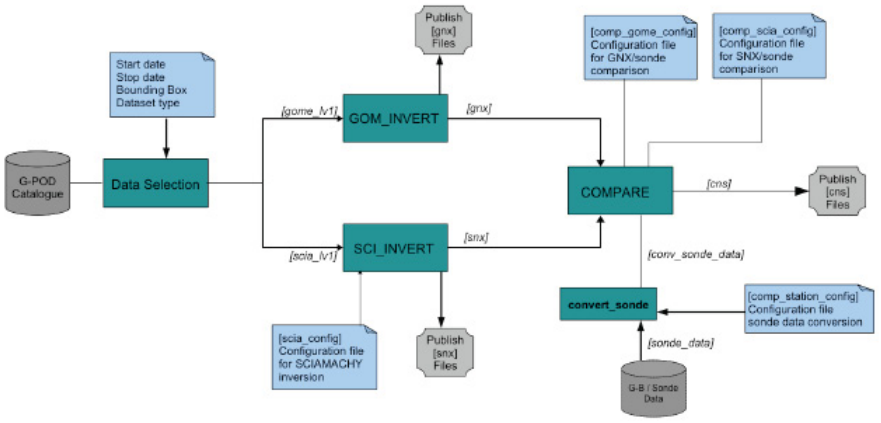

FIGURE B.1: ESA Cat-1 G-POD project 4069 end to end prototype design.

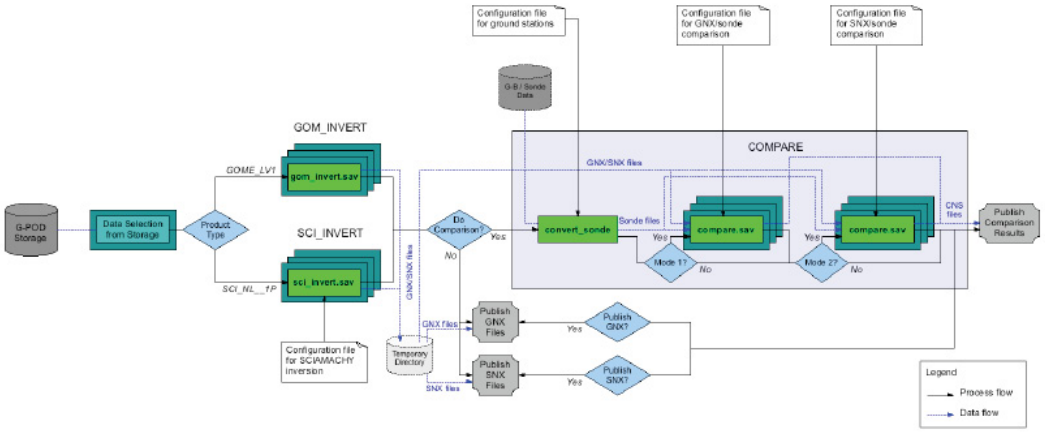

FIGURE B.2: ESA Cat-1 G-POD project 4069 end to end processing and data workflow.

In Fig. (B.1), green boxes refer to our IDL chainable executable files. Light blue boxes refer to parameters to be defined and configuration files. Grey cylinders refers to ground-based (G-B), ozonesondes (WOUDC and SHADOZ datasets) reference data and the G-POD catalogue; we have access to reference data by direct correspondence with responsible staffs.

Fig. (B.2) shows more closely the processing and data flow as designed for the overall future integration and hosting in GPOD. The core applications, depicted in green, are integrated into one box in the overall G-POD application workflow. The piled boxes in the scheme indicate that a job can be parallelized and executed on different nodes simultaneously.

The data selection is done through the definition of the temporal coverage of the data (start and stop date), a geographical limit (minimum longitude, minimum latitude, maximum longitude and maximum latitude) and finally the dataset type (GOME Level 1 or SCIAMACHY Level 1b). Products belonging to the defined dataset type, covering

the temporal interval and geographical region of interest are displayed. The inversion and comparison configuration parameters are defined through the web portal with addition, edition or deletion of configuration files.

Pasquale Sellitto: sellitto@disp.uniroma2.it

Bibliography

[1] J. T. Houghton et al. Eds. *Climate change 2001: The scientific basis. Third assessment of the Intergovernmental Panel on Climate Change, Working Group I report.* Cambridge University Press, New York, NY, USA, 2001.

[2] G. Fiocco. Il pianeta Terra. Dispense al corso di fisica terrestre. Università degli Studi di Roma La "Sapienza", Dipartimento di Fisica, 1998.

[3] G. Anderson, S. Clough, F. Kneizys, J. Chetwynd, and E. Shettle. AFGL atmospheric constituent profiles (0-120 km). Technical Report AFGL-TR-86-0110, Air Force Geophysics Laboratory, Hanscom Air Force Base, Bedford, MD, USA, 1986.

[4] Scientific assessment of ozone depletion: 2006, Executive Summary. Technical Report 50, World Meteorological Organization, Geneva, Switzerland, 2006.

[5] M. R. Schoeberl et al. EOS science plan. National Aeronautics and Space Administration - Goddard Space Flight Center, Atmospheric Chemistry and Dynamics Branch, 1997.

[6] S. Chapman. A theory of upper atmospheric ozone. *Memorial of the Royal Meteorological Society*, 3:103–25, 1930.

[7] Scientific assessment of ozone depletion: 2002, Executive Summary. Technical Report 47, World Meteorological Organization, Geneva, Switzerland, 2002.

[8] P. J. Crutzen. The influence of nitrogen oxide on the atmospheric ozone content. *Quarterly Journal of Royal Meteorological Society*, 96:320–5, 1970.

[9] J. H. Seinfeld and S. N. Pandis. *Atmospheric chemistry and physics: from air pollution to climate change.* J. Wiley and sons, New York, NY, USA, 1998.

[10] J. C. Farman, B. C. Gardiner, and J. D. Shanklin. Large loss of total ozone in Antarctica reaveal seasonal $\mathrm{Clo}_x/\mathrm{No}_x$ interaction. *Nature*, 315:207–10, 1985.

[11] S. Solomon, R. R. Garcia, F. S. Rowland, and D. J. Wuebbles. On the depletion of Antarctic ozone. *Nature*, 321:755–8, 1986.

[12] J. K. Angell et al. Southern hemisphere winter summary. Technical report, National Oceanic and Atmospheric Administration, 2002.

[13] Environment Canada website, *http://exp-studies.tor.ec.gc.ca/*.

[14] R. Guicherit and M. Roemer. Tropospheric ozone trends. *Chemosphere Global Change Science*, 2:167–83, 2000.

[15] D. M. Murphy and D. W. Fahey. An estimate of the flux of stratospheric reactive nitrogen and ozone into the troposphere. *Journal of Geophysical Research*, 99: 5332–52, 1994.

[16] P. J. Crutzen. A discussion of the chemistry of some minor constituents in the stratosphere and troposphere. *Pure and Applied Geophysics*, 1385:106–8, 1973.

[17] J. F. Müller and G. I. Brasseur. IMAGES: A three-dimensional chemical-transport model of the global troposphere. *Journal of Geophysical Reasearch*, 100:1644590, 1995.

[18] D. A. Hauglustaine, L. Emmons, M. Newchurch, G. Brasseur, T. Takao, K. Matsubara, J. Johnson, B. Ridley, J. Stith, and J. Dye. On the role of lightning NO_x in the formation of tropospheric ozone plumes: A global model perspective. *Journal of Atmospheric Chemistry*, 38(3):277–94, 2001.

[19] H. B. Singh, M. Kanakidou, P. J. Crutzen, and D. J. Jacob. High-concentrations and photochemical fate of oxygenated hydrocarbons in the global troposphere. *Nature*, 378(6552):50–4, 1995.

[20] A. M. Thompson, J. C. Witte, S. J. Oltmans, F. J. Schmidlin, J. A. Logan, M. Fujiwara, V. W. J. H. Kirchhoff, F. Posny, G. J. R. Coetzee, B. Hoegger, S. Kawakami, T. Ogawa, J. P. F. Fortuin, and H.M. Kelder. Southern Hemisphere ADditional OZonesondes (SHADOZ) 1998-2000 tropical ozone climatology 2. Tropospheric variability and the zonal wave-one. *Journal of Geophysical Research*, 108(D2): 8241, 2006.

[21] J. Logan et al. Trends in the vertical distribution of ozone: A comparison of two analyses of ozonesonde data. *Journal of Geophysical Research*, 104:26373–99, 1999.

[22] S. Chalita, D. A. Hauglustaine, H. Le Treut, and J. F. Müller. Radiative forcing due to increased tropospheric concentrations. *Atmospheric Environment*, 30:1641–6, 1996.

[23] L. T. Molina and M. J. Molina. Absolute absorption cross section of ozone in the 185-350 nm wavelength range. *Journal of Geophysical Research*, 91(D13):14501–8, 1986.

[24] D. Fuà. Dispense al corso di fisica terrestre. Università degli Studi di Roma La Sapienza, Dipartimento di Fisica, 2006.

[25] SPARC/IOC/GAW, *Assessment of trends in the vertical distribution of ozone*, *http://www.atmosp.physics.utoronto.ca/people/sparc/SPARCReport1/1.08_O3sondes/*.

[26] World Ozone and Ultraviolet Radiation Data Centre (WOUDC) homepage, *http://www.woudc.org*.

[27] A. M. Thompson, J. C. Witte, R. D. McPeters, S. J. Oltmans, F. J. Schmidlin, J. A. Logan, M. Fujiwara, V. W. J. H. Kirchhoff, F. Posnym, G. J. R. Coetzee, B. Hoegger, S. Kawakami, T. Ogawa, B. J. Johnson, H. Vmel, and G. Labow. Southern Hemisphere ADditional OZonesondes (SHADOZ) 1998-2000 tropical ozone climatology 1. Comparison with Total Ozone Mapping Spectrometer (TOMS) and ground-based measurements. *Journal of Geophysical Research*, 108(D2):8238, 2006.

[28] J. Kerr, C. T. McElroy, D. I. Wardle, R. A. Olafson, and W. F. J. Evans. The automated brewer spectrophotometer. *Proceedings of the quadriennial Ozone Symposium, Halkidiki, Greece*, page 396, 1985.

[29] A. Sarkissian, G. Vaughan, H. K. Roscoe, L. M. Bartlett, F. M. O'Connor, D. G. Drew, P. A. Hughes, and D. M. Moore. Accuracy of measurements of total ozone by a SAOZ groundbased zenith sky visible spectrometer. *Journal of Geophysical Research*, 102(D1):1379–90, 1997.

[30] G. J. Magie, G. Ancellet, and J. Pelon. Lidar measurements of ozone vertical profiles. *Applied Optics*, 24(21):3454–63, 1985.

[31] C. L. Mateer and J. J. DeLuisi. A new Umkehr inversion algorithm. *Journal of of atmospheric and terrestrial physics*, 54(5):537–56, 1992.

[32] I. S. Mc Dermid, S. Godin, and T. D. Walsh. Lidar measurements of stratospheric ozone and intercomparisons and validation. *Applied Optics*, 29:4914–23, 1990.

[33] G. Fiocco, P. G. Calisse, M. Cacciani, S. Casadio, G. Pace, and D. Fuà. ABLE: Development of an airborne lidar. *Journal of Atmospheric and Oceanic Technology*, 16(10):1337–44, 1999.

[34] R. M. Measures. *Laser remote sensing: Fundamentals and applications*. John Wiley and sons, New York, NY, USA, 1984.

[35] P. Lier and M. Bach. PARASOL: a microsatellite in the A-Train for Earth atmospheric observations. *Acta Astronautica*, 62:257–63, 2008.

[36] D. M. Winker, J. Pelon, and M. P. McCormick. The CALIPSO mission: spaceborne lidar for observation of aersosols and clouds. In *Proceedings of SPIE*, volume 4893, pages 1–11, 2003.

[37] R. D. McPeters and W. D. Komhyr. Long-term changes in the Total Ozone Mapping Spectrometer relative to world primary standard Dobson spectrometer 83. *Journal of Geophysical Research*, 96:2987–93, 1991.

[38] R. D. McPeters, R. D. Hudson, and P. K. Bhartia. The vertical ozone distribution in the Antarctic ozone minimum measured by SBUV. *Geophysical Research Letters*, 13(12):1213–6, 1986.

[39] A. J. Miller et al. Information content of Umkehr and solar backscattered ultraviolet (SBUV-2) satellite data for ozone trends and solar responses in the stratosphere. *Journal of Geophysical Research*, 102(D15):19257–63, 1997.

[40] E. Hilsenrath, P. A. Newman, R. P. Cebula, P. W. DeCamp, T. J. Kelly, and L. Coy. Ozone change from 1992 to 1993 as observed from SBUV on the ATLAS-1 and ATLAS-2 missions. *Geophysical Research Letters*, 23(17):2305–8, 1996.

[41] J. P. Burrows, M. Weber, M. Buchwitz, V. Rozanov, A. Ladstatter Weissenmayer, A. Richter, R. DeBeek, R. Hoogen, K. Bramstedt, K. U. Eichmann, and M. Eisinger. The global ozone monitoring experiment (GOME): Mission concept and first scientific results. *Journal of the Atmospheric Sciences*, 56(2):151–75, 1999.

[42] B. J. K. Kerridge, R. Siddans, B. L. Latter, J. P. Burrows, M. Weber, R. De Beek, I. Aben, and W. Hartman. GOME-2 error assessment study. Technical Report EUM/CO/01/901/DK, EUMETSAT, 2002.

[43] S. Noël, H. Bovensmann, M. W. Wuttke, J. P. Burrows, M. Gottwald, E. Krieg, A. P. H. Goede, and C. Muller. Nadir, limb, and occultation measurements with SCIAMACHY. *Advances in Space Research*, 29(11):1819–24, 2002.

[44] P. F. Levelt, G. H. J. van den Oord, M. R. Dobber, A. Mlkki, H. Visser, J. de Vries, P. Stammes, J. O. V. Lundell, and H. Saari. The Ozone Monitoring Instrument. *IEEE Transaction on Geosciences and Remote Sensing*, 44(5):1093–101, 2006.

[45] E. E. Remsberg, J. M. Russell, J. C. Gille, L. L. Gordley, P. L. Bailey, W. G. Planet, and J.E. Harries. The validation of NIMBUS-7 LIMS measurements of ozone. *Journal of the Geophysical Research*, 89(D4):5161–78, 1984.

[46] P. L. Bailey, D. P. Edwards, J.C. Gille, L. V. Lyjak, S. T. Massie, A.E. Roche, J. B. Kumer, J. L. Mergenthaler, B. J. Connor, M. R. Gunson, J. J. Margitan, I. S. McDermid, and T.J. McGee. Comparison of Cryogenic Limb Array Etalon Spectrometer (CLAES) ozone observations with correlative measurements. *Journal of the Geophysical Research*, 101(D6):9737–56, 1996.

[47] B. J. Connor, C. J. Scheuer, D. A. Chu, J. J. Remedios, R. G. Grainger, C. D. Rodgers, and F. W. Taylor. Ozone in the middle atmosphere as measured by the improved stratospheric and mesospheric sounder. *Journal of the Geophysical Research*, 101(D6):9831–41, 1996.

[48] L. Froidevaux et al. Validation of UARS microwave limb sounder ozone measurement. *Journal of the Geophysical Research*, 101(D6):10017–60, 1996.

[49] D. Murtagh et al. An overview of the Odin atmospheric mission. *Canadian Journal of Physics*, 80(4):309–19, 2002.

[50] H. Fischer et al. MIPAS: an instrument for atmospheric and climate research. *Atmospheric Chemistry and Physics Discussion*, 7:8795–893, 2007.

[51] Y. Sasano, M. Suzuki, T. Yokota, and H. Kanzawa. Improved Limb Atmospheric Spectrometer (ILAS) for stratospheric ozone layer measurements by solar occultation technique. *Geophysical Research Letters*, 26:197–200, 1999.

[52] K. U. Eichmann, J. W. Kaiser, C. von Savigny, A. Rozanov, V. V. Rozanov, H. Bovensmann, M. von König, and J. P. Burrows. SCIAMACHY limb measurements in the UV/VIS spectral region: first results. *Advances in Space Research*, 34(4):775–9, 2004.

[53] J. Waters et al. The Earth Observing System Microwave Limb Sounder (EOS MLS) on the Aura satellite. *IEEE Transaction on Geosciences and Remote Sensing*, 44(5):1075–92, 2006.

[54] D. M. Cunnold, W. P. Chu, R. A. Barnes, M. P. McCormick, and R. E. Veiga. Validation of SAGE-II ozone measurements. *Journal of Geophysical Research*, 94(D6):8447–60, 1989.

[55] J. D. Lumpe, R. M. Bevilacqua, K. W. Hoppel, and C. E. Randall. POAM III retrieval algorithm and error analysis. *Journal of Geophysical Research*, 107(D20): 4575, 2002.

[56] J. M. Russell III et al. The HALogen Occultation Experiment. *Journal of Geophysical Research*, 98(D6), 1993.

[57] W. H. Swartz, J. H. Yee, R. J. Vervack Jr., S. A. Lloyd, and P. A. Newman. Photochemical ozone loss in the Arctic as determined by MSX/UVISI stellar occultation observations during the 1999/2000 winter. *Journal of Geophysical Research*, 107(D20):8296, 2002.

[58] J. L. Bertaux, G. Megie, T. Widemann, E. Chassefiere, R. Pellinen, E. Kyrölä, S. Korpela, and P. Simon. Monitoring of ozone trend by stellar occultations: The GOMOS instrument. *Advances in Space Research*, 11(3):237–42, 1991.

[59] P. K. Bhartia, R. D. McPeters, C. L. Mateer, L. E. Flynn, and C. Wellemeyer. Algorithm for the estimation of vertical ozone profiles from the backscattered ultraviolet technique. *Journal of Geophysical Research*, 101(D13):18793–806, 1996.

[60] X. Liu, K. Chance, C. E. Sioris, R. J. D. Spurr, T. P. Kurosu, R. V. Martin, and M. J. Newchurch. Ozone profile and tropospheric ozone retrieval from Global Ozone Monitoring Experiment (GOME): Algorithm description and validation. *Journal of Geophysical Research*, 110(D20):D20307, 2005.

[61] O. P. Hasekamp and J. Landgraf. Ozone profile retrieval from backscattered ultraviolet radiances: The inverse problem solved by regularization. *Journal of Geophysical Research*, 106(D8):8077–88, 2001.

[62] F. Del Frate, A. Ortenzi, S. Casadio, and C. Zehner. Application of neural algorithms for a real-time estimation of ozone profiles from GOME measurements. *IEEE Transaction og Geosciences and Remote Sensing*, 40(10):2263–70, 2002.

[63] M. D. Müller, A. K. Kaifel, M. Weber, S. Tellmann, J. P. Burrows, and D. Loyola. Ozone profile retrieval from Global Ozone Monitoring Experiment (GOME) data using a neural network approach (Neural Network Ozone Retrieval SYstem (NNORSY)). *Journal of Geophysical Research*, 108(D16), 2003.

[64] Y. J. Meijer et al. Evaluation of GOME ozone profiles from nine different algorithms. *Journal of Geophysical Research*, 111:D21306, 2006.

[65] S. Chandra, J. R. Ziemke, and R. V. Martin. Tropospheric ozone at tropical and middle latitudes derived from TOMS/MLS residual: Comparison with a global model. *Journal of Geophysical Research*, 108(D9), 2003.

[66] J. R. Ziemke, S. Chandra, B. N. Duncan, L. Froidevaux, P. K. Bhartia, P. F. Levelt, and J. W. Waters. Tropospheric ozone determined from Aura OMI and MLS: Evaluation of measurements and comparison with the Global Modeling Initiative's Chemical Transport Model. *Journal of Geophysical Research*, 111:D19393, 2003.

[67] X. Liu et al. First directly retrieved global distribution of tropospheric column ozone from GOME: Comparison with the GEOS-CHEM model. *Journal of Geophysical Research*, 111(D2):D20308, 2006.

[68] M. R. Schoeberl et al. A trajectory-based estimate of the tropospheric ozone column using the residual method. *Journal of Geophysical Research*, 112:D24S49, 2007.

[69] I. K. Stajner et al. Assimilated ozone from EOS-Aura: Evaluation of the tropopause region and tropospheric columns. *Journal of Geophysical Research*, 113:D16S32, 2008.

[70] Q. Yang, D. M. Cunnold, H. J. Wang, L. Froidevaux, H. Claude, J. Merrill, M. Newchurch, and S. J. Oltmans. Midlatitude tropospheric ozone columns derived from the Aura Ozone Monitoring Instrument and Microwave Limb Sounder measurements. *Journal of Geophysical Research*, 112:D20305, 2007.

[71] ESA-Envisat website, *http://www.envisat.esa.int/*.

[72] M Gottwald et al. *SCIAMACHY: monitoring the changing Earth's atmosphere*. Pubbl. by DLR-IMF, 2006.

[73] J. P. Burrows and K. V. Chance. Scanning Imaging Absorption spectroMeter for Atmospheric CHartographY. In *Proceedings of SPIE*, volume 1490, pages 146–55, 1991.

[74] H. Bovensmann, J. P. Burrows, M. Buchwitz, J. Frerick, S. Noël, V. V. Rozanov, K. V. Chance, and A. H. P. Goede. SCIAMACHY - Mission objectives and measurement modes. *Journal of Atmospheric Science*, 56(2):127–50, 1999.

[75] G. Lichtenberg et al. SCIAMACHY Level 1 data: calibration concept and in-flight calibration. *Atmospheric Chemistry and Physics*, 6:5347–67, 2006.

[76] S. Noël, H. Bovensmann, J. Skupin, M. W. Wuttke, J. P. Burrows, M. Gottwald, and E. Krieg. The SCIAMACHY calibration/monitoring concept and first results. *Advances in Space Research*, 32(11):2123–8, 2003.

[77] NASA-Aura website, *http://www.aura.gsfc.nasa.gov/*.

[78] G. L. Stephens et al. The Cloudsat mission and the A-Train. *American Meteorological Society*, pages 1771–91, 2002.

[79] D. Crisp and C. Johnson. The Orbiting Carbon Observatory mission. *Acta Astronautica*, 56:193–7, 2005.

[80] G. A. Vicente, S. Kempler, P. Smith, K. Tewari, R. Kummerer, G. Leptoukh, G. Stephens, P. Partain, and D. Reinke. The NASA A-Train and the next generation of Earth Science Data Integration. *EOS Transaction AGU Fall Meeting*, 86(52), 2005.

[81] P. F. Levelt. OMI algorithm theoretical basis document: OMI instrument, Level 0-1b processor, calibration & operations. Technical Report 1, P. F. Levelt Eds., Royal Netherlands Meteorological Institute, De Bilt, the Netherlands, 2002.

[82] M. R. Dobber et al. Ozone Monitoring Instrument calibration. *IEEE Transaction on Geosciences and Remote Sensing*, 44(5):1209–38, 2006.

[83] I. H. Hopkins and G. R. Hopkinson. Random telegraph signals from proton-irradiated CCDs. *IEEE Transaction on Nuclear Science*, 40(6):1567–74, 1993.

[84] AVDC website, *http://avdc.gsfc.nasa.gov/*.

[85] J. R. Jensen. *Remote sensing of the environment: an Earth resource perspective.* Prentice Hall Eds., Upper Saddle River, NJ, USA, 2007.

[86] J. B. Campbell. *Introduction to remote sensing.* The Guilford Press, New York, NY, USA, 2002.

[87] G. Galati and A. Gilardini. *Tecniche e strumenti per il telerilevamento ambientale*, volume 1. Consiglio Nazionale delle Ricerche Eds., Rome, Italy, 2001.

[88] S. Twomey. *Introduction to the mathematics of inversion in remote sensing and indirect measurements.* Dover Publications Inc., Mineola, NY, USA, 1996.

[89] C. D. Rodgers. *Inverse methods for atmospheric sounding: Theory and practice.* World Scientific Publishing Company, London, UK, 2000.

[90] C. M. Bishop. *Neural networks for pattern recognition.* Oxford University Press, New York, USA, 1995.

[91] S. Haykin. *Neural networks: A comprehensive foundation.* Prentice Hall, Upper Saddle River, NJ, USA, second ed. edition, 1999.

[92] V. Kecman. *Learning and soft computing, support vector machines, neural networks and fuzzy logic models.* MIT Press, Cambridge, MA, USA, 2001.

[93] K. Hornik, M. Stinchcombe, and H. White. Multilayer feedforward networks are universal approximators. *Neural Network*, 2(5):359–366, 1989.

[94] D.E. Rumelhart, G.E. Hinton, and R.J. Williams. Learning representations by back propagating errors. *Nature*, 323:533–6, 1986.

[95] M. F. Møller. A scaled conjugate gradient algorithm for fast supervised learning. *Neural Networks*, 6(4):525–33, 1993.

[96] P. Sellitto, D. Solimini, and F. Del Frate. A neural network algorithm for tropospheric ozone retrievals from ESA-Envisat SCIAMACHY nadir UV/VIS measurements. *Under revision for Journal of Geophysical Research.*

[97] F. Del Frate, P. Sellitto, and D. Solimini. Design of neural network algorithms for the retrieval of tropospheric ozone from satellite data. In *Proceedings of Envisat Symposium*, 2007.

[98] P. Sellitto, A. Burini, F. Del Frate, and S. Casadio. Dedicated neural networks algorithms for direct estimation of tropospheric ozone from satellite measurements. In *Proceedings of International Geosciences and Remote Sensing Symposium*, 2007.

[99] J. E. Jonson, D. Simpson, H. Fagerli, and S. Solberg. Can we explain the trends in European ozone levels? *Atmospheric Chemistry anf Physics*, 6:51–66, 2006.

[100] J. Fishman, A. E. Wozniak, and J. K. Creilson. Global distribution of tropospheric ozone from satellite measurements using the empirically corrected tropospheric ozone residual technique: Identification of the regional aspects of air pollution. *Atmospheric Chemistry and Physics*, 3:893–907, 2003.

[101] R. Munro, R. Siddans, W. J. Reburn, and B. J. Kerridge. Direct measurement of tropospheric ozone distributions from space. *Nature*, 392:171–98, 1998.

[102] H. M. Worden et al. Comparisons of Tropospheric Emission Spectrometer (TES) ozone profiles to ozonesondes: Methods and initial results. *Journal of Geophysical Research*, 112:D03309, 2007.

[103] F. Del Frate and G. Schiavon. A combined natural ortogonal functions/neural network technique for the radiometric estimation of atmospheric profiles. *Radio Science*, 33(2):405–10, 1998.

[104] F. Del Frate, M. F. Iapaolo, S. Casadio, S. Godin-Beekmann, and M. Petitdidier. Neural networks for the dimensionality reduction of GOME measurement vector in the estimation of ozone profiles. *Journal of Quantitative Spectroscopy and Radiative Transfer*, 92:275–91, 2005.

[105] F. Del Frate, M. F. Iapaolo, and S. Casadio. Intercomparison between GOME ozone profiles retrieved by neural network inversion schemes and ILAS products. *Journal of Atmospheric and Oceanic Technology*, 22(9):1433–40, 2005.

[106] M. Iapaolo, S.Godin-Beekmann, F. Del Frate, S. Casadio, M. Petitdidier, I. S. McDermid, T. Leblanc, D. Swart, Y. Meijer, G. Hansen, and K. Stebel. Ozone profiles retrieved by neural network techniques: A global validation with lidar measurements. *Journal of Quantitative Spectroscopy and Radiative Transfer*, 22(9): 1433–40, 2005.

[107] B. Mayer and A. Kylling. Technical note: The libRadtran software package for radiative transfer calculations - description and examples of use. *Atmospheric Chemistry and Physics*, 5:1855–77, 2005.

[108] S. Kato, T. P. Ackerman, J. H. Mather, and E. Clothiaux. The k-distribution method and correlated-k approximation for a shortwave radiative transfer model. *Journal of Quantitative Spectroscopy and Radiative Transfer*, 62:109–21, 1999.

[109] A. Cheymol and H. De Backer. Retrieval of the aerosol optical depth in the UV-B at Uccle from Brewer ozone measurements over a long time period 1984-2002. *Journal of Geophysical Research*, 108(D24), 2003.

[110] P. Sellitto, A. Burini, F. Del Frate, and S. Casadio. Neural networks algorithms for ozone profiles retrieval from satellite measurements: analysis with ESA-Envisat SCIAMACHY and NASA-Aura OMI data. *Geophysical Research Abstracts*, 9: 09410, 2007.

[111] P. Sellitto, F. Del Frate, and A. Burini. Neural networks algorithms for the retrieval of ozone concentration profiles from Envisat-SCIAMACHY measurements. In *Proceedings of Envisat Symposium*, 2007.

[112] P. Sellitto, F. Del Frate, D. Solimini, C. Retscher, B. Bojkov, and P. K. Bhartia. Neural networks algorithms for ozone profile retrieval from ESA-Envisat SCIAMACHY and NASA-Aura OMI satellite data. In *Proceedings of International Geosciences and Remote Sensing Symposium*, 2008.

[113] C. P. Loughner, D. J. Lary, L. C. Sparling, R. C. Cohen, P. DeCola, and W. R. Stockwell. A method to determine the spatial resolution required to observe air quality from space. *IEEE Transanction on Geosciences and Remote Sensing*, 45(5): 1308–14, 2007.

[114] P. Sellitto, F. Del Frate, and D. Solimini. Joint temperature and nitrogen dioxide vertical profiles from UV/VIS satellite data for air pollution monitoring from space. In *Proceedings of International Geosciences and Remote Sensing Symposium*, 2008.

[115] L. M. Lamsal, M. Weber, S. Tellmann, and J. P. Burrows. Ozone column classified climatology of ozone and temperature profiles based on ozonesonde and satellite data. *Journal of Geophysical Research*, 109(D20304), 2004.

[116] L. G. Tilstra, G. van Soest, and P. Stammes. Method for in-flight satellite calibration in the ultraviolet using radiative transfer calculations, with application to Scanning Imaging Absorption spectroMeter for Atmospheric CHartographY (SCIAMACHY). *Journal of Geophysical Research*, 110(D18311), 2005.

[117] K. F. Boersma, E. J. Bucsela, E. J. Brinksma, and J. F. Gleason. OMI algorithm theoretical basis document: OMI trace gas algorithms. Technical Report 4, K. Chance Eds., Smithsonian Astrophysical Observatory, Cambridge, MA, USA, 2002.

[118] ESA EO-GRID portal *http://eogrid.esrin.esa.int/*.

List of Figures

1.1 Standard thermal structure of the atmosphere at different latitudes and seasons. Elaborated from data taken from [3]. 5
1.2 A standard ozone profile at mid-latitudes. Figure taken from [5] 7
1.3 Standard ozone concentration profiles at different latitudes and seasons. Elaborated from data taken from [3] 7
1.4 Two ozone soundings made at the South Pole in September and October 2002 (red line), compared to a pre-ozone hole profile taken on August 2002 (blue line). A temperature profile is also reported (green line). Figure taken from [12]. 11
1.5 Global mean total ozone for different months in 2008. Elaborated from data taken from [13]. 12
1.6 The Antarctic ozone hole evolution in the period 1995-2004: September's concentrations taken from GOME and SCIAMACHY data. Courtesy of DLR. 12
1.7 Scheme of the major ozone transport, formation and removal phenomena. Courtesy of NASA. 13
1.8 UV and VIS ozone absorption spectrum at T=298.0 K (a), and spectral differences of the cross sections at different temperatures (b). Elaborated from data taken from [23] 17

2.1 EnviSat during integration in ESA-ESTEC, the Nederlands. Courtesy of Dutch Space. 29
2.2 Sciamachy level 1 OA. Courtesy of DLR-IMF. 30
2.3 Sciamachy level 2 OA. Courtesy of DLR-IMF. 31
2.4 Sciamachy observation modes and related optical paths or *trains*. Courtesy of DLR-IMF. 31
2.5 SCIAMACHY's science observation modes. 1 = nadir, 2 = limb, 3 = occultation. Courtesy of DLR-IMF. 35
2.6 SCIAMACHY's Total Clear Fields of View (TCFoV) and observation geometries. Courtesy of DLR-IMF. 35
2.7 SCIAMACHY reference orbit with timelines. Courtesy of DLR-IMF. . . . 36
2.8 Ground pixels for a nadir measurement (only forward scan); integration time = 1 sec (left), integration time = 0.125 (right). Courtesy of DLR-IMF. 37
2.9 SCIAMACHY data calibration concept. Courtesy of SRON. 38
2.10 Memory effect for SCIAMACHY's channel 3. Courtesy of SRON. 39
2.11 Q (blue) and u (red) polarization sensitivities for channel 1-5 nadir measurements (elavation angle of 61°). Courtesy of SRON. 40
2.12 Aura during integration and a scheme of the platform with its four instruments. 42

2.13 The A-Train. Figure taken from [80]. . . . 43
2.14 Conceptual design of the Ozone Monitoring Instrument. Courtesy of Fokker Space. . . . 44
2.15 OMI UV OA. Courtesy of KNMI. . . . 45
2.16 OMI VIS OA. Courtesy of KNMI. . . . 46
2.17 OMI measurements concept. Courtesy of Dutch Space. . . . 48
2.18 OPF relations with relevant products and processors [81]. . . . 49
2.19 Time histograms (left) and dark currents as a function of time (right) for 3 pixels hit by a proton and showing a RTS behavior [82]. . . . 52
2.20 Spectral stray light fraction in UV1 at 290 nm as a function of the source wavelength [82]. . . . 53
2.21 Spatial stray light at column 300 (about 340 nm) in UV2 with source illumination at nadir [82]. . . . 53
2.22 Measured and fitted OMI instrument BSDF for the three onboard diffusers for nadir viewing angle and nominal azimuth and elevation angles. The curves show the BSDF results for the backup aluminum diffuser, the regular aluminum diffuser, and the quartz volume diffuser from top to bottom [82]. . . . 54

3.1 Summary of the differences between soft and hard computing algorithms. 63
3.2 Scheme of a MLP. . . . 64
3.3 Two tentative approximation functions (thick line) of underlying function (dashed line) describing data (crosses). The case on the left reveals overfitting. Figure adapted from [92]. . . . 66
3.4 Weight w_{kj} connecting the j-th hidden layer neuron with the k-th output layer neuron and its adaptation Δw_{kj} in relation to backpropagating error signal δ_{ok}. . . . 68
3.5 Detailed MLP scheme, with indication of backpropagating errors signals. . 68

4.1 Spectral differences (%) of Earth's radiance for a doubling of ozone concentration at z=14 km with respect to AFGL mid-latitude standard, with noise. Please refer to the text for the model settings. . . . 75
4.2 Spectral differences (%) of Earth's radiance for a doubling of ozone concentration at z=1, 4, 8, 12 km with respect to AFGL mid-latitude standard, without noise. Please refer to the text for the model settings. . . . 75
4.3 UV radiative forcing vs. height at a fixed observation angle (SZA=30°, $\vartheta = 0$) for ozone doubling. A sigmoidal fitting function is shown. Each point represents the mean value and the bar is the standard deviation of a set of 500 spectral simulations; each simulation includes a 1% level Gaussian noise. . . . 76
4.4 VIS radiative forcing vs. height at a fixed observation angle (SZA=30°, $\vartheta = 0$) for ozone doubling. Each point represents the mean value and the bar is the standard deviation of a set of 500 spectral simulations; each simulation includes a 1% level Gaussian noise. . . . 77
4.5 UV/VIS forcing ratio vs. height at a fixed observation angle (SZA=30°, $\vartheta = 0$) for ozone doubling. Each point represents the mean value and the bar is the standard deviation of a set of 500 spectral simulations; each simulation includes a 1% level Gaussian noise. Two different straight lines for the ranges 0-7 km and 8-14 km are shown. . . . 77

4.6 TOC NNs scheme. 79
4.7 Scaling function of the input training vector in TCO dedicated UV NN. Overlapped a linear scaling function is reported to underline the larger slope of our scaling function near the boundaries of the selected radiance interval. 80
4.8 Retrieved normalized TOCs vs. "true" noisy simulated data, for UV-only measurements. Pearson coefficient value is reported. 81
4.9 Density of the selected wavelengths after 10000 (a), 40000 (b) pruning steps and at the end (about 90000 steps) of the whole procedure (c). The gray scale represents the density at some selected ranges, i.e. the number of useful measurement wavelengths per nm. A standard Earth's radiance spectrum calculated by means to the UVSPEC code is overlapped. 83
4.10 UV/VIS TOC NN scheme. The subdivision of the UV and VIS input bands are indicated. 84
4.11 Retrieved normalized TOCs vs "true" noisy simulated data, for UV/VIS input measurements. Pearson coefficient value is reported. 85
4.12 Matching distance vs. latitude of SCIAMACHY measurements vs. ozonesondes stations (solid line) and GOME measurements vs lidar stations as described by [106] (dashed line). The vertical lines identify the 30°N-60°N latitude range. 86
4.13 Map of the matching points between mid-latitude ozonesondes stations and SCIAMACHY overpasses. 86
4.14 Time series of the retrieved (asterisks with errorbars) and simultaneous reference ozonesondes TOCs (diamonds) at Uccle and Debilt stations, in the period january 2003-may 2004. 88

5.1 Trend of available ozonesondes profile measurements in the interval 2002-2006. 91
5.2 WOUDC and SHADOZ active ozonesonde stations (red circles) in the period 2002-2006. Only stations with at least one measurement in the complete range 1000.0-6.5 hPa have been considered. 91
5.3 Number of available ozonesondes measurements versus latitude. 91
5.4 Example of a SCIAMACHY-NN retrieved profile (line with diamonds), with ozonesondes target profile (dotted line) as a comparison. Lat/lon = N41.92, E12.50, JD = 201/2003. 93
5.5 NN estimations vs ozonesonde data at pressure level P=178.5 hPa, for an independent ozonesondes subset. Pearson coefficient is reported. 93
5.6 NN estimations vs ozonesonde data at pressure level P=31.6 hPa, for an independent ozonesondes subset. Pearson coefficient is reported. 94
5.7 Height resolved RMSs for SCIAMACHY and GOME NN ozone profile retrievals, and OS standard deviations for the subset in the period Jan.-Aug. 2003 (see text for details). 94

6.1 Two examples of OMI-NN retrieved profiles (line with diamonds), with MLS target profile (dotted line) as a comparison. a) Lat/lon = N43.00, E62.48, JD = 126/2005; b) Lat/lon = N39.41, E22.56, JD=180/2006. . . 99
6.2 Two scatter plots of the retrieved ozone mixing ratios vs MLS target values for the test dataset. a) P = 177.83 hPa; b) P = 1.78 hPa. 99

6.3 RMS deviation profile of the retrievals (line) and MLS target values' standard deviation (dotted line), over the test dataset. 100
6.4 Mean absolute differences (%) of our retrievals over the test dataset. . . . 100

A.1 Spectral radiance differences (%) of Eq. (A.4) for the 7 total ozone dependent climatologies of [115]. (a) Lamsal ozone profiles, fixed AFGL temperature profile, (b) Lamsal temperature profile, fixed AFGL ozone profile. 107
A.2 Relative spectral differences of Eq. (A.5). 108
A.3 Absolute relative differences of Eq. (A.5) versus total ozone, at ~ 323.8 nm 108
A.4 Examples of a retrieved profile (diamond with line) with the corresponding true profile (dotted line). Total ozone is 320 DU. 109
A.5 Scatterplot of the NN retrieved NO_2 columns vs true values for the test dataset. 111

B.1 ESA Cat-1 G-POD project 4069 end to end prototype design. 113
B.2 ESA Cat-1 G-POD project 4069 end to end processing and data workflow. 113

List of Tables

1.1 Atmospheric composition: molar fraction of the major atmospheric gasses [1]. 3

2.1 EnviSat parameters. Adapted from [72]. 29
2.2 SCIAMACHY science channels. Adapted from [72] 32
2.3 Aura parameters. Adapted from [77]. 42
2.4 OMI science channels. Adapted from [44]. 44
2.5 Characteristics of the main observation modes. Adapted from [82]. 49

4.1 Selected wavelengths for UV TCO NN input vectors. 79
4.2 Final wavelength selection for UV/VIS TCO NN input vectors. 84

Acronyms

ADEOS	**A**dvanced **E**arth **O**bserving **S**atellite
AFGL	**A**ir **F**orce **G**eophysics **L**aboratory
AO	**A**nalogue **O**ffset
ASM	**A**zimuth **S**can **M**echanism
ATC	**A**ctive **T**hermal **C**ontrol
AVDC	**A**ura **V**alidation **D**ata **C**enter
BSDF	**B**idirectional **S**cattering **D**istribution **F**unction
BU	**B**inary **U**nits
BUV	**B**ackscatter **U**ltra**V**iolet
CALIPSO	**C**loud-**A**erosol **L**idar and **I**nfrared **P**athfinder **S**atellite **O**bservation
CCD	**C**harged **C**oupled **D**evice
CFC	**C**hloro**F**luoro**C**arbon
CLAES	**C**ryogenic **L**imb **A**rray **E**talon **S**pectrometer
CLOUDSAT	**CLOUD SAT**ellite
CNES	**C**entre **N**ational d'**E**tudes **S**patiales
DC	**D**ark **C**ount
DEM	**DE**tector **M**odule
DIAL	**DI**fferential **A**bsorption **L**idar
DISC	**D**ata and **I**nformation **S**ervices **C**enter
DLR	**D**eutschen zentrums für **L**uft- und **R**aumfahrt
DOAS	**D**ifferential **O**ptical **A**bsorption **S**pectroscopy
EA	**E**lectronic **A**ssembly
ECC	**E**lectrochemical **C**oncentration **C**ell
ELU	**EL**ectronic **U**nit
ENVISAT	**ENVI**ronmental **SAT**ellite

EOS	**E**arth **O**bserving **S**ystem
EP	**E**xtended **P**runing
ERS	**E**uropean **R**emote **S**ensing satellite
ESA	**E**uropean **S**pace **A**gency
ESM	**E**levation **S**can **M**echanism
ESSP	**E**uropean **S**atellite **S**ervices **P**rovider
FoV	**F**ield **o**f **V**iew
FWHM	**F**ull **W**idth at **H**alf **M**aximum
GAW	**G**lobal Atmosphere Watch
GDPS	**G**round **D**ata **P**rocessing **S**ystem
GES	**G**oddard **E**arth **S**ciences
GOME	**G**lobal **O**zone **M**onitoring **E**xperiment
GOMOS	**G**lobal **O**zone **M**onitoring by **O**ccultation of **S**tars
GPOD	**G**rid **P**rocessing **O**n **D**emand
GSFC	**G**oddard **S**pace **F**light **C**enter
HALOE	**HAL**ogen **O**ccultation **E**xperiment
HIRDLS	**HI**gh **R**esolution **D**ynamics **L**imb **S**ounder
IAM	**I**nterface **A**daptor **M**odule
ICU	**I**nstrument **C**ontrol **U**nit
IFoV	**I**nstantaneous **F**ield **o**f **V**iew
ILAS	**I**mproved **L**imb **A**tmospheric **S**pectrometer
ILOS	**I**nstantaneous **L**ine **O**f **S**ight
IMF	**I**nstitut für **M**ethodik der **F**ernerkundung
IR	**I**infra**R**ed
ISAMS	**I**mproved **S**tratospheric **A**nd **M**esospheric **S**ounder
IT	**I**ntegration **T**ime
KNMI	**K**oninklijk **N**ederlands **M**eteorologisch **I**nstituut
LEO	**L**ow **E**arth **O**rbits
LC	**L**eakage **C**urrent
LIDAR	**LI**ght **D**etection **A**nd **R**anging
LIMS	**L**imb **I**nfrared **M**onitor of the **S**tratosphere
LOS	**L**ine **O**f **S**ight
LRIR	**L**imb **R**adiance **I**nversion **R**adiometer

METOP	**MET**eorological **OP**erational satellite
MIPAS	**M**ichelson **I**nterferometer for **P**assive **A**tmospheric **S**ounding
MLS	**M**icrowave **L**imb **S**ounder
MO	**M**oon **O**ccultation
MW	**M**icro**W**aves
NASA	**N**ational **A**eronautics and **S**pace **A**dministration
NDACC	**N**etwork for **D**etection of **A**tmospheric **C**omposition **C**hange
NDFM	**N**eutral **D**ensity **F**ilter **M**echanism
NIR	**N**ear **I**nfra**R**ed
NN	**N**eural **N**etwork
NOAA	**N**ational **O**ceanic and **A**tmospheric **A**dministration
NPOESS	**N**ational **P**olar **O**rbiting **E**nvironmental **S**atellite **S**ystem
OA	**O**ptical **A**ssembly
OBM	**O**ptical **B**ench **M**odule
OCO	**O**rbiting **C**arbon **O**bservatory
OE	**O**ptimal **E**stimation
OMI	**O**zone **M**onitoring **I**nstrument
OPF	**O**perational **P**arameters **F**ile
OPB	**OP**tical **B**ench
OS	**O**zone**S**ondes
OSIRIS	**O**ptical **S**pectrograph and **I**nfra**R**ed **I**mager **S**ystem
PAN	**P**eroxy**A**cetyl**N**itrate
PARASOL	**P**olarization and **A**nisotropy of **R**eflectances for **A**tmospheric **S**ciences coupled with **O**bservations from a **L**idar
PET	**P**ixel **E**xposure **T**ime
PMD	**P**olarization **M**easurement **D**evice
PMTC	**P**ower **M**echanism and **T**hermal **C**ontrol
POAM	**P**olar **O**zone and **A**erosol **M**easurement
PSC	**P**olar **S**tratospheric **C**loud
QE	**Q**uantum **E**fficiency
RC	**R**adiant **C**ooler
RCA	**R**adiant **C**ooler **A**ssembly
RRU	**R**adiant **R**eflector **U**nit

RTM	**R**adiative **T**ransfer **M**odel
RTS	**R**andom **T**elegraph **S**ignal
SAGE	**S**tratospheric **A**erosol and **G**as **E**xperiment
SAOZ	**S**ysteme d'**A**nalyse par **O**bservation **Z**enithale
SBI	**S**atellite **B**us **I**nterface
SBUV	**S**olar **B**ackscatter **U**ltra**V**iolet
SCIAMACHY	**SC**anning **I**maging **A**bsorption spectro**M**eter for **A**tmospheric **CH**artograph**Y**
SDPU	**S**cience **D**ata **P**rocessing **U**nit
SF	**S**un **F**ollower
SHADOZ	**S**outhern **H**emisphere **AD**ditional **OZ**onesondes
SLS	**S**pectral **L**ine **S**ource
SMR	**S**ub**M**illimeter **R**adiometer
SO	**S**olar **O**ccultation
SPOT	**S**atellite **P**our l'**O**bservation de la **T**erre
SRON	**S**tichting voor **R**uimte**O**nderzoek **N**ederland
STE	**S**tratospheric **T**ropospheric **E**xchanges
SWIR	**S**hort **W**avelength **I**nfra**R**ed
SZA	**S**olar **Z**enith **A**ngle
TBU	**T**hermal **B**us **U**nit
TCFoV	**T**otal **C**lear **F**ield **o**f **V**iew
TIR	**T**hermal **I**nfra**R**ed
TOC	**T**ropospheric **O**zone **C**olumn
TOMS	**T**otal **O**zone **M**apping **S**pectrometer
TOR	**T**ropospheric **O**zone **R**esidual
UARS	**U**pper **A**tmosphere **R**esearch **S**atellite
UV	**U**ltra**V**iolet
UVISI	**U**ltraviolet and **V**isible **I**magers and **S**pectrographic **I**magers
VIS	**VIS**ible
WLS	**W**hite **L**ight **S**ource
WMO	**W**orld **M**eteorological **O**rganization
WOUDC	**W**orld **O**zone and **U**ltraviolet radiation **D**ata **C**enter

Symbols

k	Extinction/absorption/scattering coefficient	m^{-1}
ν	Frequency	Hz
ρ	Mass Density	$\mathrm{kg/m}^3$
I	Irradiance	$\mathrm{W/m}^2$
τ	Optical Depth	pure
L	Radiance	$\mathrm{W/(m}^2\mathrm{sr)}$
F	Radiant Flux	$\mathrm{W/m}^2$
R	Reflectance	pure
$\tilde{\omega_0}$	Single scattering albedo	pure
λ	Wavelength	m